ULTRASONIC GUIDED WAVES APPLICATIONS FOR LOCATING AND QUANTIFYING PIPELINES DEFECTS

ALIREDA A. ALJAROUDI

ULTRASONIC GUIDED WAVES APPLICATIONS FOR LOCATING AND QUANTIFYING PIPELINES DEFECTS

By

Alireda A. Aljaroudi

A Thesis submitted to the

School of Graduate Studies

in partial fulfillment of the requirements for the degree of

Master of Engineering

Faculty of Engineering and Applied Science

Memorial University of Newfoundland

August 2011

St. John's Newfoundland Canada

ABSTRACT

On-line Health Monitoring of industrial structures in particular the oil and gas transporting system such as pipelines is of great importance to the reliability and survivability of the plant. In this research the propagation of Ultrasonic Guided Waves as a tool to condition monitoring of the pipes was investigated. Also, under this research the Kirchhoff flaw approximation model was modified to provide an estimation of the size and location of flaws that may exist along the pipe. The modified model and the dispersion curves generated by the Ultrasonic Waves using PCDISP software can provide assessment of the location and extent of the flaw. Several simulation trials were performed using Matlab to validate the feasibility and applicability of the modified model and the results indicate that this model can accurately estimate the size and location of the flaws that exist in the pipe.

ACKNOWLEDGEMENTS

I would like to express my thanks and appreciation to Dr. Mahmoud Haddara and Dr. Faisal Khan who provided me with excellent guidance and support throughout the course of this research. Their outstanding supervision and encouragement strongly contributed to the success of this research. They were accommodating, committed and forthcoming and most of all they were tolerant. This tolerance played a major role in going forward with this research leading to a successful completion despite the difficulties and challenges.

Thanks and words of appreciation go to the faculty of Engineering and Applied Science and the library staff at Memorial University of Newfoundland for providing the required support and assistance throughout the research period.

Finally, special thanks go to all members of my family, my friends and colleagues for their support and encouragement.

Table of Contents

CHAPTER 6

CHAPTER 7

List of Tables

List of Figures

CHAPTER 1

INTRODUCTION

1.1 INTRODUCTION

Pipeline networks serve as the backbone of the oil and gas supply system; hence, it should be highly reliable and capable in meeting customers' demand for oil and gas products at all times. Continuous flow of these products plays a major role in the prosperity and advancement of nations and as such should remain stable and available at all times. Thus, it is imperative that such network be given the highest consideration and attention at all times to insure its integrity and safety.

There are many contributing factors to the failure of pipelines that could affect their integrity. One of these contributing factors is the aging of the existing oil and gas infrastructure. Other contributing factors include corrosion, interference from third party, material defects, malfunction, and natural hazards. These are key causes that can lead in most cases to undesired consequences. Such consequences may include puncture, rupture and/or leakage of the pipe that may result in injuries, fatalities and catastrophic damage to the surrounding environment and loss of production.

Hence, innovative monitoring systems and defects diagnosis techniques should be in place to insure the sustainability of the infrastructure, i.e. pipelines and the associated equipment to insure their integrity and continuity.

Generally, Non Destructive Testing (NDT) is used by the industry for assessing pipeline integrity and reliability. It is an acceptable practice to detect dangerous defects before they can cause catastrophic failure or interruption to production. The main issue with such system is that it is performed on as need basis or at regular maintenance intervals and does not provide on-line monitoring and detection of failures as they happen.

Most of the literature reviewed dealt with utilizing guided wave technology coupled with Digital Signal Processing (DSP) systems as the main components of the NDT system. The Guided Wave system consists mainly of one or group of transducers that are placed on the structure to detect the existence of defect. If the inspected structure is a pipeline, the abnormalities such as metal loss, holes or cracks, will cause a discontinuity to the transmission of the Guided Wave along the pipe. As a result, some portion of the wave energy is reflected back. The reflected wave can then be analyzed to determine the location, type and the extent of the damage.

Integrating guided waves techniques with wireless communication systems can transparently and easily interface with sensors for monitoring objects or any other structures above ground, underground or underwater. The structural health status of the

monitored object will be up to date and will give advance warning should any structural health problem occur.

Before going any further, one needs to study the behavior of the guided waves as they propagate along the structure and their interaction with a defect. The reviewed literature included some information that can be used to analyze the behaviors of the guided waves but, for estimating the defect mathematically, such models could not be found. Based on the reviewed literature by the author, there is no mathematical model that can provide interaction of the Guided Waves with defects where the defects can be estimated and located. All the reviewed literature dealt with experimental work and some analytical methods such as Finite Element Method (FEM) to estimate the location and the size of the flaw.

So, the main objective of this research is to model and simulate the behaviors of the ultrasonic Guided Waves propagation along hollow cylinders and their interaction with defects. The model can be used to determine beforehand if a flaw has occurred and if it has occurred, determine its location and size. Such model can serve as a prerequisite for experimental work or real time operation. To validate this model, several tests should be presented and investigated to conclude its feasibility.

1.2 OBJECTIVE

The objective of this research is to:

- Investigate the propagation of ultrasonic guided waves in solid structures.
- Develop a mathematical model that can predict the location and size of spherical flaws.

1.3 RESEARCH LIMITATION

The focus of the research will be on:

- Ultrasonic waves propagation in hollow cylinders.
- Locating and estimating spherical flaws.

1.4 RESEARCH METHODOLOGY

- Investigate the propagation of ultrasonic Waves propagation into hollow cylinders.
- Develop a mathematical model that can provide an estimation of the size of the flaw and its location along the hollow cylinder.
- Use Matlab as the programming tool to perform the simulation of the developed model.
- Perform several simulation trials with different flaw sizes located at different distances along the investigated structure.
- Determine if the model can accurately estimate and locate the flaw as the flaw size and flaw location change.

- Compare the results obtained from experimental work found in the literature with the results produced by the simulation.
- Investigate the feasibility of the developed model from the results obtained and the comparison analyses performed in the abovementioned steps.

1.5 ORGANIZATION OF THE THESIS

The thesis consists of seven chapters; the first chapter provides an introduction to the research topic, the research objective, research limitation and methodology. Chapter 2 provides literature review about ultrasonic guided waves. Chapter 3 presents the theoretical background of ultrasonic guided waves propagation into hollow cylinders while chapter 4 discuses the digital signal processing techniques for ultrasonic waves and the formulation of the mathematical model to locate and assess the extent of flaws on hollow cylinders. Simulation of the formulated model and analyses are presented in chapter 5. Chapter 6 provides a comparison between some experimental results reported in the literature and results obtained by the formulated model. Finally, summary, concluding remarks and recommendation for future work are discussed in chapter 7.

CHAPTER 2

LITERATURE REVIEW

In this review a summary of scientific articles, conferences' proceedings and independent research articles available in the open literature about guided waves and their applications in assessing the integrity of structures such as pipelines is presented. Most of the literature reviewed dealt with utilizing Guided Wave technology coupled with either signal processing techniques, Finite Element Method (FEM), Boundary Element Method (BEM) or Neural Network (NN) to locate and quantify the extent of the damage. Signal processing techniques that were used included Fast Fourier Transforms, Short Time Fourier Transforms (STFT) and Wavelet Transforms (WT).

The guided wave system consists mainly of one or group of transducers that are placed on the structure reporting the health status of the structure 24/7. The transducers are excited at equal time intervals to determine the health status of the monitored structure and to detect any abnormalities that have occurred during the monitoring period. The reported data are sent back to the main office computer network for further analysis using Digital Signal Processing (DSP) techniques. From these signals the health of the monitored structure can be determined. If an abnormality has occurred the reflected signals will indicate that such abnormality has occurred, where its location, and extent can be determined.

In case that the monitored object is a pipeline, the abnormalities such as metal loss, holes or cracks, will cause a discontinuity to the transmission of the wave along the pipe. As a result, some portion of the wave energy gets reflected back for further analysis. Based on the analysis using the aforementioned techniques, the location, type and the extent of the damage can be estimated.

Under this method the pipe is interrogated for a while, and then time-histories of the received signal amplitude versus frequency curves are generated. From these curves the relationship between the characteristics of the reflected signal and the defect features can be established.

Another approach which is different from the aforementioned method is called SMART layer where a layer of sensors is mounted on the pipe. Once the signal encounters a discontinuity, the reflected signal from the defect is compared with a signal of defect-free pipe. After that the Probability Density Function (PDF) curves are plotted to indicate the most probable size of the damage.

A prior knowledge of the mechanics of the guided waves is an essential element in the study and analysis of their propagation behaviors in solid structure such as hollow cylinder. The outcome of the studies and analysis can be used to assess the integrity of monitored structure.

The general solution of the guided waves propagating in an infinitely long elastic hollow cylinder was first studied by Gazis (1959) using elasticity theory. The solution he provided was viewed as the most fundamental concept that most researchers referred to in their work. In his study, a three dimensional solution of the wave propagation in a hollow cylinder was provided Gazis (1959a, 1959b).

There are many articles found in the literature investigated and analyzed Guided Waves and their application for detecting and locating defects on hollow cylinders such as pipes. These papers were reviewed and summarized in the subsequent sections.

Lu (2005) investigated the application of guided acoustic waves in monitoring beams and tubular components of steam generators and heat exchangers. The time-frequency and pattern recognition techniques were used to classify several defects and the analytical evaluation of wave's propagation was implemented by using Finite Element Method (FEM) and ABAQUS software. It was concluded that the structural flaws can be detected by using transient and nonlinear acoustic signal analysis and the analytical agreed with the experimental results.

It was also concluded that Lamb waves have multi-mode that could confuse the analyst of the reflected waves where each mode exhibits nonlinearity in their behaviors. It was noted that the speed is a nonlinear function of the product of the frequency and thickness.

Zhao (2003) investigated the interaction between phenomena of scattering and mode conversion of guided waves as a result of defects in hollow cylinders. Two and three-dimensional defects were studied by using the Boundary Element Method (BEM) and the Normal Mode Expansion (NME) techniques. These techniques were used to analyze and determine the size of the defect. The research concluded that the phase and group velocities dispersion curves and wave field distributions were dependent on the ratio of wall thickness to the radius. It was also concluded that both Lamb and Shear Horizontal (SH) waves can be used to quantify defects in plate like structure.

Assessing the integrity of pipelines using guided waves can be determined while the pipeline is in-service. In his work, Ahmad (2005) assessed the integrity of pipelines using guided waves while the pipeline is in-service. In his work, a technique based on cylindrical guided waves was implemented to identify and locate the defects for underground water pipelines while in-service. Both theoretical and experimental investigations were conducted. Several pipes with different setup and conditions were used in the lab experiments including a pipe in contact with the air; a pipe filled with water and the outer surface was in contact with air; a pipe was placed under ground without flow of water and finally a pipe embedded in soil and with water flow. Piezoelectric Transducers (PZT) were used to produce cylindrical guided waves throughout the pipe for detecting the damage but no mention was cited about the assessment of defects.

Guo (2001) proved that ultrasonic guided waves were sensitive to pipeline defects. A transducer holder was fabricated to allow the transducer to generate the guided wave throughout the pipe at different angles and at different positions i.e., horizontal, vertical and at inclined positions. Steel, aluminum and copper pipes were used for the experiment. Pipes without defects tested first and then pipes with defects were tested to present the difference between the data of both situations. Lamb waves were generated by an ultrasonic exciter where these waves travelled throughout the pipe. The reflected signal was recorded where a plot of voltage versus signal was presented. Any variation of the recorded data for the defect-free pipeline and a pipeline with a defect indicated the presence of pipeline anomalies. Anomalies such as dent, gouge and removed metal were investigated under this research. The work presented only a situation of a pipe in mid air with three types of defects to detect the defects but not the extent of the defect.

Application of guided waves for underwater applications was proved to be feasible and promising. Na and Kundu, (2002) conducted and experiment on five different aluminum pipes with different sizes, with defect free and with different types of defects namely removed metal, dent, and gouges. The experiment was conducted several times to investigate the consistency of the results. Each test was conducted at different location on the pipe. Different frequencies versus amplitude plots were generated to identify the defects. From the results the defect can be detected but the estimation of the size of the defect was not part of the study.

Takashi, Nobuhiko, Fumitoshi and Kiyotaka (2006), implemented a system of Guided Wave pipe inspection and monitoring where the system consisted of sensors made of magnetostrictive strip of Nickel and coils, a transducer and a software program. The waves were generated which propagated along the pipe and were reflected back at points where the acoustic impedance changes indicating a resistance in the wave propagation. So, the reflected wave was generated whenever the section was changed. The designed system showed its ability to detect gradual wall thickness losses in pipes, pipe elbows and pipe reducers but not the extent of the defect.

Hwang (2002) used Wavelet Basis Function (WBF) neural network to predict 3-D characterization of pipeline defects. The method was validated by simulation data and experimental trials by using magnetic flux signatures. It was indicated from the results that the 3-D characterization of defects by applying WBF Neural Networks can be obtained with certain accuracy. The accuracy of characterization of defects increases by considering the radial, circumferential and axial coordinates. The experiment dealt with the characterization of the defect but not the size of the defect itself.

Yang (2009) used Wavelet Transform Coefficient (WTC) Method to investigate the relationship between the WTC and the depth of cracks in concrete plate and concrete pipes. It was concluded that central frequencies have to be adjusted in accordance to the thickness for the tested object. It was also concluded that there is a correlation between the WTC and the depth of cracks where the depth can be determined with high accuracy.

Using wireless communication system inside a pipe was one of the areas that has been addressed in the literature. In his work, Kokossalak (2006), studied and evaluated the feasibility of a communication system based on an in-pipe wireless sensors network for monitoring underground water pipelines. The proposed system used modulated acoustic waves to carry the data pertaining to the pipeline condition and the pipeline was used as a wave guide for the acoustic waves. The system was evaluated by means of numerical simulation and lab experiment. The system consisted mainly of several sensors installed inside the pipe that transmit the acoustic waves to the destination for further processing to determine the condition of the pipe. The acoustic waves penetrated the walls of the pipe, the water and the surrounding environment which is in this case the ground. Several issues existed concerning the wave propagation along and within the pipeline that included, dispersion, attenuation of the signal, losses of the signal into the surrounding environment and the resulted echoes at pipe joints and bends, also, the power limitations feeding the sensors. All these issues were addressed in the research. This work was concerned mainly about the feasibility of using acoustic communications to detect and locate pipeline abnormalities while using the water pipeline as the transmission medium.

In his work, Hay (2004), studied different guided wave methods and recommended that the piezoplymers sensors are the most suitable for the Structural Health Monitoring (SHM). It was demonstrated that certain types of sensors are compatible with wireless communication systems. His work included the development of an analytical tool to model the displacement of Guided Waves (GW) on fixed structure by using two dimensional Fourier transforms techniques. In addition, the compatibility of GW with

wireless communication was investigated and concluded that it is compatible with wireless communication systems. The sensors were designed to detect cracks of 1 mm length where the frequency tuning technique was used to generate the GW. The experiment was conducted in a lab setting and in the field using US navy helicopter as a test bed. For the experiment in the field, eight sensors were installed on the helicopter and data was recorded and analyzed over a 2-year period. The data was observed for any changes in the received signals by using coefficient of correlations. Any change in the correlation coefficient will indicate the presence of cracks. It was concluded that the application of these sensors are feasible for structural health monitoring using wireless communications system for transmitting signals and receiving the data from the monitored structure.

Another approach which is different from the Guided Wave method is the SMART layer where a layer of sensors is mounted on the pipe to provide around the clock monitoring of the structure. Qing et al. (2009) utilized SMART layer technology to detect pipeline defects such as corrosion, growth of corrosion and pinholes. The system is called RAPID, Real-time Active Pipeline Integrated Detection. It consisted of a sensor network, portable hardware devices and diagnostic software. The way it operated was that the portable devise generates stress waves that propagate along the pipe, when the propagating wave encounters a discontinuity in the geometry of the pipe, the wave is reflected back. After it gets reflected back, it is compared with a previously recorded sensor response from the undamaged pipe. The difference between the two signals will determine if any defect would exist along the pipe. The layers of sensors are embedded piezoelectric disks

performing the function of sensing in real time. A probability density function (PDF) curve was plotted for each type of damage giving the lower and upper limit of the size as well as the most probable damage size but not exact size.

Davies & Cawley (2009), used a system of circumferential array of piezoelectric transducers elements to excite torsional guided wave. The reflected waves from manually made circumferential cracks like-defects and welds were analyzed which revealed the location and the magnitude of the defects. The amplitude of the reflected waves was used to estimate the depth of the defect and the width was estimated by the width of the signal. The results were compared with analytical results obtained from Finite Element Method (FEM) and it was found out that both results agree with each other. Also, it was concluded from ten researches that the accurate size of the defect can be obtained if the circumferential width of the defect exceeds 1.5 times the wavelength of the shear wave.

Kwun, et al. (2008) conducted experiments on pipes and tubes by generating Guided Waves to detect cracks and notches. The notches were made on the pipe at various depths and the data were collected by using magnetostrictive sensors. It was observed that the notches produced at depth of 85% or higher were detectable by the signal.

The experiment did not address the sizing of defects. From the literature reviewed, it was not clear if the defect sizing was possible using the techniques presented. There was no clear evidence that pointed any technique for sizing of defects.

CHAPTER 3

GUIDED WAVES IN HOLLOW CYLINDERS

3.1 WAVE PROPAGATION IN HOLLOW CYLINDERS

Wave propagation in cylindrical waveguides has been studied on the theoretical and experimental levels by researchers at academic institutions and the industry. Such studies can be found in the literature by Gazis (1959), Achenbach (1973), Rose (1999), Kundu (2004) and many others.

There are basically two categories of guided waves that propagate in a hollow cylinder, the circumferential and the axial guided waves. Under the axial category, there are three types of modes generated when waves are propagating along a cylindrical structure. These are the longitudinal, torsional and flexural wave modes. The longitudinal and torsional waves inflict symmetrical displacement of particles in the axial direction across the structure while the flexural waves impose a non-symmetric particle displacement along the structure.

Figure (3.1) provides details of a typical hollow cylinder showing the inner and outer radius and Figure (3.2) illustrates the longitudinal modes propagation where the particle movement is parallel to the wave direction. Figure (3.3) shows the torsioanl wave modes propagating along the circumferential direction of the pipe and the particle motion is

perpendicular to the wave direction. The flexural guided wave has a non-symmetric mode propagating in the [r, z, θ] directions, this is shown in Figure (3.4).

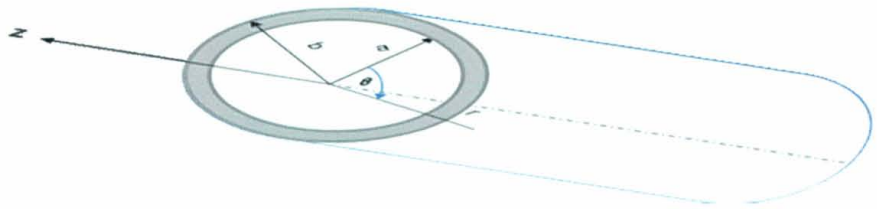

Figure 3.1- Hollow Cylinder with Inner Radius and Outer Radius.

The longitudinal waves which inflict symmetric particles displacement across the pipe in the radial and axial directions can be seen in Figure (3.2).

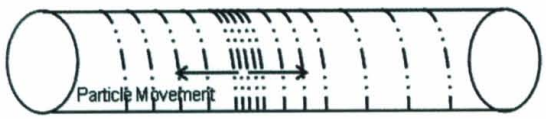

Figure 3.2- Longitudinal Wave with Symmetric Propagation along the Pipe.

The torsional wave with symmetric particles displacement along the circumference of the pipe is shown in Figure (3.3).

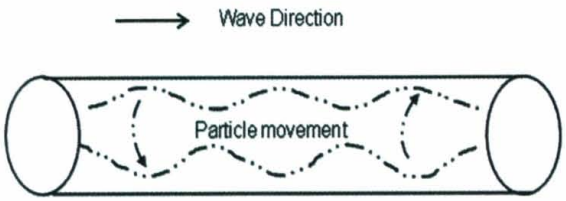

Figure 3.3- Torsional Wave Propagation along the Pipe in the θ Direction.

For flexural waves, all three displacement components exist, the radial, the axial and the circumferential (r,θ,z). This mode is an essential element in the diagnosis of defects (Rose, 1999).

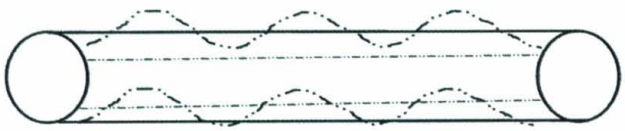

Figure 3.4 - Flexural Wave Showing Nonsymmetrical Propagation.

Waves propagating in the circumferential direction follow a curved path as shown in Figure (3.5).

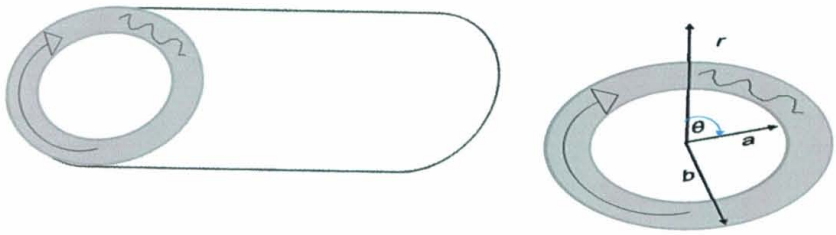

Figure 3.5 - Waves Propagating in Circumferential Direction.

These waves suffer a great deal of dispersion and mode conversion that makes it very difficult to analyze. It is extremely important to have a prior knowledge about the physical characteristics of the wave guide, the propagating medium and the defects that may encounter along the propagation path. Such knowledge serves as a prerequisite for the diagnosis of the reflected waves which can be carried out by using special signal processing techniques. These techniques can provide the characteristics and features of

the reflected waves. Then the outcome of theses analyses will reveal the existence, location and extent of defects should they exist.

3.2 GOVERNING EQUATIONS IN CYLINDRICAL COORDINATES

Consider a hollow cylinder as shown in Figure (3.1) with inner radius *a* and outer radius *b*, assuming that the cylinder is elastic and isotropic. There are two types of waves, the axial and circumferential waves. The axial waves impose longitudinal, torsional and flexural modes of propagation while the circumferential waves follow a curved path around the circumference of the object.

The analysis of governing Equation will start with Navier's displacement Equation. However, this Equation is not wave Equation but as cited in the literature it can provide wave solutions (Gazis, 1959a).

$$\mu\nabla^2\mathbf{u} + (\lambda + \mu)\nabla\nabla\cdot\mathbf{u} = \rho\left(\frac{\partial^2 u}{\partial t^2}\right) \tag{3.1}$$

∇^2 is the Laplace operator, $\mathbf{u}$ is the displacement Vector, λ, μ are the Lamé's Constants and ρ is the density. Gazis (1959), investigated wave propagation in hollow cylinder and decomposed Naveir's Equation by Helmholtz decomposition method. The result is shown

below where displacement vector **u** is expressed in terms of a dilatational scalar potential ϕ and a vector potential $\boldsymbol{\psi}$ as:

$$\mathbf{u} = \nabla\phi + \nabla \times \boldsymbol{\psi} \tag{3.2}$$

Substituting Equation (3.2) into Equation (3.1), Navier's Equation becomes:

$$\nabla\left[(\lambda + 2\mu)\nabla^2\phi - \rho\left(\frac{\partial^2\phi}{\partial t^2}\right)\right] + \nabla \times \left[\mu\nabla^2\boldsymbol{\psi} - \rho\left(\frac{\partial^2\boldsymbol{\psi}}{\partial t^2}\right)\right] = 0 \tag{3.3}$$

If the scalar potential ϕ and the vector potential ψ satisfy the wave Equations then the Navier's displacement Equation is satisfied:

$$\left.\begin{aligned} C_1^2\nabla^2\phi - \frac{\partial^2\phi}{\partial t^2} &= 0 \\ C_2^2\nabla^2\boldsymbol{\psi} - \frac{\partial^2\boldsymbol{\psi}}{\partial t^2} &= 0 \end{aligned}\right\} \tag{3.4}$$

Then C_1^2 and C_2^2 can be expressed as:

$$\left.\begin{aligned} C_1^2 = C_L^2 &= \frac{(\lambda + \mu)}{\rho} \\ C_2^2 = C_T^2 &= \frac{\mu}{\rho} \end{aligned}\right\} \tag{3.5}$$

Where, ∇^2 mentioned in Equation (3.4) is the Laplacian operator, ϕ is the scalar potential and $\boldsymbol{\psi}$ is the vector potential; ρ shown in Equation (3.5) is the density, C_L is the

longitudinal wave speed, C_T is the transverse or shear wave speed, λ and μ are the Lamé's first and second constants. The second Equation in (3.4) has a vector laplacian that can be presented as:

$$\nabla^2\boldsymbol{\psi} = \begin{bmatrix} \dfrac{\partial^2\psi_r}{\partial r^2} + \dfrac{1}{r^2}\dfrac{\partial^2\psi_r}{\partial\theta^2} + \dfrac{\partial^2\psi_r}{\partial z^2} + \dfrac{1}{r}\dfrac{\partial\psi_r}{\partial r} - \dfrac{2}{r^2}\dfrac{\partial\psi_\theta}{\partial\theta} - \dfrac{\psi_r}{r^2} \\ \dfrac{\partial^2\psi_\theta}{\partial r^2} + \dfrac{1}{r^2}\dfrac{\partial^2\psi_\theta}{\partial\theta^2} + \dfrac{\partial^2\psi_\theta}{\partial z^2} + \dfrac{1}{r}\dfrac{\partial\psi_\theta}{\partial r} + \dfrac{2}{r^2}\dfrac{\partial\psi_r}{\partial\theta} - \dfrac{\psi_\theta}{r^2} \\ \dfrac{\partial^2\psi_z}{\partial r^2} + \dfrac{1}{r^2}\dfrac{\partial^2\psi_z}{\partial\theta^2} + \dfrac{\partial^2\psi_z}{\partial z^2} + \dfrac{1}{r}\dfrac{\partial\psi_z}{\partial r} \end{bmatrix} \tag{3.6}$$

$$\nabla^2\boldsymbol{\psi} = \begin{bmatrix} \nabla^2\psi_r \\ \nabla^2\psi_\theta \\ \nabla^2\psi_z \end{bmatrix} \tag{3.7}$$

Where, ∇^2 is the laplacian operator.

$$\nabla^2 = \frac{\partial^2}{\partial r^2} + \frac{1}{r}\frac{\partial}{\partial r} + \frac{1}{r^2}\frac{\partial^2}{\partial\theta^2} + \frac{\partial^2}{\partial z^2}$$

Going back to Equation (3.4) one can get:

$$\left.\begin{aligned}
\nabla^2\phi &= \frac{1}{C_L^2}\frac{\partial^2\phi}{\partial t^2} \\
\nabla^2\psi_r - \frac{2}{r^2}\frac{\partial\psi_\theta}{\partial\theta} - \frac{\psi_r}{r^2} &= \frac{1}{C_T^2}\frac{\partial^2\psi_r}{\partial t^2} \\
\nabla^2\psi_\theta + \frac{2}{r^2}\frac{\partial\psi_r}{\partial\theta} - \frac{\psi_\theta}{r^2} &= \frac{1}{C_T^2}\frac{\partial^2\psi_\theta}{\partial t^2} \\
\nabla^2\psi_z &= \frac{1}{C_T^2}\frac{\partial^2\psi_z}{\partial t^2}
\end{aligned}\right\} \qquad (3.8)$$

The displacement can be expressed in terms of a scalar and a vector potential as per toke-Helmholtz decomposition found in Rose (1999) and Kundu (2004):

$$\left.\begin{aligned}
u_r &= \frac{\partial\phi}{\partial r} + \frac{1}{r}\frac{\partial\psi_z}{\partial\theta} - \frac{\partial\psi_\theta}{\partial z} \\
u_\theta &= \frac{1}{r}\frac{\partial\phi}{\partial\theta} + \frac{\partial\psi_r}{\partial z} - \frac{\partial\psi_z}{\partial r} \\
u_z &= \frac{\partial\phi}{\partial z} + \frac{1}{r}\frac{\partial\left(r\psi_\theta\right)}{\partial r} - \frac{1}{r}\frac{\partial\psi_r}{\partial\theta}
\end{aligned}\right\} \qquad (3.9)$$

The stresses can be expressed in terms of displacement as in Achenbach (1973) and Kundu (2004):

$$
\left.
\begin{aligned}
\sigma_{rr} &= \lambda\left(\frac{\partial u_r}{\partial r} + \frac{u_r}{r} + \frac{1}{r}\frac{\partial u_\theta}{\partial \theta} + \frac{\partial u_z}{\partial z}\right) + 2\mu\frac{\partial u_r}{\partial r} \\
\sigma_{\theta\theta} &= \lambda\left(\frac{\partial u_r}{\partial r} + \frac{u_r}{r} + \frac{1}{r}\frac{\partial u_\theta}{\partial \theta} + \frac{\partial u_z}{\partial z}\right) + 2\mu\left(\frac{u_r}{r} + \frac{1}{r}\frac{\partial u_\theta}{\partial \theta}\right) \\
\sigma_{zz} &= \lambda\left(\frac{\partial u_r}{\partial r} + \frac{u_r}{r} + \frac{1}{r}\frac{\partial u_\theta}{\partial \theta} + \frac{\partial u_z}{\partial z}\right) + 2\mu\frac{\partial u_z}{\partial z} \\
\sigma_{r\theta} &= \mu\left(\frac{\partial u_\theta}{\partial r} - \frac{u_\theta}{r} + \frac{1}{r}\frac{\partial u_r}{\partial \theta}\right) \\
\sigma_{\theta z} &= \mu\left(\frac{1}{r}\frac{\partial u_z}{\partial \theta} + \frac{\partial u_\theta}{\partial z}\right) \\
\sigma_{zr} &= \mu\left(\frac{\partial u_r}{\partial z} + \frac{\partial u_z}{\partial r}\right)
\end{aligned}
\right\} \qquad (3.10)
$$

Also, the stresses can be expressed in terms of potentials by substituting Equation (3.9) into (3.10) to yield:

$$
\left.
\begin{aligned}
\sigma_{rr} &= \lambda\nabla^2\phi + 2\mu\left(\frac{\partial^2\phi}{\partial r^2} - \frac{\partial^2\psi_\theta}{\partial r\,\partial z} - \frac{1}{r^2}\frac{\partial\psi_z}{\partial\theta} + \frac{1}{r}\frac{\partial^2\psi_z}{\partial r\partial\theta}\right)\\
\sigma_{r\theta} &= \mu\left(\frac{2}{r}\frac{\partial^2\phi}{\partial r\,\partial\theta} - \frac{2}{r^2}\frac{\partial\phi}{\partial\theta} - \frac{1}{r}\frac{\partial\psi_r}{\partial z} + \frac{\partial^2\psi_r}{\partial r\partial z} + \frac{1}{r}\frac{\partial^2\psi_\theta}{\partial\theta\partial z} + \frac{1}{r^2}\frac{\partial^2\psi_z}{\partial\theta^2} + \frac{1}{r}\frac{\partial\psi_z}{\partial r} - \frac{\partial^2\psi_z}{\partial r^2}\right)\\
\sigma_{zr} &= \mu\left(-\frac{1}{r^2}\psi_\theta - \frac{\partial^2\psi_\theta}{\partial z^2} + \frac{1}{r^2}\frac{\partial\psi_r}{\partial\theta} + \frac{1}{r}\frac{\partial^2\psi_z}{\partial\theta\partial z} + \frac{1}{r}\frac{\partial\psi_\theta}{\partial r} + 2\frac{\partial^2\phi}{\partial z\,\partial\theta} - \frac{1}{r}\frac{\partial^2\psi_r}{\partial r\partial\theta} + \frac{\partial^2\psi_\theta}{\partial r^2}\right)
\end{aligned}
\right\} \qquad (3.11)
$$

According to Achenbach (1973) and Kundu (2004) the displacement potential can be expressed as:

$$
\left.
\begin{aligned}
\phi &= \Phi(r)\cos\left(m\theta + \theta_0\right)e^{j\left(k_z z - \omega t\right)}\\
\psi_r &= \Psi_r(r)\sin\left(m\theta + \theta_0\right)e^{j\left(k_z z - \omega t\right)}\\
\psi_\theta &= \Psi_\theta(r)\cos\left(m\theta + \theta_0\right)e^{j\left(k_z z - \omega t\right)}\\
\psi_z &= \Psi_z(r)\sin\left(m\theta + \theta_0\right)e^{j\left(k_z z - \omega t\right)}
\end{aligned}
\right\} \qquad (3.12)
$$

θ_0 is a constant and m is an integer. As mentioned above that there are four (4) displacement components one scalar and three vector potentials: ϕ, ψ_r, ψ_θ and ψ_z. Substituting governing Equations (3.12) into Equation (3.8) yields the following Equations:

$$\left.\begin{aligned} \Phi'' + \frac{1}{r}\Phi' + \left(p^2 - \frac{m^2}{r^2}\right)\Phi = 0 \\ \psi_z'' + \frac{1}{r}\Psi_z' + \left(q^2 - \frac{m^2}{r^2}\right)\Psi_z = 0 \\ \psi_r'' + \frac{1}{r}\Psi_r' + \left(q^2 - \frac{(m+1)^2}{r^2}\right)\Psi_r = 0 \end{aligned}\right\} \qquad (3.13)$$

The terms p and q can be expressed as:

$$p = \sqrt{\frac{\omega^2}{C_L^2} - K_z^2} \qquad \text{and} \qquad q = \sqrt{\frac{\omega^2}{C_T^2} - K_z^2}$$

The solution of these Equations is Bessel Equation of the first or the second kind and m the order of the Bessel Equations. They can be written as:

$$\left.\begin{aligned}
\Phi(\mathrm{r}) &= A_1 J_m(pr) + A_2 Y_m(pr) \\
\psi_{\mathrm{r}}(\mathrm{r}) &= B_1 J_{m+1}(qr) + B_2 Y_{m+1}(qr) \\
\psi_{\mathrm{z}}(\mathrm{r}) &= C_1 J_m(qr) + C_2 Y_m(qr) \\
\psi_{\theta}(\mathrm{r}) &= -\psi_{\mathrm{r}}(\mathrm{r}) = -D_1 J_{m+1}(qr) - D_2 Y_{m+1}(qr)
\end{aligned}\right\} \qquad (3.14)$$

Substituting Equations in (3.12) into the Equation in (3.11) yields:

$$\left.\begin{aligned}
\sigma_{\mathrm{rr}} &= \mu\sigma_{11}(\mathrm{r})\cos\left(\mathrm{m}\theta + \theta_0\right)e^{jk_z} \\
\sigma_{\mathrm{r}\theta} &= \mu\sigma_{12}(\mathrm{r})\sin\left(\mathrm{m}\theta + \theta_0\right)e^{jk_z} \\
\sigma_{\mathrm{rz}} &= \mu\sigma_{13}(\mathrm{r})\cos\left(\mathrm{m}\theta + \theta_0\right)e^{jk_z}
\end{aligned}\right\} \qquad (3.15)$$

Where, σ_{11}, σ_{12} and σ_{13} are given as per Kundu (2004):

$$\left.\begin{aligned}
\sigma_{11}(\mathrm{r}) &= \left[\frac{2\mathrm{m}^2}{\mathrm{r}^2} - \left(\mathrm{q}^2 - \mathrm{k}_z^2\right)\right]\Phi - \frac{2}{\mathrm{r}}\Phi' + 2\mathrm{jk}_z\Psi'_{\mathrm{r}} \\
&\quad - \frac{2\,\mathrm{m}}{\mathrm{r}^2}\Psi_z + \frac{2\,\mathrm{m}}{\mathrm{r}}\Psi'_z \\
\sigma_{12}(\mathrm{r}) &= \frac{2\mathrm{m}}{\mathrm{r}^2}\left(\Phi - \mathrm{r}\Phi'\right) - \mathrm{jk}\left(\frac{1+\mathrm{m}}{\mathrm{r}}\right)\Psi_{\mathrm{r}} + \left[\mathrm{q}^2\right. \\
&\quad \left. - \frac{2\mathrm{m}^2}{\mathrm{r}^2}\right]\Psi_z + \mathrm{jk}_z\Psi'_{\mathrm{r}} + \frac{2}{\mathrm{r}}\Psi'_z \\
\sigma_{13}(\mathrm{r}) &= \left(\mathrm{k}_z - \mathrm{q}^2 - \left(\frac{\mathrm{m}(1+\mathrm{m})}{\mathrm{r}^2}\right)\right)\Psi_{\mathrm{r}} - \frac{\mathrm{m}}{\mathrm{r}}\Psi'_{\mathrm{r}} \\
&\quad + 2\mathrm{jk}_z\Phi' + \mathrm{jk}_z\frac{\mathrm{m}}{\mathrm{r}}\Psi_z
\end{aligned}\right\} \qquad (3.16)$$

Substituting Equation (3.14) into Equation (3.15) yields:

$$\boldsymbol{\sigma} = \mathbf{D}(m, k, \omega)\mathbf{A} \tag{3.17}$$

Where, $\boldsymbol{\sigma}$ is the stress vector, σ_{rr}, σ_{rz}, $\sigma_{r\theta}$, $\mathbf{D}$ is a matrix whose elements are expressed in terms of the circumferential order m, wave number k and angular frequency ω.

Equation (3.17) is presented as:

$$\left.\begin{aligned}\begin{bmatrix}\sigma_{rr}\\ \sigma_{rz}\\ \sigma_{r\theta}\end{bmatrix} &= \begin{bmatrix}D_{11} & D_{12} & D_{13} & D_{14} & D_{15} & D_{16}\\ D_{21} & D_{22} & D_{23} & D_{24} & D_{25} & D_{26}\\ D_{31} & D_{32} & D_{33} & D_{34} & D_{35} & D_{36}\end{bmatrix}\mathbf{A}\\ \mathbf{A} &= \begin{bmatrix}A_1 & B_1 & C_1 & A_2 & B_2 & C_2\end{bmatrix}^T\end{aligned}\right\} \tag{3.18}$$

3.3 WAVES IN PIPES

3.3.1 Axial Waves in Pipes

As stated above that these waves have symmetrical and non-symmetrical motions along the pipe. The symmetrical waves include the longitudinal and torsional and the anti-symmetric waves are basically the flexural waves.

Taking into account the traction-free condition on the inner and outer surfaces $r = a$ and $r = b$ yield the following eigenvalue problem which is presented in kundo (2004). By setting the determinant to zero, the dispersion Equation can be obtained which yields the following:

$$\begin{bmatrix} D_{11} & D_{12} & D_{13} & D_{14} & D_{15} & D_{16} \\ D_{21} & D_{22} & D_{23} & D_{24} & D_{25} & D_{26} \\ D_{31} & D_{32} & D_{33} & D_{34} & D_{35} & D_{36} \\ D_{41} & D_{42} & D_{43} & D_{44} & D_{45} & D_{46} \\ D_{51} & D_{52} & D_{53} & D_{54} & D_{55} & D_{56} \\ D_{61} & D_{62} & D_{63} & D_{64} & D_{65} & D_{66} \end{bmatrix} \begin{bmatrix} A_1 \\ B_1 \\ C_1 \\ A_2 \\ B_2 \\ C_2 \end{bmatrix} = 0 \tag{3.19}$$

$$D_{11} = \left[\frac{2m(m-1)}{r^2} + k_z^2 - q^2 \right] J_m(pr) + \frac{2p}{r} J_{m+1}(pr)$$

$$D_{12} = 2jk_z \left[qJ_m(qr) - \frac{(m+1)}{r} J_{m+1}(qr) \right]$$

$$D_{13} = 2m \left[\frac{(m-1)}{r^2} J_m(qr) - \frac{q}{r} J_{m+1}(qr) \right]$$

$$D_{14} = \left[\frac{2m(m-1)}{r^2} + k_z^2 - q^2 \right] Y_m(pr) + \frac{2p}{r} Y_{m+1}(pr)$$

$$D_{15} = 2jk_z \left[qY_m(qr) - \frac{(m+1)}{r} Y_{m+1}(qr) \right]$$

$$D_{16} = 2m \left[\frac{(m-1)}{r^2} Y_m(qr) - \frac{q}{r} Y_{m+1}(qr) \right]$$

$$D_{21} = 2jk_z\left[\frac{m}{r}J_m(pr) - pJ_{m+1}(pr)\right]$$

$$D_{22} = -\frac{qm}{r}J_m(qr) + \left(q^2 - k_z^2\right)J_{m+1}(qr)$$

$$D_{23} = \frac{\left(jk_z m\right)}{r}J_m(qr)$$

$$D_{24} = 2jk_z\left[\frac{m}{r}Y_m(pr) - pY_{m+1}(pr)\right]$$

$$D_{25} = -\frac{qm}{r}Y_m(qr) + \left(q^2 - k_z^2\right)Y_{m+1}(qr)$$

$$D_{26} = \frac{\left(jk_z m\right)}{r}Y_m(qr)$$

$$D_{31} = -2m\left[\frac{(m-1)}{r^2}J_m(pr) - \frac{p}{r}J_{m+1}(pr)\right]$$

$$D_{32} = jk_z\left[qJ_m(qr) - \frac{2(m+1)}{r}J_{m+1}(qr)\right]$$

$$D_{33} = \left[q^2 - \frac{2m(m-1)}{r^2}\right]J_m(qr) - \frac{2q}{r}J_{m+1}(qr)$$

$$D_{34} = -2m\left[\frac{(m-1)}{r^2}Y_m(pr) - \frac{p}{r}Y_{m+1}(pr)\right]$$

$$D_{35} = jk_z\left[qY_m(qr) - \frac{2(m+1)}{r}Y_{m+1}(qr)\right]$$

$$D_{36} = \left[q^2 - \frac{2m(m-1)}{r^2}\right]Y_m(qr) - \frac{2q}{r}Y_{m+1}(qr)$$

For the terms D_{11} to D_{36}, $r = b$; $D41$ to D_{66} are similar to $D_{11} - D_{36}$ but $r = a$.

3.3.1.1 Longitudinal Waves

The displacement is in the radial and axial direction *(r, z)* and no displacement along the circumferential direction (θ). To satisfy these constraints C_n, order m and θ_0 are set to zero in the general solution and leave A_n and B_n. Then Equation in (3.19) can be presented as:

$$\begin{bmatrix} D_{11} & D_{12} & D_{14} & D_{15} \\ D_{21} & D_{22} & D_{24} & D_{25} \\ D_{41} & D_{42} & D_{44} & D_{45} \\ D_{51} & D_{52} & D_{54} & D_{55} \end{bmatrix} \begin{bmatrix} A_1 \\ B_1 \\ A_2 \\ B_2 \end{bmatrix} = 0 \tag{3.20}$$

To solve this Equation the determinant must vanish which yields the dispersion Equations.

3.3.1.2 Torsional Waves

Motion of torsional waves are along the circumferential (θ) direction, therefore the only displacement component that exist in the Equations is the component related to θ. To satisfy this constraint, A_n, B_n, m and $\theta = 90^0$ must be set to zero and leave C_n. Then Equation (3.19) can be expressed as:

$$\begin{bmatrix} D_{33} & D_{36} \\ D_{63} & D_{66} \end{bmatrix} \begin{bmatrix} C_1 \\ C_2 \end{bmatrix} = 0 \tag{3.21}$$

3.3.1.3 Flexural Waves

Flexural modes are solved by calculating the whole Equation (3.19) to get solutions for each circumferential order n. To satisfy this Equation, m is set to 1 and θ_0 to 0.

3.3.2 Circumferential Guided Waves

These waves propagate along the circumference of the pipe in the θ direction along the (r, θ) space and there will be no axial propagation which is basically the z direction. Therefore, the displacement field can be described in terms of the radial and the circumferential direction only as there will be no propagation along the axial direction z. So the defect can only be detected by this type of wave only if the defect is located where the wave is propagating circumferentially. The displacement potential can be expressed as Kundu (2004):

$$\phi = \Phi(\mathrm{r})\exp\left[j\left(k_\theta\theta - \omega t\right)\right]$$
$$\psi_z = \Psi_z(\mathrm{r})\exp\left[j\left(k_\theta\theta - \omega t\right)\right] \tag{3.22}$$

Eliminating the terms that are associated with z direction Equation (3.9) and rewriting it in Equation (3.23) to describe the displacement fields in the radial and circumferential directions in terms of the potentials ψ and ϕ as:

$$\left.\begin{aligned} u_r &= \frac{\partial \phi}{\partial r} + \frac{1}{r}\frac{\partial \psi}{\partial \theta}\ , \\ u_\theta &= \frac{1}{r}\frac{\partial \phi}{\partial \theta} - \frac{\partial \psi}{\partial r}\ , \\ u_z &= 0 \end{aligned}\right\} \qquad (3.23)$$

Substituting Equations in (3.22) into the first and last Equation in (3.8) one gets the Equations for circumferential guided wave in terms of the potential ψ and ϕ as:

$$\left.\begin{aligned} \left(\frac{\partial^2}{\partial r^2} + \frac{1}{r}\frac{\partial}{\partial r} + \frac{1}{r^2}\frac{\partial^2}{\partial \theta^2}\right)\phi &= \frac{1}{C_L^2}\frac{\partial^2 \phi}{\partial t^2} \\ \left(\frac{\partial^2}{\partial r^2} + \frac{1}{r}\frac{\partial}{\partial r} + \frac{1}{r^2}\frac{\partial^2}{\partial \theta^2}\right)\psi_z &= \frac{1}{C_T^2}\frac{\partial^2 \psi_z}{\partial t^2} \end{aligned}\right\} \qquad (3.24)$$

Equation (3.24) can be re-written as:

$$\left.\begin{aligned} \Phi'' + \frac{1}{r}\Phi' + \left[\left(\frac{\omega}{C_L}\right)^2 - \left(\frac{K_\theta}{r}\right)^2\right]\Phi &= 0 \\ \psi_z'' + \frac{1}{r}\psi_z' + \left[\left(\frac{\omega}{C_T}\right)^2 - \left(\frac{K_\theta}{r}\right)^2\right]\psi_z &= 0 \end{aligned}\right\} \qquad (3.25)$$

These are Bessel Equations and their general solutions is given as:

$$\left.\begin{aligned}\Phi(\mathrm{r}) &= A_1 J_{k_\theta}\left(\frac{\omega}{C_L}r\right) + A_2 Y_{k_\theta}\left(\frac{\omega}{C_L}r\right)\\ \psi_z(\mathrm{r}) &= B_1 J_{k_\theta}\left(\frac{\omega}{CT}r\right) + B_2 Y_{k_\theta}\left(\frac{\omega}{CT}r\right)\end{aligned}\right\} \qquad (3.26)$$

J_{k_θ} and Y_{k_θ} are the first and second kind of Bessel functions.

Assuming $\sigma_{rr} = \sigma_{r\theta} = 0$, we will have:

$$\begin{bmatrix} D_{11} & D_{12} & D_{13} & D_{14} \\ D_{21} & D_{22} & D_{23} & D_{24} \\ D_{31} & D_{32} & D_{33} & D_{34} \\ D_{41} & D_{42} & D_{43} & D_{44} \end{bmatrix} \begin{bmatrix} A_1 \\ A_2 \\ B_1 \\ B_2 \end{bmatrix} = 0 \qquad (3.27)$$

A_1, A_2, B_1, and B_2 in Equation (3.27) are constants that can be determined by satisfying the boundary conditions given as: $\sigma_{rr} = \sigma_{r\theta} = 0$ at the inner and outer radius of the pipe; this referred to as traction-free boundary.

The characteristic Equations or the dispersion Equations can be expressed as shown below:

$$D_{11} = J_{K_\theta - 2}\left(\frac{\omega r}{KC_T}\right) - 2\left(K^2 - 1\right)J_{K_\theta}\left(\frac{\omega r}{KC_T}\right) + J_{K_\theta + 2}\left(\frac{\omega r}{KC_T}\right)$$

$$D_{12} = jK^2\left(J_{K_\theta - 2}\left(\frac{\omega r}{C_T}\right) - J_{K_\theta + 2}\left(\frac{\omega r}{C_T}\right)\right)$$

$$D_{13} = J_{Y_\theta - 2}\left(\frac{\omega r}{KC_T}\right) - 2\left(\mathrm{K}^2 - 1\right)Y_{K_\theta}\left(\frac{\omega r}{KC_T}\right) + Y_{K_\theta + 2}\left(\frac{\omega r}{KC_T}\right)$$

$$D_{14} = jK^2\left(J_{K_\theta - 2}\left(\frac{\omega r}{C_T}\right) - J_{K_\theta + 2}\left(\frac{\omega r}{C_T}\right)\right)$$

$$D_{21} = j\left(J_{K_\theta - 2}\left(\frac{\omega r}{KC_T}\right) - J_{K_\theta + 2}\left(\frac{\omega r}{KC_T}\right)\right)$$

$$D_{22} = K^2\left(J_{K_\theta - 2}\left(\frac{\omega r}{C_T}\right) + J_{K_\theta + 2}\left(\frac{\omega r}{C_T}\right)\right)$$

$$D_{23} = j\left(Y_{K_\theta - 2}\left(\frac{\omega r}{KC_T}\right) - Y_{K_\theta + 2}\left(\frac{\omega r}{KC_T}\right)\right)$$

$$D_{24} = K^2\left(Y_{K_\theta - 2}\left(\frac{\omega r}{C_T}\right) + Y_{K_\theta + 2}\left(\frac{\omega r}{C_T}\right)\right)$$

$$D_{31} = J_{K_\theta - 2}\left(\frac{\omega r}{KC_T}\right) - 2\left(K^2 - 1\right)J_{K_\theta}\left(\frac{\omega r}{KC_T}\right) + J_{K_\theta + 2}\left(\frac{\omega r}{KC_T}\right)$$

$$D_{32} = jK^2\left(J_{K_\theta - 2}\left(\frac{\omega r}{C_T}\right) - J_{K_\theta + 2}\left(\frac{\omega r}{C_T}\right)\right)$$

$$D_{33} = J_{Y_\theta - 2}\left(\frac{\omega r}{KC_T}\right) - 2\left(K^2 - 1\right)Y_{K_\theta}\left(\frac{\omega r}{KC_T}\right) + Y_{K_\theta + 2}\left(\frac{\omega r}{KC_T}\right)$$

$$D_{34} = jK^2\left(J_{K_\theta - 2}\left(\frac{\omega r}{C_T}\right) - J_{K_\theta + 2}\left(\frac{\omega r}{C_T}\right)\right)$$

$$D_{41} = j\left(J_{K_\theta - 2}\left(\frac{\omega r}{KC_T}\right) - J_{K_\theta + 2}\left(\frac{\omega r}{KC_T}\right)\right)$$

$$D_{42} = K^2\left(J_{K_\theta - 2}\left(\frac{\omega r}{C_T}\right) + J_{K_\theta + 2}\left(\frac{\omega r}{C_T}\right)\right)$$

$$D_{43} = j\left(Y_{K_\theta - 2}\left(\frac{\omega r}{KC_T}\right) - Y_{K_\theta + 2}\left(\frac{\omega r}{KC_T}\right)\right)$$

$$D_{44} = K^2\left(Y_{K_\theta - 2}\left(\frac{\omega r}{C_T}\right) + Y_{K_\theta + 2}\left(\frac{\omega r}{C_T}\right)\right)$$

3.4 DISPERSION CURVES

Here are some of the results obtained using *PCDISP* program (Seco et al., 2007) for the calculation of the cutoff frequencies and the corresponding dispersive curves for the longitudinal, torsioanl and flexural modes for a steel pipe with the following input parameters:

Poisson's ratio : $\nu = .29$;

Density (kg/m^3) : $\rho = 7900$

Internal radius (m) : $a = 16.468e-3$

External radius (m) : $b = 17.68e-3$

3.4.1 Longitudinal Modes Dispersion Curves

3.4.1.1 Cutoff Frequencies for the Phase Speed Curves

L(0,1): cutoff = 0 kHz

L(0,2): cutoff = 49.8999 kHz

L(0,3): cutoff = 1560.36 kHz

L(0,4): cutoff = 2222.05 kHz

L(0,5): cutoff = 3395.64 kHz

L(0,6): cutoff = 3951.4 kHz

3.4.1.2 Dispersion Curves

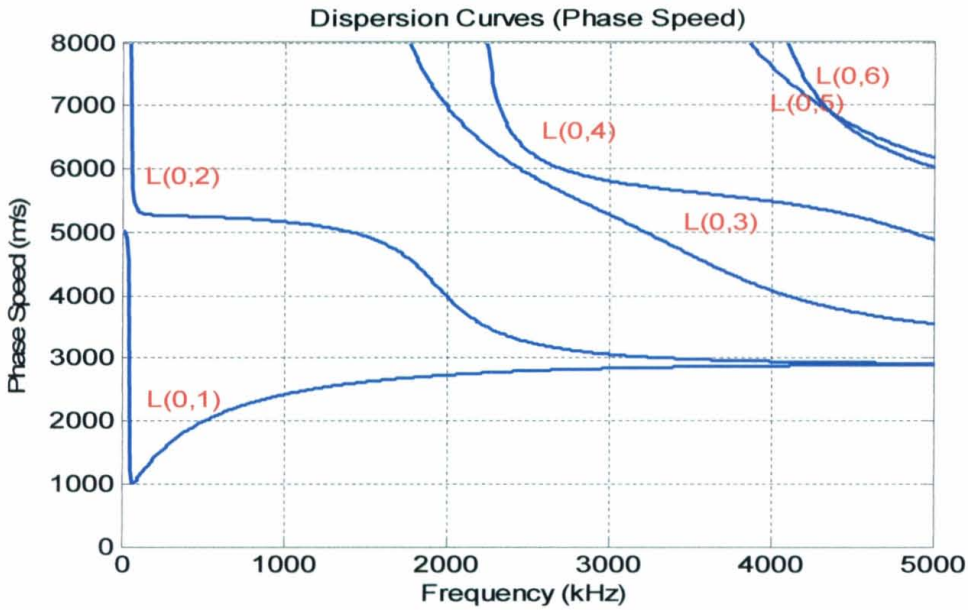

Figure 3.6 - Phase Speed Curves for Longitudinal Modes.

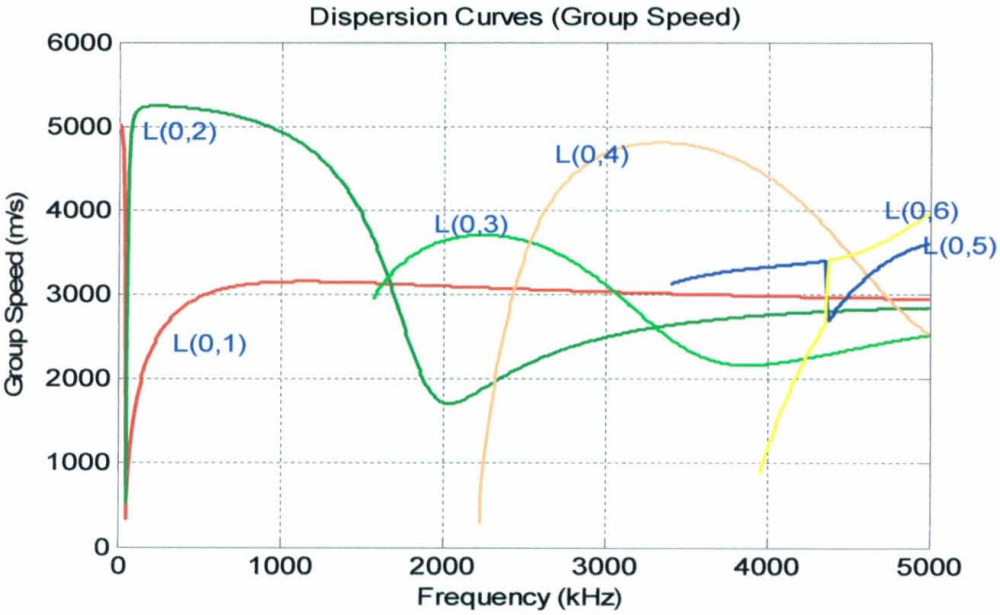

Figure 3.7 – Group Speed Curves for Longitudinal Modes.

3.4.2 Torsional Modes Dispersion Curves

3.4.2.1 Cutoff Frequencies for the Phase Speed Curves

T(0,1): cutoff = 0 kHz

T(0,2): cutoff = 1002.37 kHz

T(0,3): cutoff = 2002.39 kHz

T(0,4): cutoff = 3002.94 kHz

T(0,5): cutoff = 4003.62 kHz

3.4.2.2 Dispersion Curves

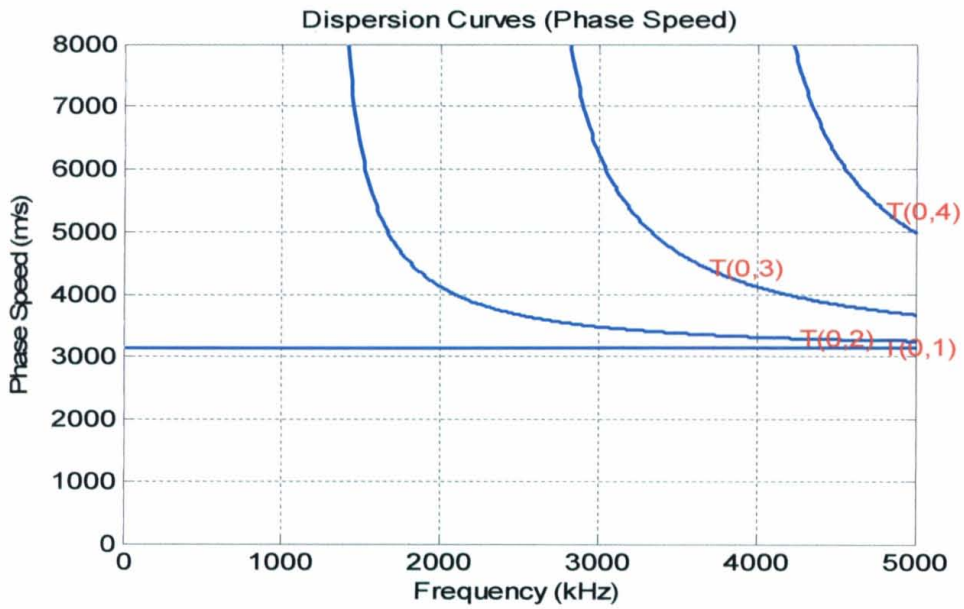

Figure 3.8 - Phase Speed Curves for Torsional Modes.

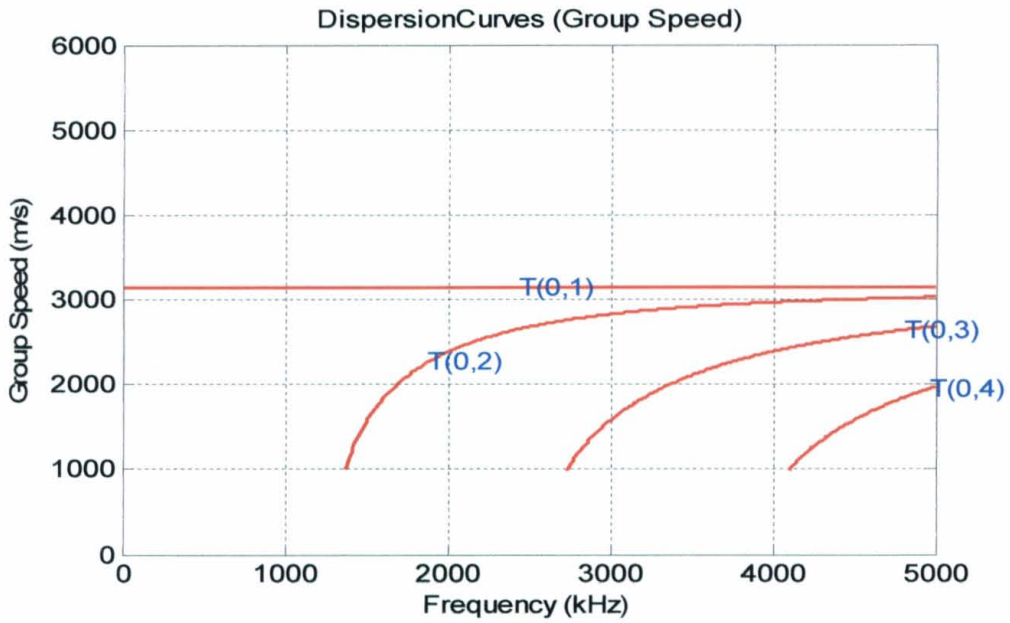

Figure 3.9 – Group Speed Curves for Torsional Modes.

3.4.3 Dispersion Curves Flexural N = 1 Modes

3.4.3.1 Cutoff Frequencies for the Phase Speed Curves

F(1,1): cutoff = 0 kHz

F(1,2): cutoff = 31.3643 kHz

F(1,3): cutoff = 70.3452 kHz

F(1,4): cutoff = 1002.78 kHz

F(1,5): cutoff = 1147.07 kHz

F(1,6): cutoff = 1631.37 kHz

F(1,7): cutoff = 2002.6 kHz

F(1,8): cutoff = 2493.6 kHz

F(1,9): cutoff = 2900.91 kHz

F(1,10): cutoff = 3003.08 kHz

F(1,11): cutoff = 4003.72 kHz

F(1,12): cutoff = 4033.36 kHz

F(1,13): cutoff = 4179.78 kHz

3.4.3.2 Dispersion Curves

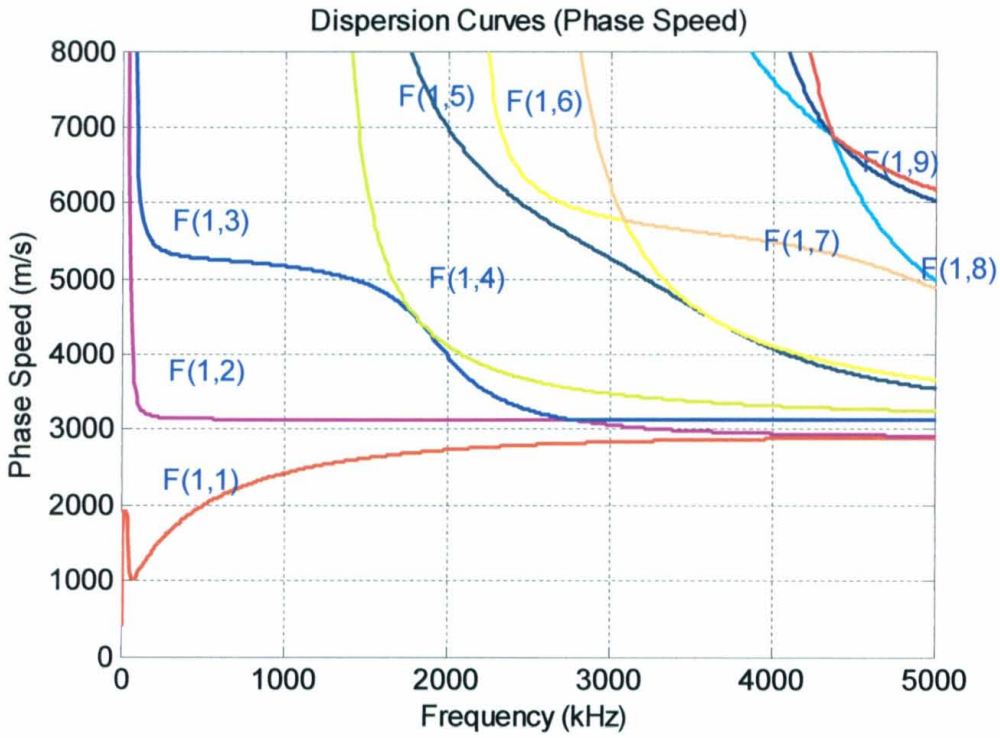

Figure 3.10 - Phase Speed Curves for Flexural Modes, n=1

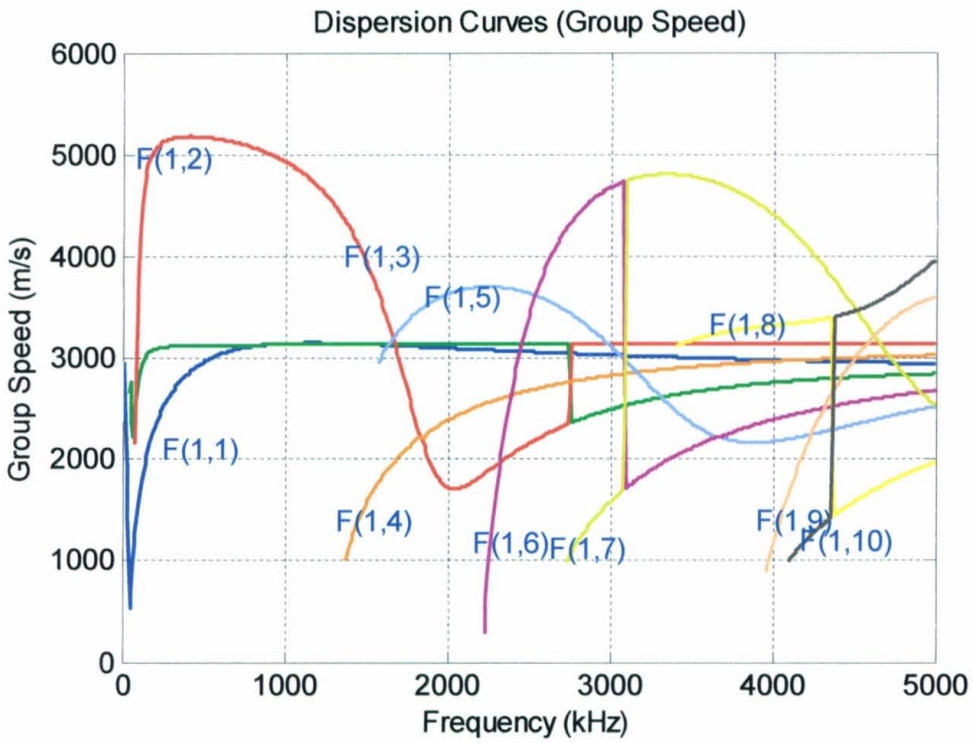

Figure 3.11 - Group Speed Curves for Flexural Modes, n=1

3.4.4 Dispersion Curves Flexural N = 3 Modes

3.4.4.1 Cutoff Frequencies

F(3,1): cutoff = 9.0393 kHz

F(3,2): cutoff = 88.1533 kHz

F(3,3): cutoff = 167.619 kHz

F(3,4): cutoff = 1006.07 kHz

F(3,5): cutoff = 1158.15 kHz

F(3,6): cutoff = 1631.39 kHz

F(3,7): cutoff = 2004.27 kHz

F(3,8): cutoff = 2499.14 kHz

F(3,9): cutoff = 2901.9 kHz

F(3,10): cutoff = 3004.19 kHz

F(3,11): cutoff = 4004.55 kHz

F(3,12): cutoff = 4034.64 kHz

F(3,13): cutoff = 4182.12 kHz

3.4.4.2 Dispersion Curves

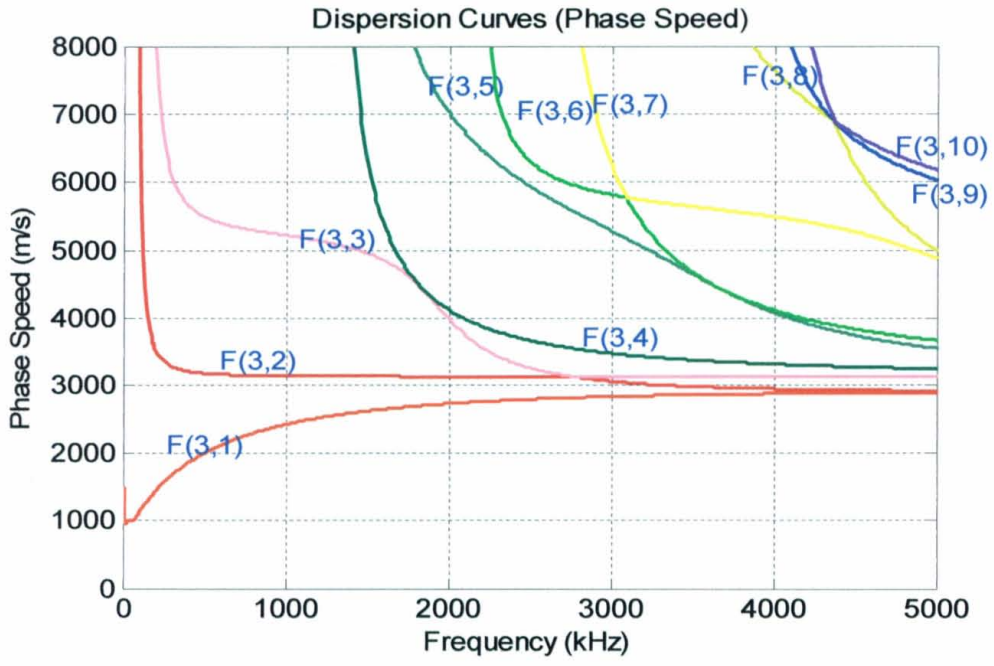

Figure 3.12 – Phase Speed Curves for Flexural Modes, n=3

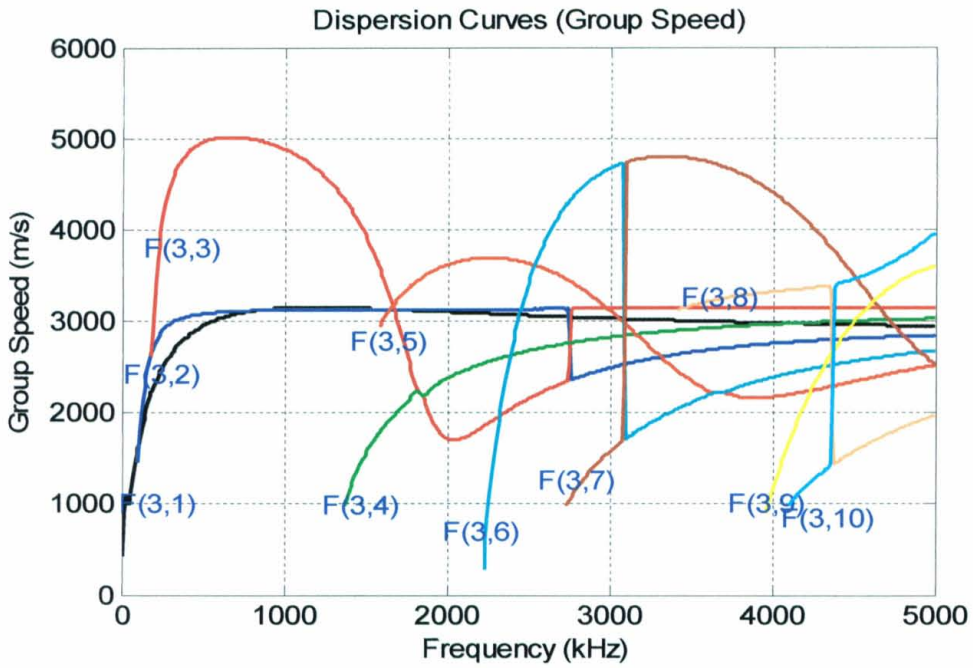

Figure 3.13 – Group Speed Curves for Flexural Modes, n=3

3.5 DEFECTS APPROXIMATION METHODS

The transmitted waves that interact with the flaw produce scattered waves which can be used to characterize the flaw in terms of extent and shape. There are several approximation methods cited in the literature that can provide an approximation of the amplitude of the scattered waves from the flaws. Each method has its shortcoming and advantages. Such methods include Finite Element Method (FEM), Born Approximation method, T Matrix method, Boundary Element Method (BEM) and Kirchhoff Approximations method (Schmerr & Song, 2007).

The Born approximation method was first developed for quantum mechanics and later used for scattering problem. The BEM can provide a very good approximation of the flaw but when dealing with 3-D scattering problem it becomes tedious and time consuming. The T-Matrix method only approximates non-cylindrical and non-spherical shapes while the FEM relies heavily on the creation of mesh with discreet points placed throughout the body being investigated.

The Kirchhoff approximations method can provide a very good approximation of the volumetric flaws and cracks. It does not necessarily provide an accurate approximation of the last arriving waves from the flaw but it can very accurately model the leading edge response of the flaw. Although, it cannot predict the exact size but it can provide a reliable and meaningful approximation of the flaw that can be used as a qualitative measure to assess the reliability of the monitored structure.

This research will be based on Kirchhoff approximations method to approximate the extent of defects like cracks and voids embedded in pipes.

The pulse-echo far filed scattering of circular cracks or spherical voids provides a very good measure in assessing and describing the flaw. Since all the flaws in a pipe will have almost a curved shape they occur along eh circumference of the pipe. Although the shape may have one of its dimensions in the axial direction of the pipe but its width or length will resemble a curved shape. Hence, this method is feasible for application in this research.

3.5.1 The Kirchhoff Approximations of Cracks and Voids

To determine the extent of the flaw on a pipe, the Kirchhoff approximation will be utilized where the amplitude of the scattered wave for the surface of the flaw can be calculated for a volumetric flaw or a crack. Pulse-echo far-field scattering amplitude component versus frequency for a spherical flaw in the Kirchhoff approximation is given by Equation (3.28) (Schmerr & Song, 2007):

$$A(\omega) = -\frac{b}{2}\exp(-jkb)\left(\exp(-jkb) - \frac{\sin(kb)}{kb}\right) \tag{3.28}$$

$$k = \frac{2\pi f}{C}$$

Where k is the wave number, b is the radius of the flaw, f is the range of frequencies for the scattered wave and C is the speed of the wave.

The frequency response of the flaw Equation (3.28) is converted back to the time domain by taking the Inverse Fourier Transform (IFT) to obtain the impulse response of the flaw Equation (3.29).

$$a(t) = -\frac{b}{2}\left[\delta\left(t + \frac{2b}{C}\right) - \frac{C}{2b}U\left(-\frac{2b}{C}, 0; t\right)\right] \tag{3.29}$$

Where C is the wave speed; b is the radius of the flaw; δ: delta function, its amplitude

$U(t_1, t_2, t) = 1$, for $t_1 < t < t_2$, otherwise it is equals to zero. For crack the following Kirchhoff approximation can be used to estimate the extent of a crack. The amplitude of the scattered wave from the crack can be estimated as shown below:

$$A = \frac{jbCos\theta}{2\,Sin\theta} J_1\,(2\,kbSin\theta) \tag{3.30}$$

Here are some of the results for calculating the scattering filed of flaws with different radius sizes.

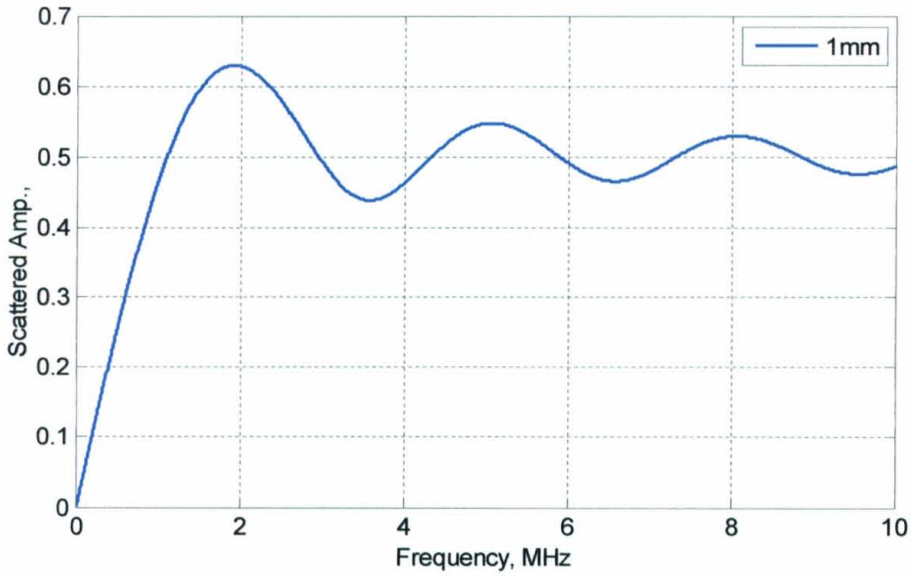

Figure 3.14 – Scattering Wave from a Flaw with a 1mm Radius.

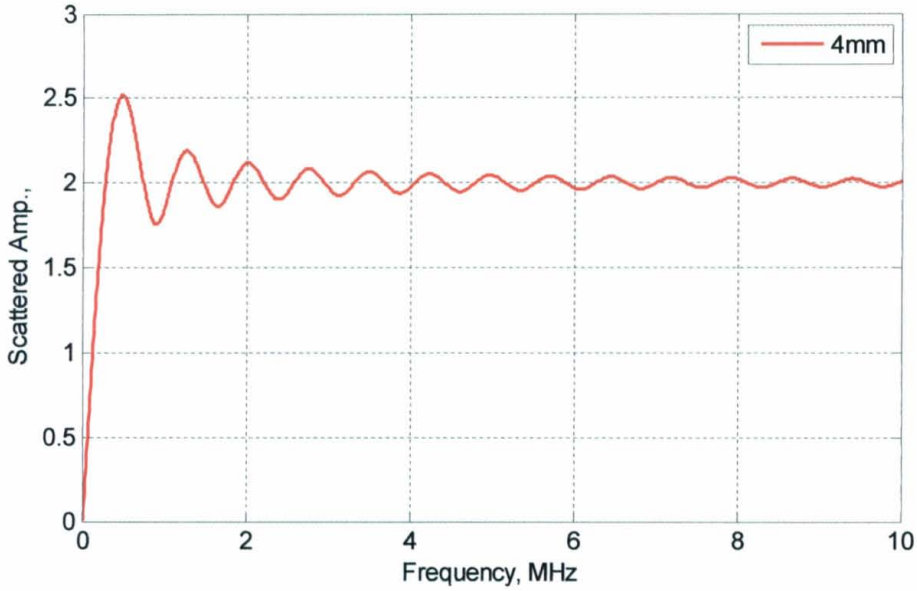

Figure 3.15 – Scattering Wave from a Flaw with a 4mm Radius.

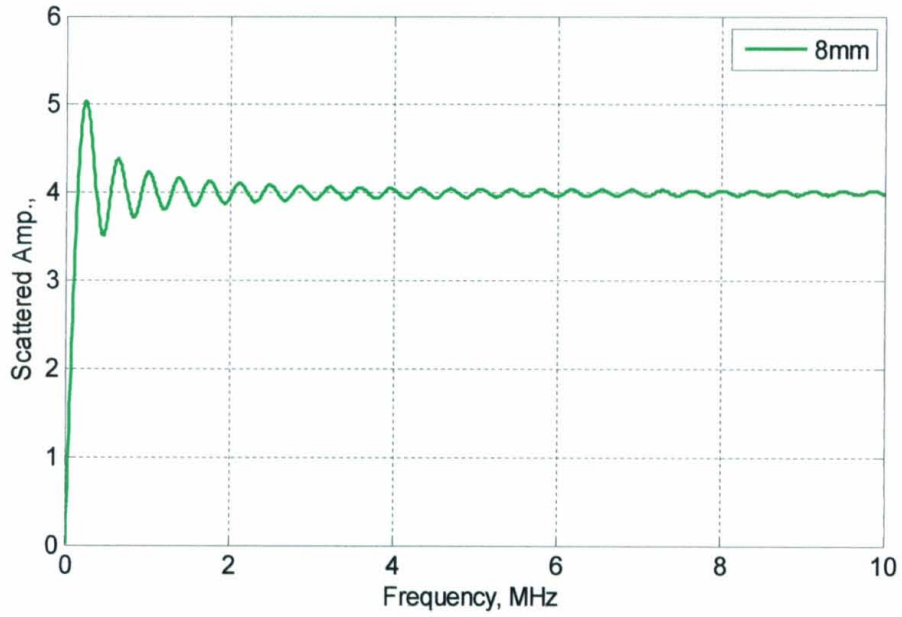

Figure 3.16 – Scattering Wave from a Flaw Having 8 mm Radius.

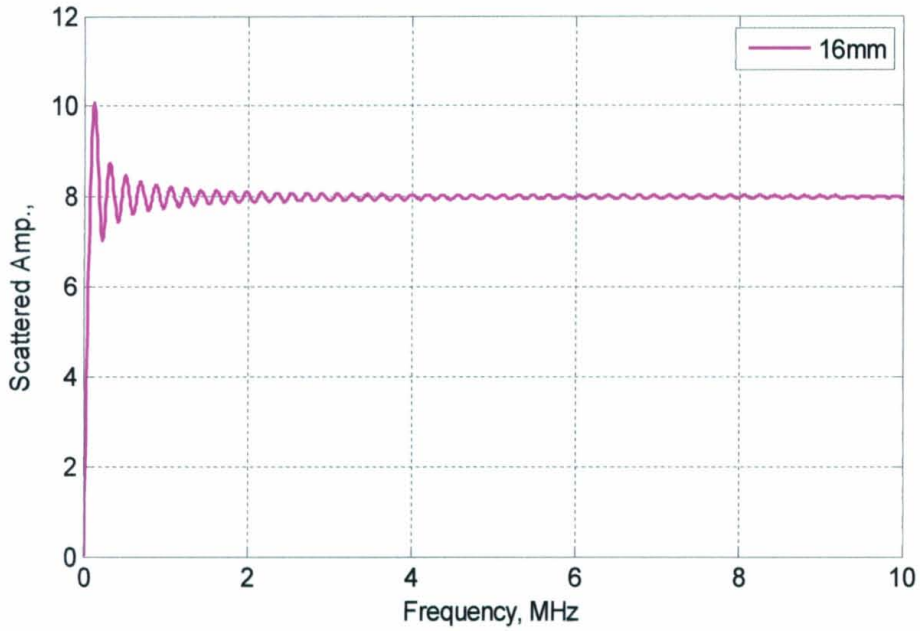

Figure 3.17 – Scattering Wave from a Flaw Having a 16mm Radius.

CHAPTER 4

SIGNAL PROCESSING AND THE FORMULATION OF FLAW ASSESSMENT MODEL

In this chapter, some basic concepts about Digital Signal Processing (DSP) for non-stationary signal will be provided. Fourier Transform, Discreet Fourier Transform (DFT), Fast Fourier Transforms (FFT), shortcoming of the DFT and ways to alleviate these shortcomings, windowing and aliasing will be discussed. Also, signal propagation in solids and the scattering signals from flaw will be discussed. The outcome of these discussions and the background information will be used to present a mathematical model to be used for locating and sizing a spherical flaw.

4.1 CONTINUOUS TIME FOURIER TRANSFORM (CTFT)

The Fourier Transform provides the frequency representation of a signal originally defined in the time domain. It is used to transform a continuous time signal into frequency domain. The Fourier transform *X(f)* of a continuous time function *x(t)* can be expressed as :

$$X(f) = \int_{-\infty}^{\infty} x(t)\, e^{-j2\pi ft}\, dt \tag{4.1}$$

The inverse transform is:

$$x(t) = \int_{-\infty}^{\infty} X(f)\, e^{j2\pi ft}\, df \qquad (4.2)$$

4.2 DISCRETE FOURIER TRANSFORM (DFT)

It is crucial that the signal is sampled at certain time intervals or frequency intervals to allow digital recording and gain a better understanding of signal during the analysis. As we are dealing with digital systems, the signals that are displayed for analysis in these systems should be digital, hence, it is always necessary that the signal to be presented in samples.

For a finite length signal x(n) the Discreet Fourier Transform (DFT) $X(\omega)$ is expressed as:

$$X(\omega) = \sum_{n=0}^{N-1} x(n) e^{-j\omega n} \qquad 0 \leq n \leq N-1 \qquad (4.3)$$

This is a finite length sequence having N values of frequency samples $X(\omega)$. In the analysis of a signal we need to get as much information as we can from the frequency content of the signal. The DFT is a very useful method that provides the frequency representation of a signal and makes the analysis easier to interpret .

Alternatively, the Discrete Fourier Transform (DFT) of the signal can be presented as shown below, by providing a simpler way that can provide a relationship between the DFT and the inverse DFT (Oppenheim & Schafer, 2010):

$$X(k) = \sum_{n=0}^{N-1} x(n) e^{-\frac{j2\pi nk}{N}}, \qquad 0 \leq k \leq N-1 \tag{4.4}$$

As noted above that the Discrete Fourier Transform (DFT) is a function that represents a number of frequency points over a finite length sequence. This is an N-point sequence defined in the region from *0* to *N -1*. *X(k)* is the DFT coefficient and *n* is an index number. As indicated above in the Equation that it is sufficient to have a length of a *N* for the sequence to provide frequency samples, the $X(\omega)$ values at N distinct points of ω_k, where k lies between *0* and *N-1*. The same thing applies to finding *x(n)* when performing the inverse Fourier transform as shown below. The inverse DFT which provides *x(n)* from *X(k)* can be defined as:

$$x(n) = \frac{1}{N} \sum_{k=0}^{N-1} X(k) e^{\frac{j2\pi}{N} kn}, \qquad 0 \leq n \leq N-1 \tag{4.5}$$

These Equations are simplified in another form as:

$$W_N = \exp\left(-\frac{j2\pi}{N}\right) \tag{4.6}$$

Taking this expression into the two Equations above:

$$X(k) = \sum_{n=0}^{N-1} x(n) W_N^{nk}, \qquad 0 \leq k \leq N-1 \tag{4.7}$$

and

$$x(n) = \frac{1}{N} \sum_{k=0}^{N-1} X(k) W_N^{-nk}, \qquad 0 \leq n \leq N-1 \tag{4.8}$$

4.2.1 Fast Fourier Transform

The Fast Fourier Transform (FFT) is more efficient computation algorithm that implements the discrete Fourier Transform with a greater efficiency and greater reduction in computation time. When using the FFT, the computation time can be reduced for an N-point DFT sequence from the order of N^2 to N log N. Typical N values will be 2^6 (64), 2^7 (128), 2^9 (512), 2^{10} (1024) 2^{11} (2048),.....etc.

The main intent of using the DFT is to approximate the Fourier transform of a continuous time process and it must be noted that the DFT has some shortcomings that may lead to wrong conclusions when analyzing the output results. Such problems are attributed to the three known phenomena about the DFT: (a) *leakage*, (b) aliasing, and (c) *the picket-fence effect.*

4.2.2 Leakage

This problem causes a spreading of the spectrum that can result in moving the highest frequency beyond the Nyquist frequency which may lead to aliasing. These two problems cannot be separated from each other. Therefore, the signal should be band limited to avoid such phenomenon from happening.

The method that is usually used to limit the length of the signal is the windowing technique. The selected window should be evaluated first to insure its effectiveness in minimizing the spreading of the signal. There are several window functions used by Digital Signal Processing (DSP) that will be addressed in the subsequent sections.

4.2.3 Aliasing

The phenomenon of aliasing causes the overlapping of signal samples which will lead to erroneous representation of the output signal. It causes ambiguity in the output results when analyzing the output signals. The only solution to the aliasing problem is to ensure that the sampling rate is high enough to avoid any spectral overlap, or to use an *anti-aliasing filters.*

The Sampling Theorem states that the input waveforms with frequencies below the half sampling rate can be reconstructed exactly while frequencies above the half the sampling rate become aliased as lower frequencies.

For frequencies just above the half the samplings rate, up to the sampling rate, the aliased frequency becomes:

$f_{alias} = f_{nyq} - |f_{actual} - f_{nyq}|$, where a kind of mirror-image takes place.

Referring to Figure (4.1), the waveform to be sampled is in blue, it is a 6 Hz sine wave and would therefore require greater than 12 Hz sampling rate to preserve the correct frequency in the reconstruction. The red line is the result of sampling at 10 Hz; the alias is therefore 5- abs (5-6) = 4 Hz.

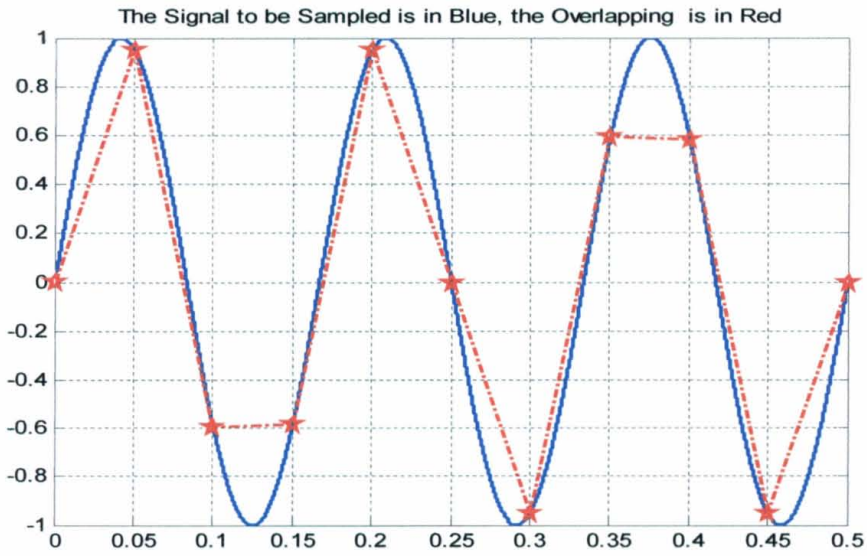

Figure 4.1 - Aliasing Effect.

4.2.4 Picket - Fence Effect

Since the spectrum can be observed at discrete points only, which will be looked at what is referred to as Picket-Fence Effect because we can observe the behaviors of the signal at discrete points.

Certain component could lie between two of the discrete transform lines, and the peak of this component might not be detected without some addition processing. So to reduce this effect is to vary the number of points in a time period by adding zeros at the end of the original record of the signal, while maintaining the original record unchanged.

This process changes the period, which in turn changes the locations of the spectral lines without altering the continuous form of the original spectrum. Consequently, the hidden spectral components can be shifted to points where they can be detected.

As demonstrated in Figure (4.2), that the hidden spectral components can be seen in the second plot.

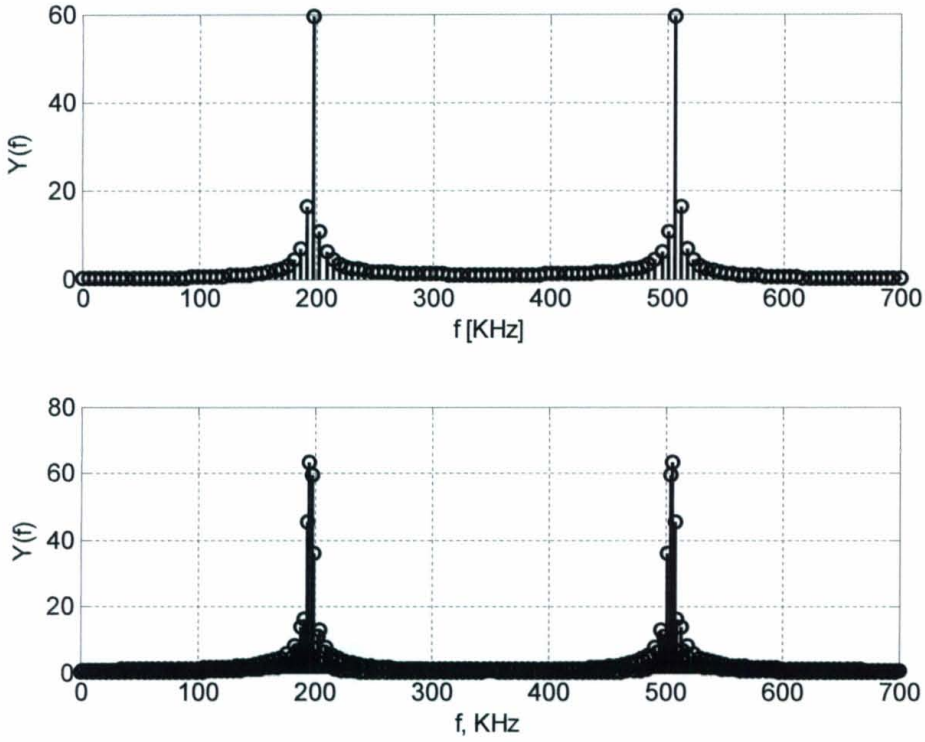

Figure 4.2 - Picket- Fence Effect.

In the latter plot the data points were padded with 7 times its original length to improve the picture. It simply allows the signal to appear more finely and it does not change the characteristics of the function and hence cannot change the resolution or the accuracy of the Discreet Fourier Transform.

4.3 SAMPLING, ALIASING AND NYQUIST THEOREM

When evaluating a function, it is always necessary to sample it because digital systems cannot process analogue or continuous functions. If the signal to be analyzed is analog in nature then it must be converted into digital form, as it is sampled, by an *analogue to digital* (A/D) converter. Figure (4.3) presents a continuous time signal, *x(t)*. It can be represented as a discrete time signal by using values of *x(t)* at intervals of nT_s to form *x[n]* as shown in Figure (4.4).

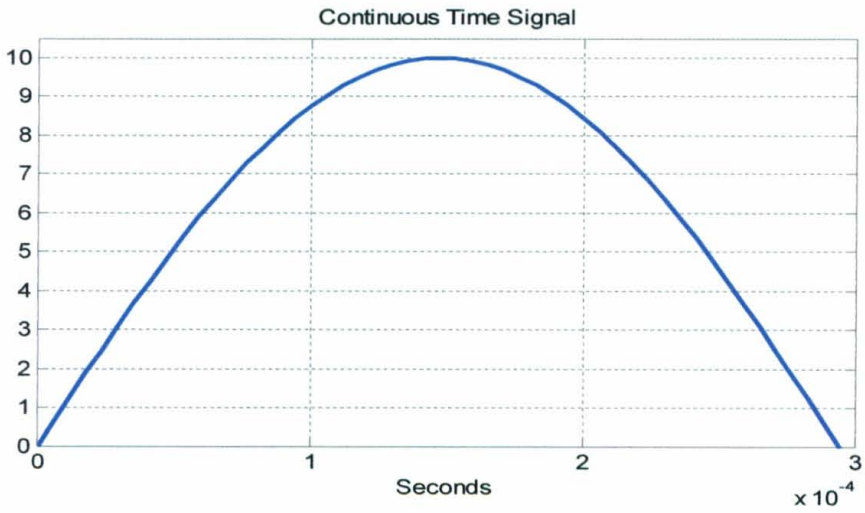

Figure 4.3 – Continuous Time Signal.

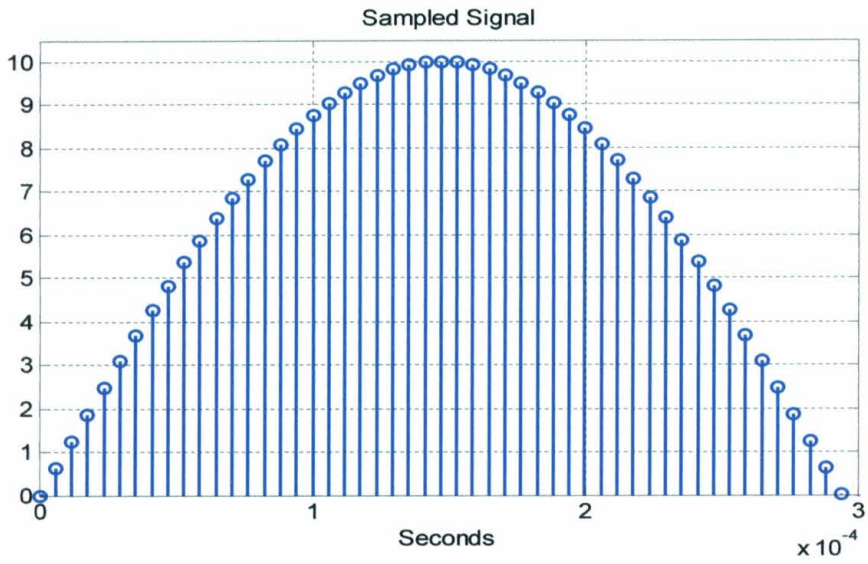

Figure 4.4 – Sampled Signal.

We are taking points from *x(t)* at regular intervals of time, T_s , called the *sampling intervals*. The frequency f_s is given by $f_s = 1/T_s$, (f_s is in Hertz) can be used in the frequency domain. If the sampling rates were high enough, then the signal *x(t)* could be reconstructed from *x[n]* by simply joining the points by small linear portions.

According to the *Nyquist Sampling Theorem,* aliasing can be avoided by having a sampling rate that is greater than or equal to twice the highest frequency presented in the signal. If the sampling rate is not high enough to sample the signal then a phenomenon called *aliasing* occurs.

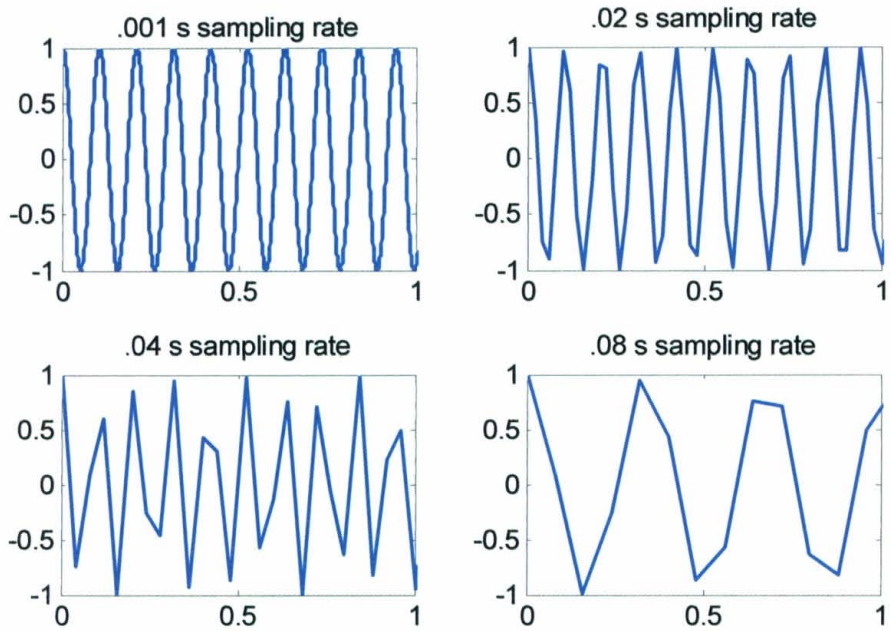

Figure 4.5 – The Effect of Different Sampling Rates.

Figure (4.5) shows the effect of different sampling rates for a sine signal in the time domain. Aliasing is basically the overlapping of the signals which leads to the distortion of the signal. This occurs when a continuous time signal has frequencies larger than half of the sampling rate. The process of aliasing describes the phenomenon in which components of the signal at high frequencies are confused for components at lower frequencies.

4.4 MATHEMATICAL MODEL FOR LOCATING AND SIZING THE FLAW

4.4.1 Flaw Size Estimation

Under this research, a simulation model has been developed to simulate propagating signals through a structure without and with a flaw. Equation (4.10) is the Equation that estimates the amplitude of the scattered waves reflected back from spherical flaws (Schmerr & Song, 2007).

$$A(\omega) = -\frac{b}{2}\exp(-jkb)\left(\exp(-jkb) - \frac{\sin(kb)}{kb}\right) \tag{4.10}$$

Figure (4.6) illustrates the scattering waves from spherical flaws with different radius sizes, 0 mm, 4 mm, 12 mm and 16 mm.

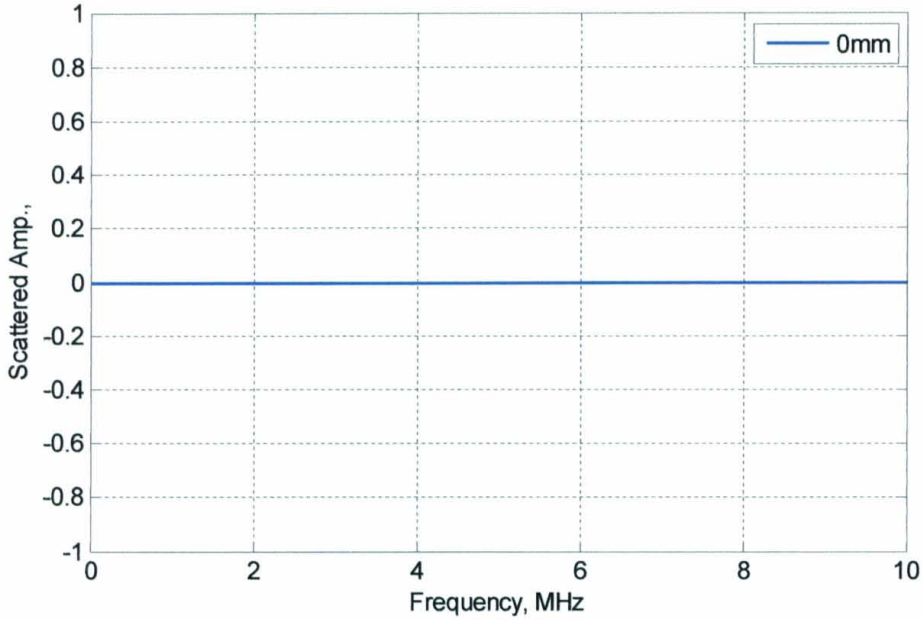

Figure 4.6 – Scattering Wave Response for a Flaw with 0 mm Radius.

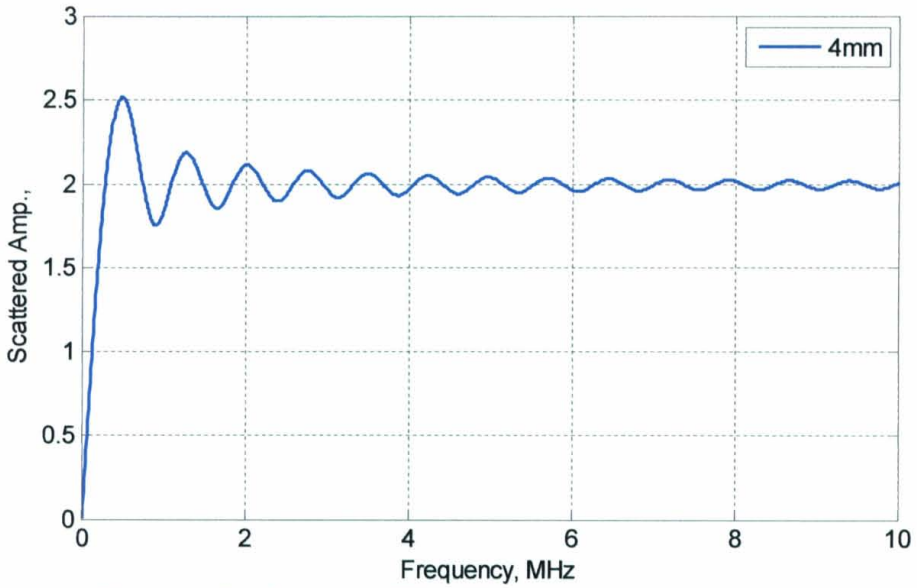

Figure 4.7 – Scattering Wave Response for a Flaw with 4 mm Radius.

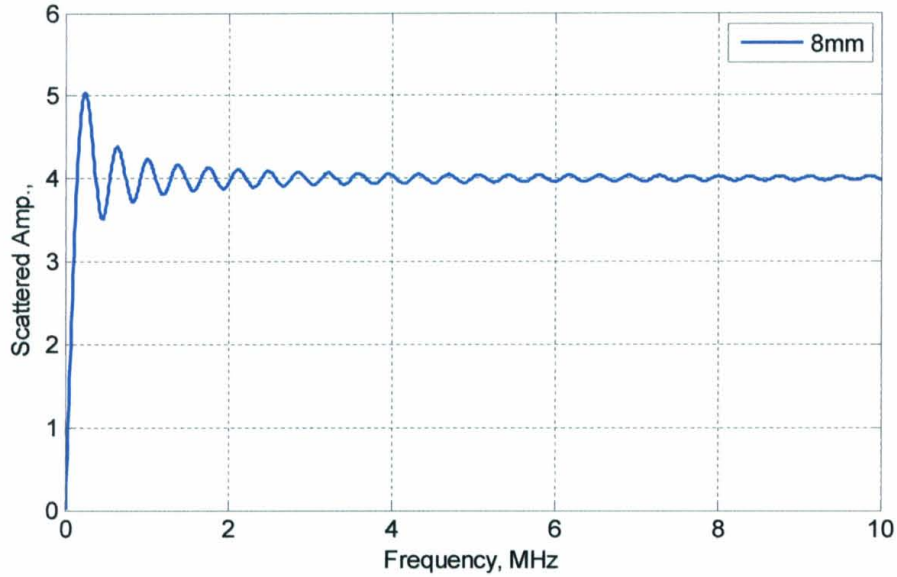

Figure 4.8 – Scattering Wave Response for a Flaw with 8 mm Radius.

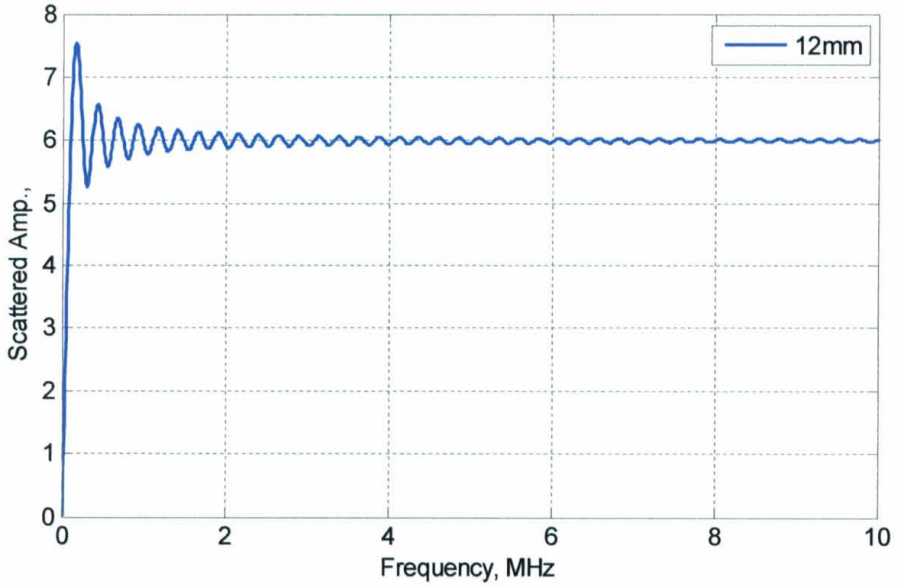

Figure 4.9 – Scattering Wave Response for a Flaw with 12 mm Radius.

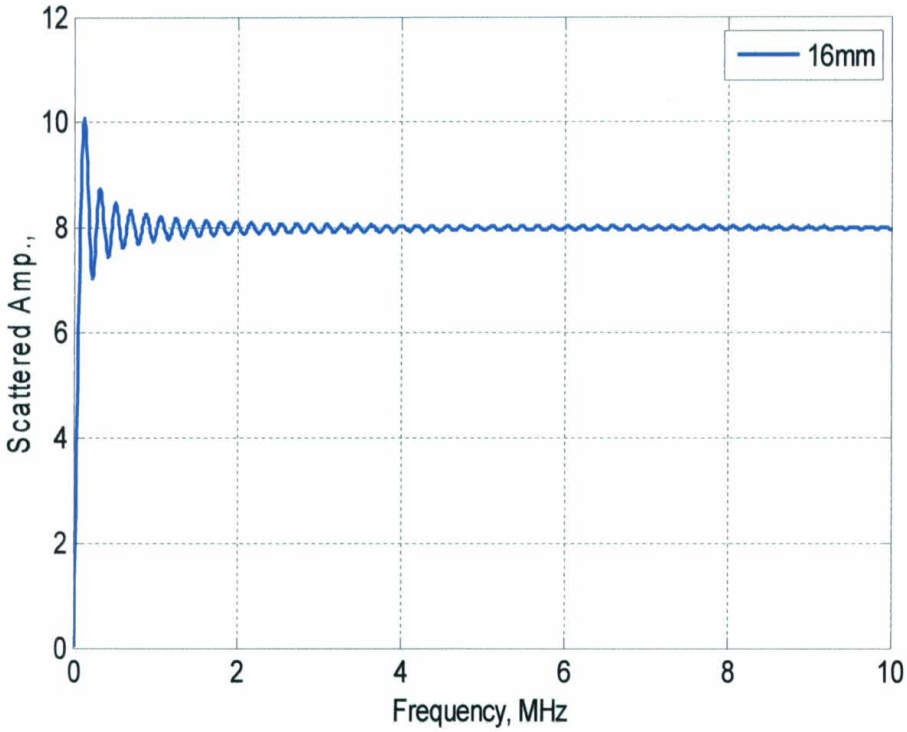

Figure 4.10 – Scattering Wave Response for a Flaw with 16 mm Radius.

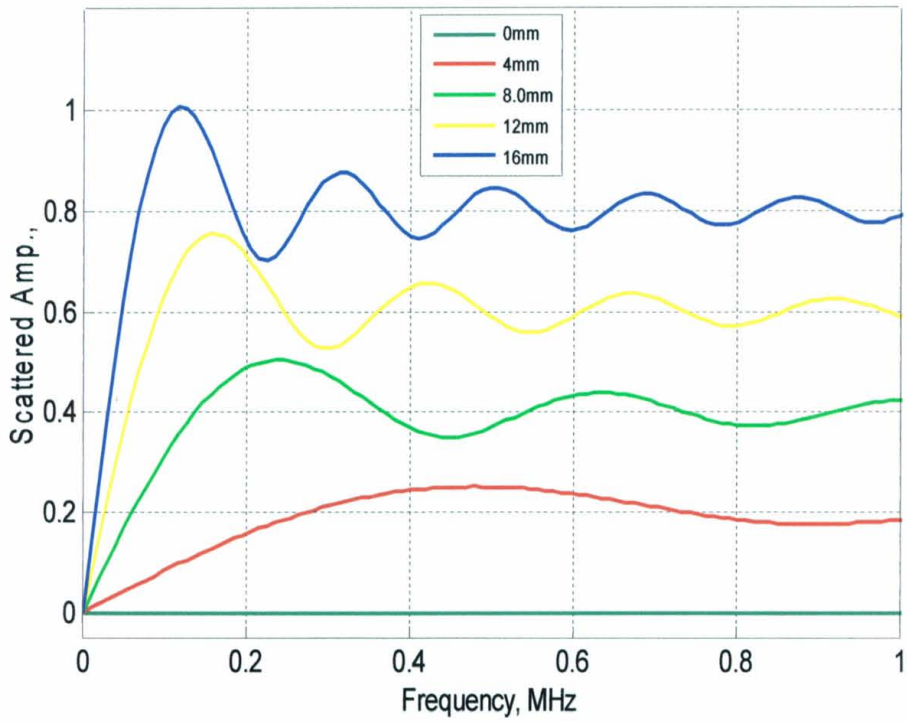

Figure 4.11 – Response of the Scattering Waves for Flaws with Radii 0, 4, 8, 12 and 16 mm.

Figure (4.11) shows that the amplitude is approximated as units of length. As the radius of the flaw increases, the amplitude of the frequency response increases. Also, as the radius of the flaw decreases the shape of the signal becomes wider in the frequency domain. In this research Equation (4.10) will be altered to calculate the amplitude as a ratio or as a coefficient by omitting the radius (b) term from the Equation. Then, it is multiplied by the original signal or the input signal to estimate the amount of attenuation and dispersion of the signal when it encounters a spherical flaw of radius b.

Equation (4.10) as it is presented calculates the scattering amplitudes and as the radius increases, the amplitude increases indicating a signal gain instead of attenuation. As the radius of the flaw decreases the response amplitude decreases. Equation (4.11) is the modified Equation is shown below:

$$\mathcal{A}_{sf}(\omega) = -\exp(-jkb)\left(exp(-jkb) - \frac{sin(kb)}{kb}\right) \tag{4.11}$$

$\mathcal{A}_{sf}$: is the spreading coefficient, it measures the amount of spread of the signal in frequency domain as a result of a spherical flaw, k is the wave number and b is the radius of the flaw. To get a better understanding of the change in the signal, this coefficient should be inverse Fourier transformed into the time domain. It should be noted that this equation calculates the pulse-echo far-field scattering amplitude of a flaws, that has an isotropic spherical shape with a given radius b, which is twice the real length of the flaw.

Referring to Figures below from Figure (4.12) up to Figure (4.23) explain the change in the frequency and time domains.

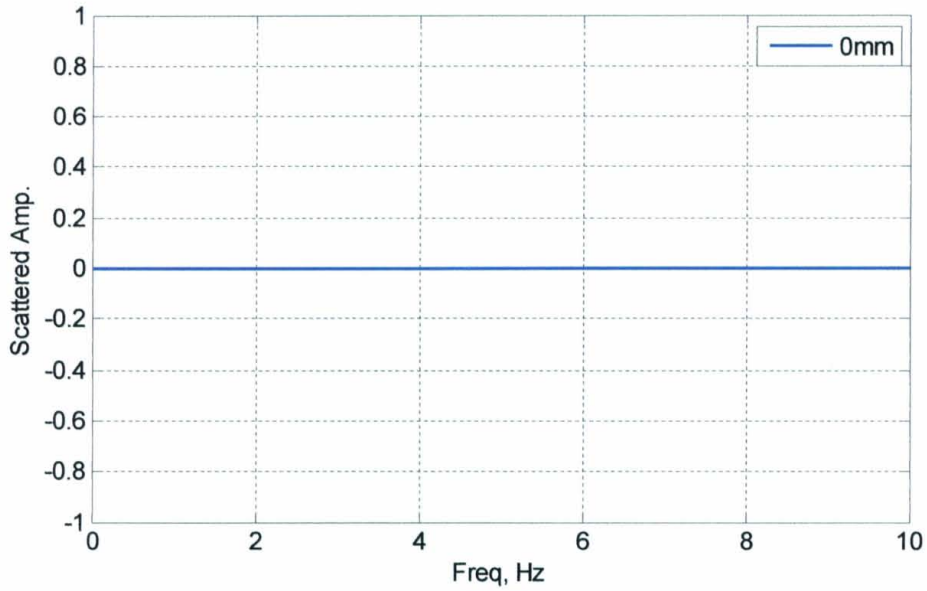

Figure 4.12a – Response of the Scattering Waves for a Flaw with 0 mm Radius – *(using the modified Equation).*

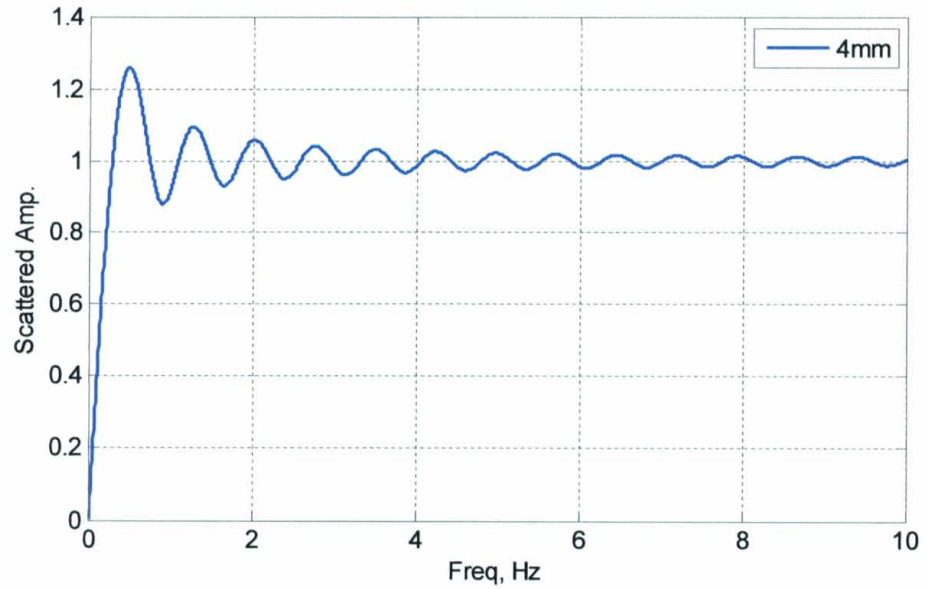

Figure 4.12b – Response of the Scattering Waves for a Flaw with 4 mm Radius – *(using the modified Equation).*

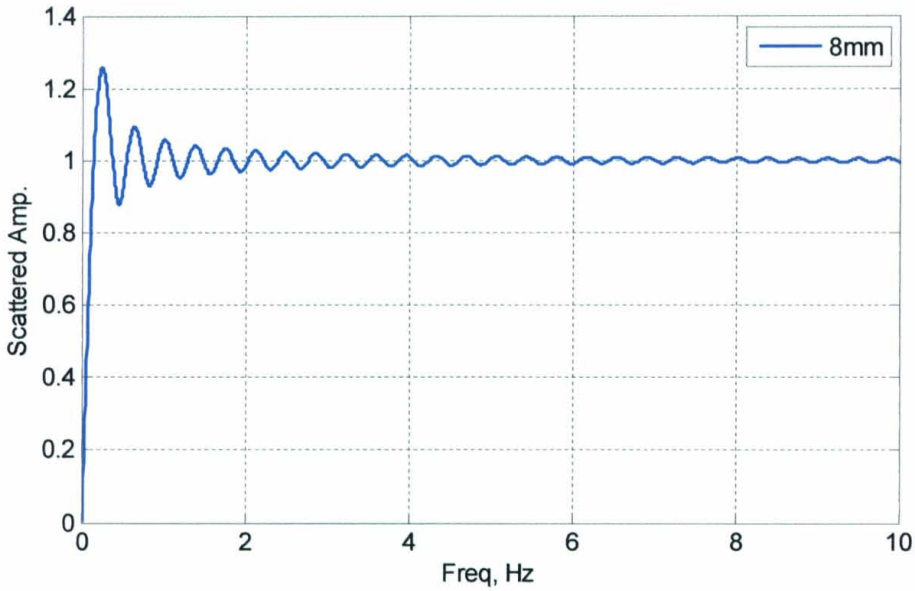

Figure 4.13a – Response of the Scattering Waves for a Flaw with 8 mm Radius – *(using the modified Equation).*

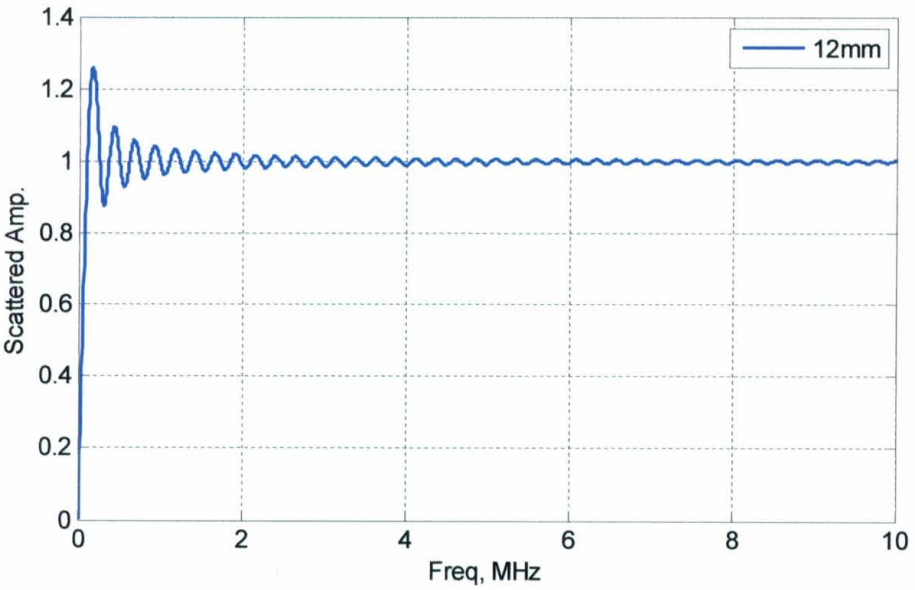

Figure 4.13b – Response of the Scattering Waves for a Flaw with 12 mm Radius – *(using the modified Equation).*

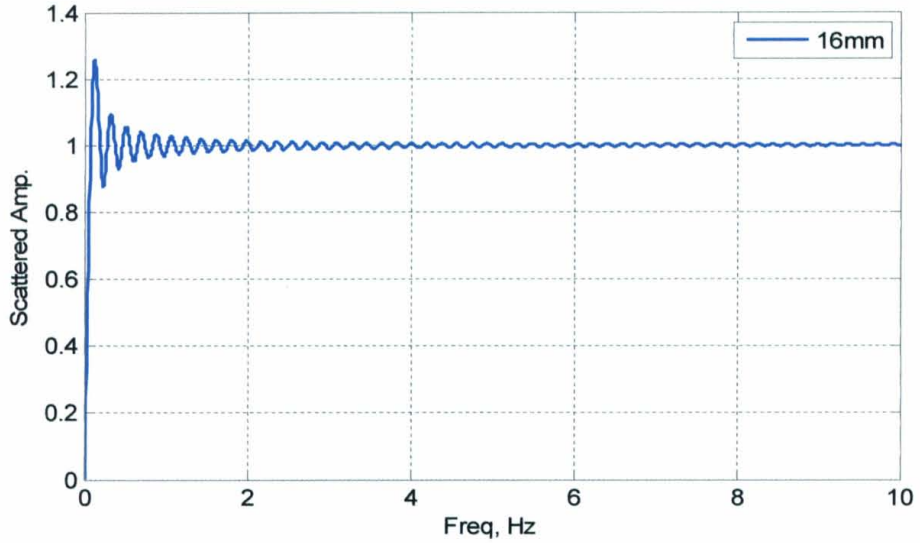

Figure 4.14a – Response of the Scattering Waves for a Flaw with 16 mm Radius – *(using the modified Equation).*

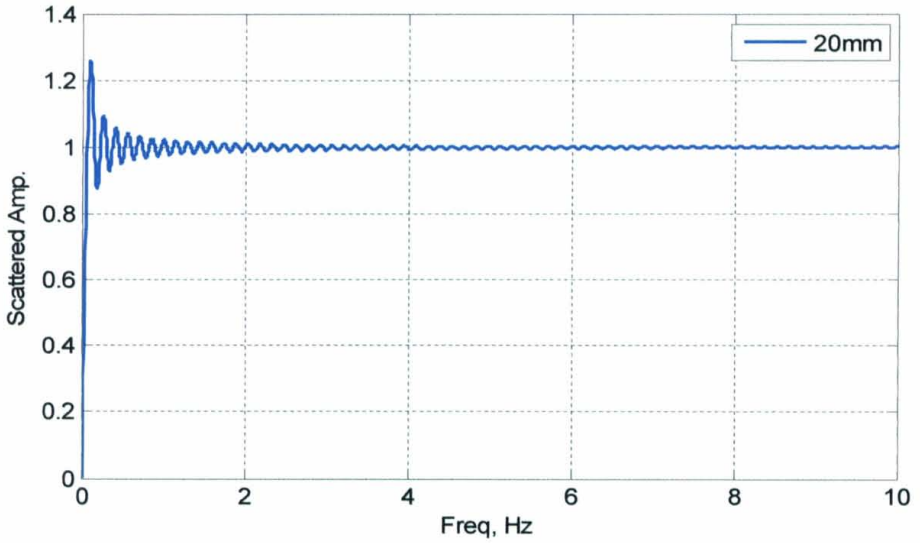

Figure 4.14b – Response of the Scattering Waves for a Flaw with 20 mm Radius – *(using the modified Equation).*

As noted from Figures (4.12), (4.13) and (4.14) that the amplitude is the same for all the responses for the different radii. The only difference is the spread of the signal. As the

radius increases the spread of the signal decreases and as the radius decreases, the spread of the signal increases; the Figure below, Figure (4.15) illustrates this fact.

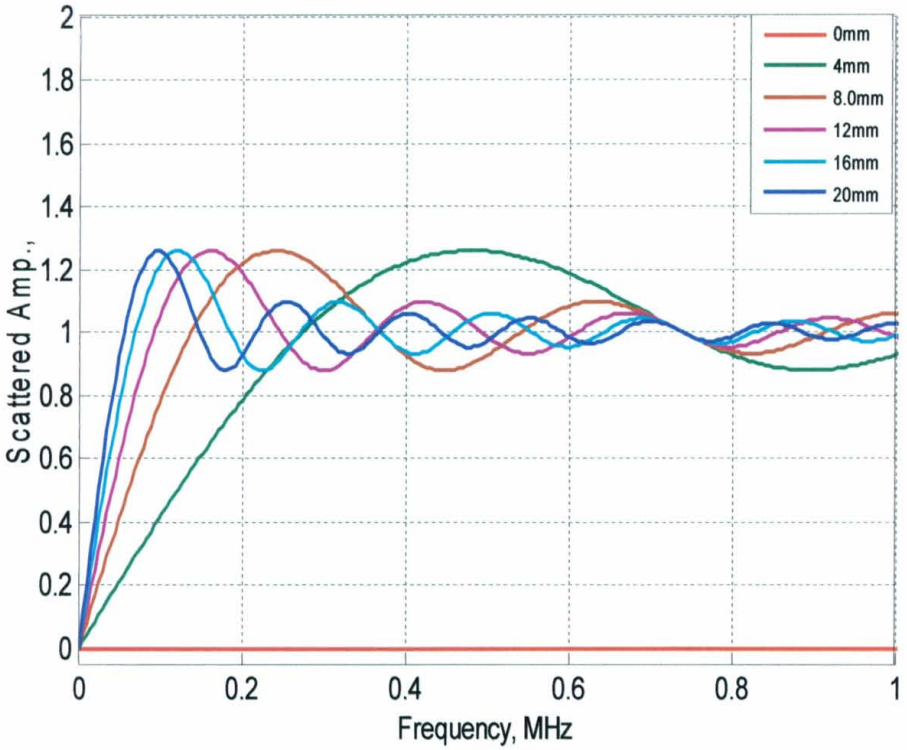

Figure 4.15 – Frequency Responses for Flaws with Radii 0, 4, 8, 12, 16 and 20 mm – (*using the modified Equation).*

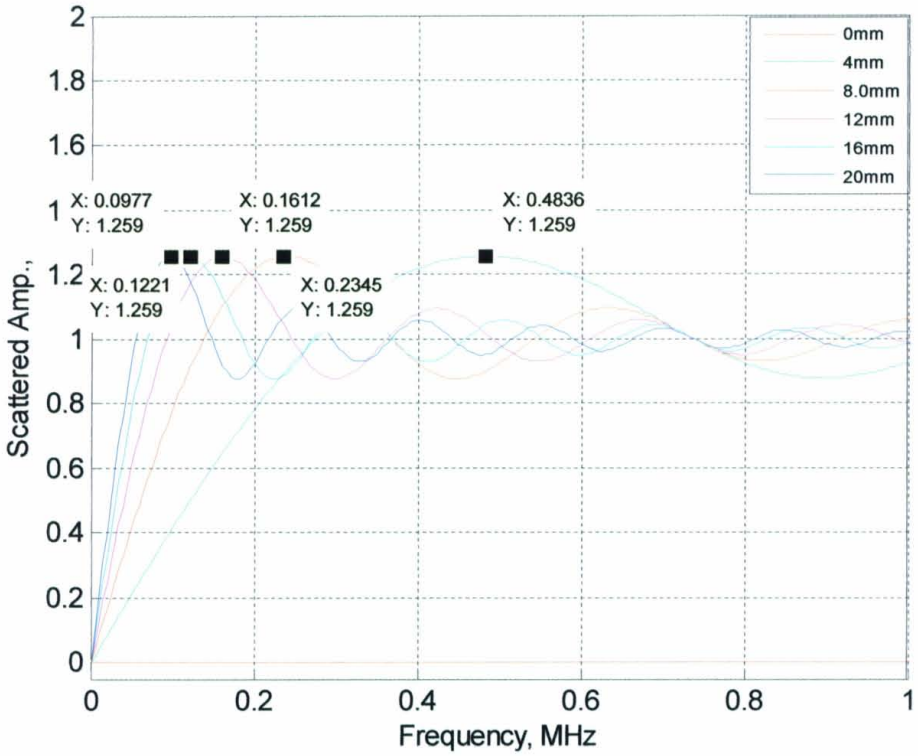

Figure 4.16 – Frequency Responses for Flaws with Radii 0, 4, 8, 12 16 and 20 mm – *Showing the Peak Values for each Response.*

As noted, that the increase in the radius causes the response to be narrower and the decrease in the radius results in a wider response. The amplitude is kept almost the same, constant over the range of all the frequencies presented in the plot.

In the time domain, the response will be the opposite, the larger the radius of the flaw the wider the response in the time domain and the lower the radius the narrower the response in the time domain. These facts are substantiated by Figures (4.17) to (4.23).

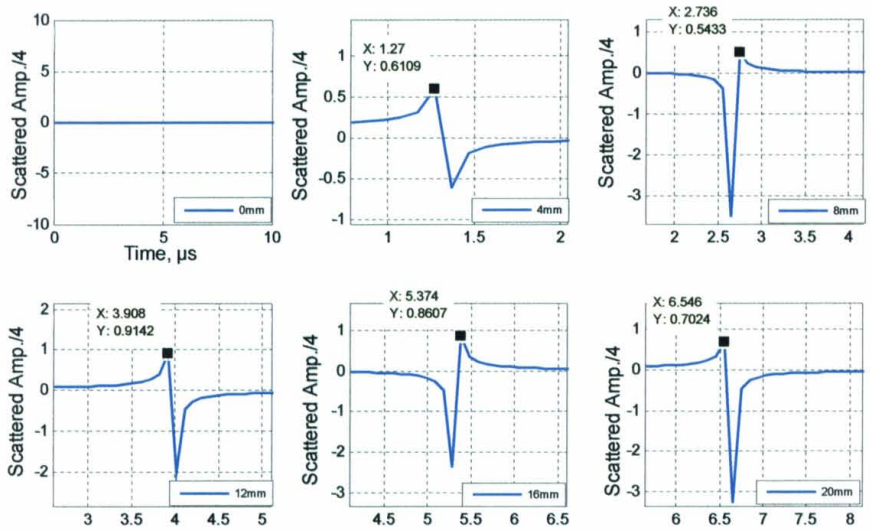

Figure 4.17 – Comparison of the Time Domain Responses of the Scattering Waves for Flaws with Radius Sizes 0, 4, 8, 12, 16 and 20 mm.

The Figure is re-plotted in a larger scale shown below in Figures (4.18) to (4.23) for each size of the flaw that clearly show that as the radius of the flaw increases, the time shift of the signal increases in the time domain.

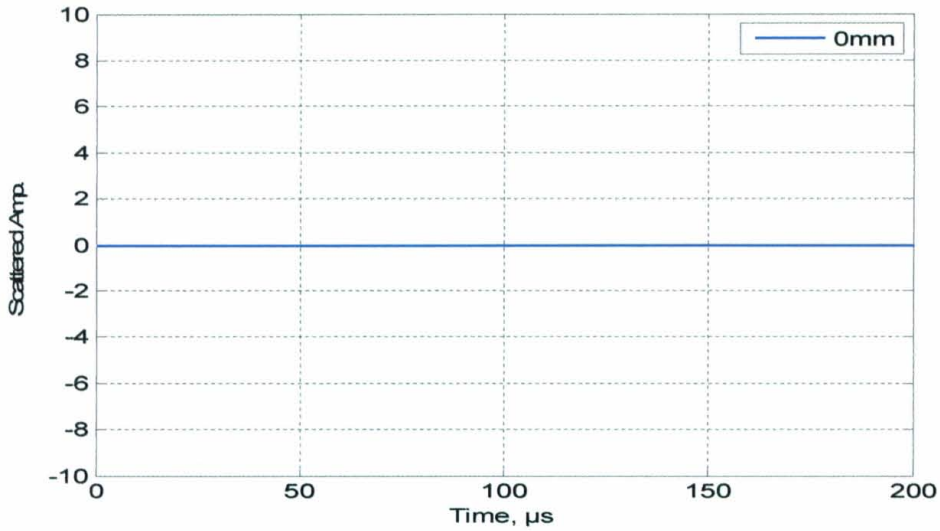

Figure 4.18 – Scattering Waves Time Domain Response for a Flaw Having 0 mm Radius.

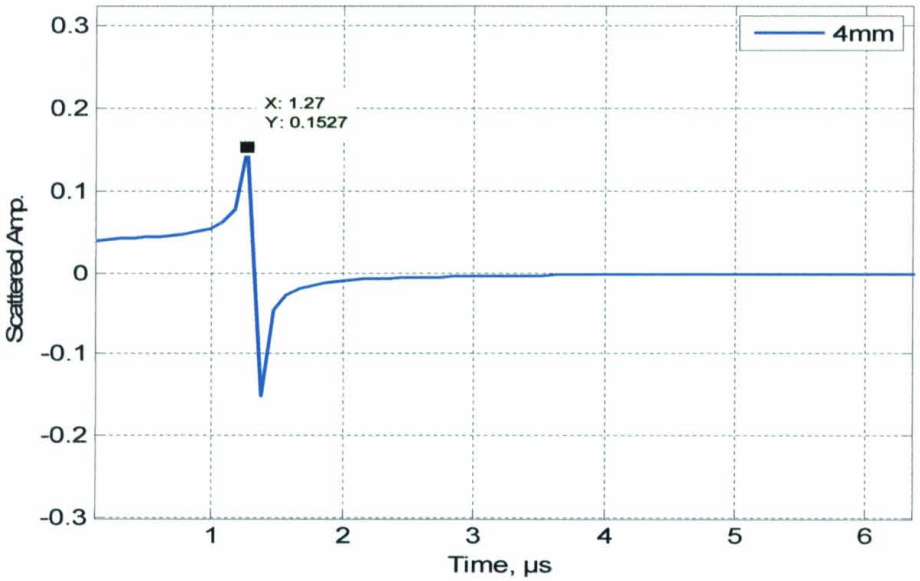

Figure 4.19 – Scattering Waves Time Domain Responses for Flaw Radius Size 4 mm.

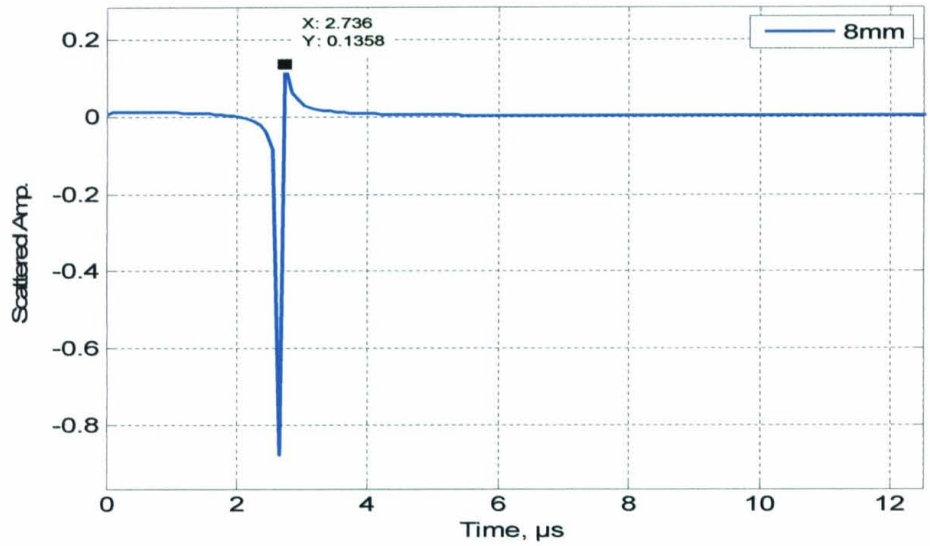

Figure 4.20 – Scattering Waves Time Domain Responses for Flaw Radius Size 8 mm.

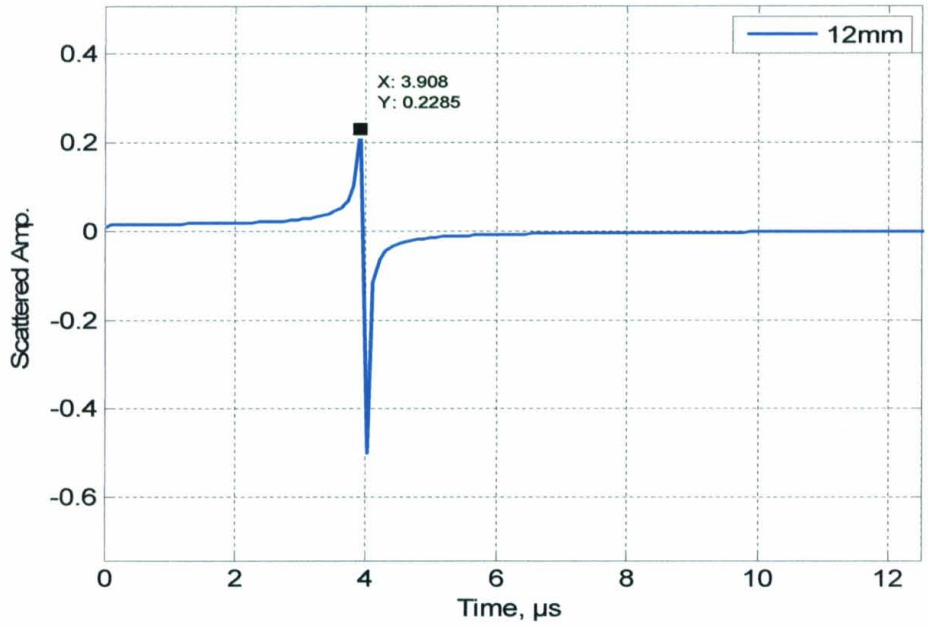

Figure 4.21– Scattering Waves Time Domain Responses for Flaw Radius Size 12 mm.

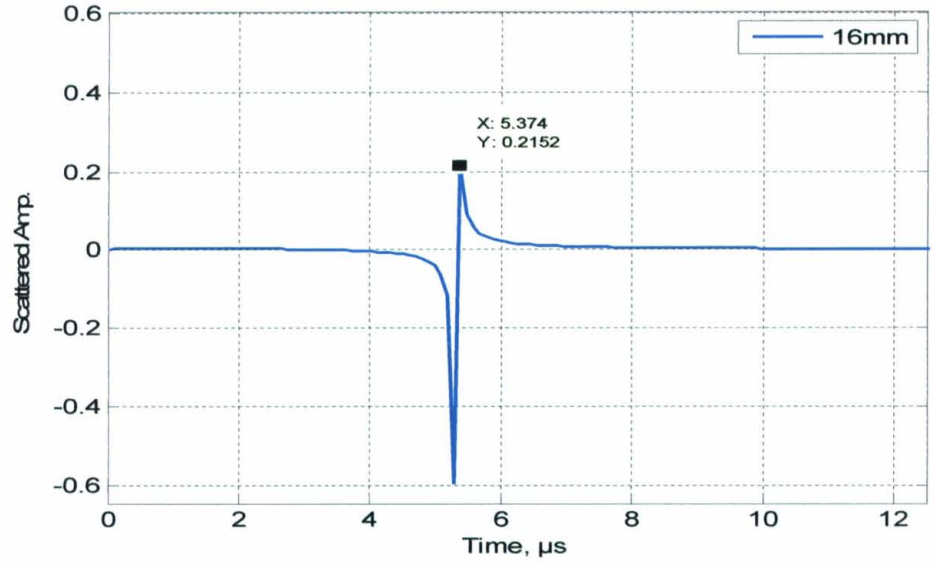

Figure 4.22 – Scattering Waves Time Domain Responses – Flaw Radius Size 16 mm.

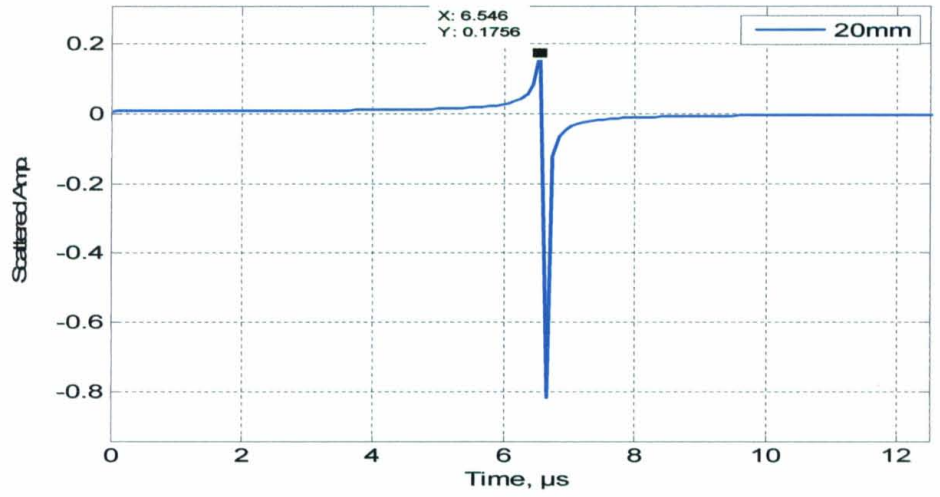

Figure 4.23 – Scattering Waves Time Domain Responses – Flaw Radius Size 20 mm.

4.5 SIGNAL PROPAGATION

The input signal can be presented as a sine wave which propagates in the structure. The signal is infinite, so a windowing technique is required to truncate the signal.

As mentioned earlier, there are several windowing techniques such as rectangular, Bartlett, Hanning, Hamming, Blackman and Kaiser. For this research Hanning windowing technique has been used. Other non-rectangular techniques can be used to produce smoother curves than the curves produced by the rectangular techniques. Smoother curves will definitely increase the accuracy when evaluating the spread of the signals and their amplitudes. The Hanning window function shown below truncates the signal where the sequences can be summed up (Oppenheim & Schafer, 2010):

$$W(n) = 0.5\left(1 - cos\left(\frac{2\pi n}{N}\right)\right), \quad 0 \leq n \leq N \tag{4.12}$$

Also, it can be expressed as (Lathi, 2005):

$$W(t) = 0.5\left[1 + cos\left(\frac{2\pi t}{T}\right)\right] \tag{4.13}$$

The input signal will be presented as a sine wave signal:

$$X(t) = 0.5 \times Cos\left(2\pi fc\,(t - td)\right) \tag{4.14}$$

Where,

f_c : Center frequency

t : Time vector; $0 \leq t \leq T$;

t is taken in steps of $t = \frac{T}{N-1}$

t_d : Time Delay

N : Number of samples

T : Time Duration for the signal in seconds

n : Index number

Then the truncated signal will be expressed as:

$$X_w(t) = X(t)W(t) \tag{4.15}$$

It is extremely crucial to know the frequency content of the signal to further analyze the signal. Performing the Fourier transform, the frequency domain representation of the signal is obtained.

$$X_w(t) \underset{\text{IFFT}}{\overset{\text{FFT}}{\rightleftharpoons}} X_w(\omega) \tag{4.16}$$

The signal propagating without defect in the frequency domain can be expressed as:

$$Y(\omega) = X_w(\omega)\exp(-jkd) \tag{4.17}$$

Where, d is the propagation distance and k is the wave number relating the frequency to the wave speed along the propagation path.

$$k = \frac{2\pi f}{C} \tag{4.18}$$

Multiplying it with the spreading coefficient of the defect, the signal propagation with defect in the frequency domain is obtained which can be expressed as:

$$Y(\omega) = X_w(\omega) exp(-jkd)\ \mathcal{A}_{sf} \tag{4.19}$$

This is the mathematical model that that will be used in this research to locate and estimate the defect. Then the output signal is presented in time domain by taking the Inverse Fourier Transform (IFFT). Obtaining the response in time domain will provide a better representation and understanding of the response, hence the flaw can be located. Knowing the group speed at the central frequency of the input signal and multiplying it with the propagation time, the location of the flaw or the length of the pipe can be estimated.

The steps required for carrying out the simulation process are:

1. Determine the input signal Equation (4.14), number of cycles and the central frequency (f_0).

2. Determine the length of the time window (T) for the input signal in (microseconds) and determine the number of Discrete Fourier Transform (DFT) points (N) for this time window.
3. Select a sampling frequency f_s greater than twice the signal bandwidth $f_s > 2BW$ to avoid overlapping repletion of the signal and to preserve the information of the input signal $x(t)$. The sampling frequency f_s is equal to $1/t_s$, sampling time or sampling intervals, $t_s = T/(N-1)$, then the time window will be divided into N sampling intervals.
4. Obtain the dispersion curves (frequencies versus group speed) for the input signal at the specified mode, whether longitudinal, torsional or flexural.
5. Apply the windowing technique (Hanning) to shorten the signal.
6. Perform FFT to the input signal to get the frequency content of the signal.
7. Obtain the prorogation flaw-free signal (Equation 4.17, this is reference signal) and the propagation signal with flaw (4.19).
8. IFFT both signals in item 7.
9. Determine the width difference or the time shift between the two signals in step 8 and divide the result by two --- $f_e = 1/2(t_{flaw} - t_{ref})$, where f_e: flaw extent, t_{flaw} and t_{ref} are the time at the highest amplitude of the flaw signal and the time at the highest amplitude of reference signal respectively.
10. Multiply the time shift in step number 9 by the group speed obtained in step 4 at the specified central frequency to estimate the extent of the flaw in millimeters.
11. Add the time at the highest amplitude obtained for both signals in step 9 and multiply by the group speed and subtract that from the estimated flaw obtained in

10 to estimate the location of the flaw in meters, ---- $f_l = 1/2(t_{flaw} + t_{ref}) \times S_g - f_e$, where f_e is the flaw extent and S_g is the group speed.

Figures (4.24) and Figure (4.25) illustrate this fact in more details.

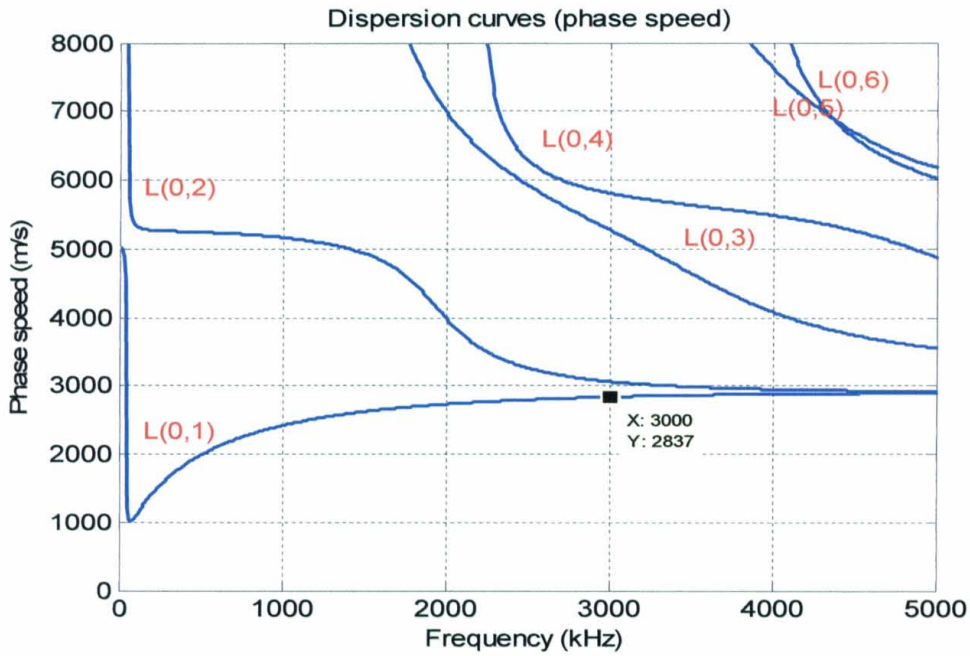

Figure 4.24– Dispersion Curves Showing the Phase Speed versus Frequency for Longitudinal Wave L(0,1).

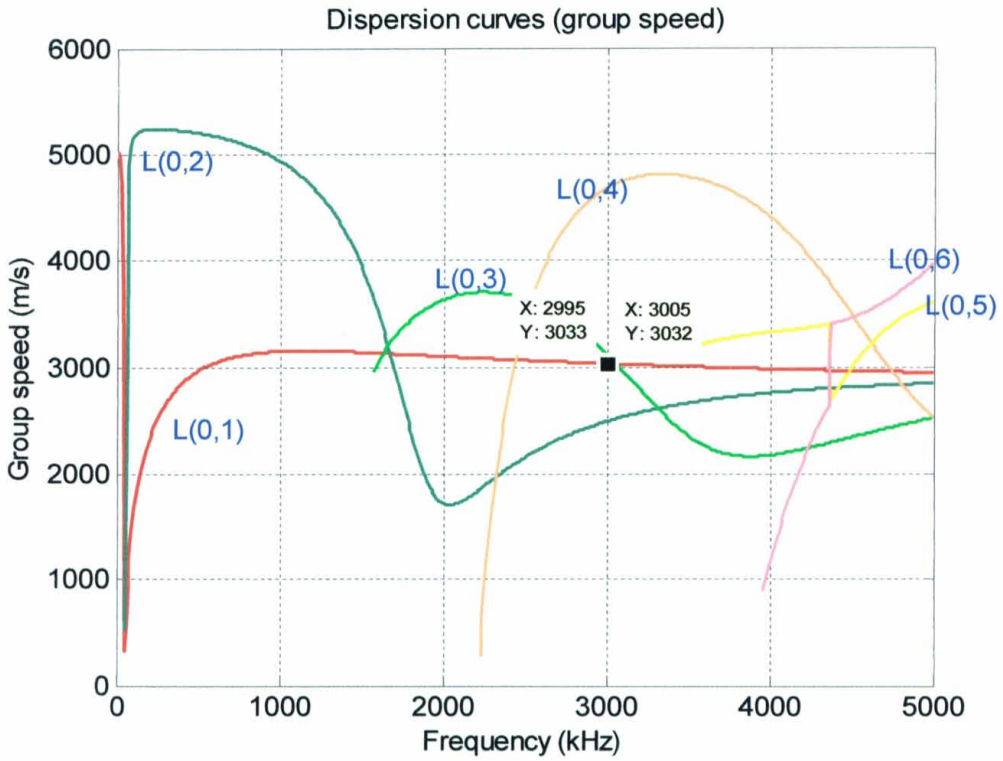

Figure 4.25 – Dispersion Curves Showing the Group Speed versus Frequency for Longitudinal Wave L(0,1).

Figure (4.25) depicts the dispersion curves for longitudinal wave propagating in steel pipe, mode(0,1), the group speed at the test frequency (300 kHz) is 3032.5 m/s for a 2-mtere steel pipe with an external radius of 16.468 mm and internal radius of 17.68 mm. Figure (4.25) is obtained by calculating the dispersion Equations (3.20) and (3.21) for longitudinal and torsional respectively. The propagating signal throughout the pipe is shown in Figure (4.26) in time domain.

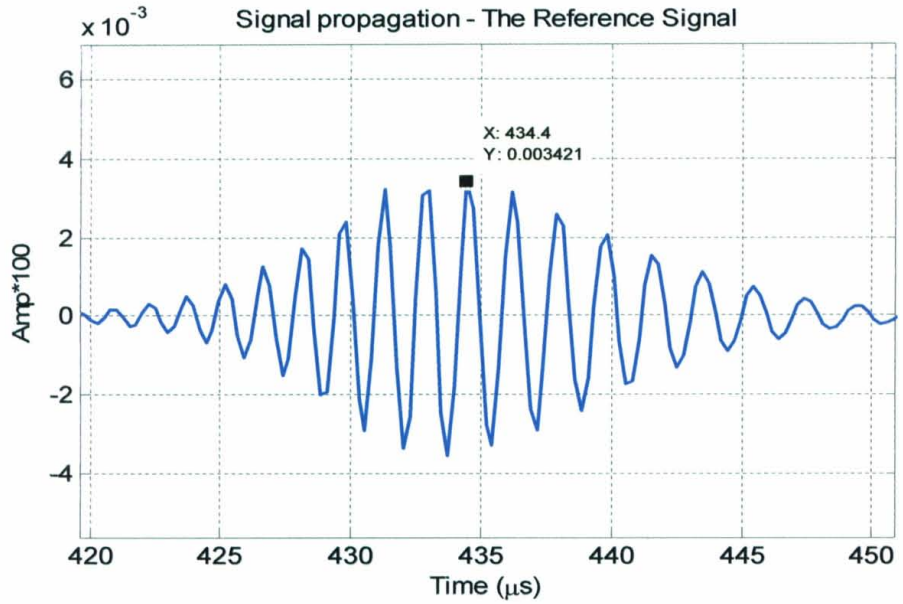

Figure 4.26 – The Reference Signal.

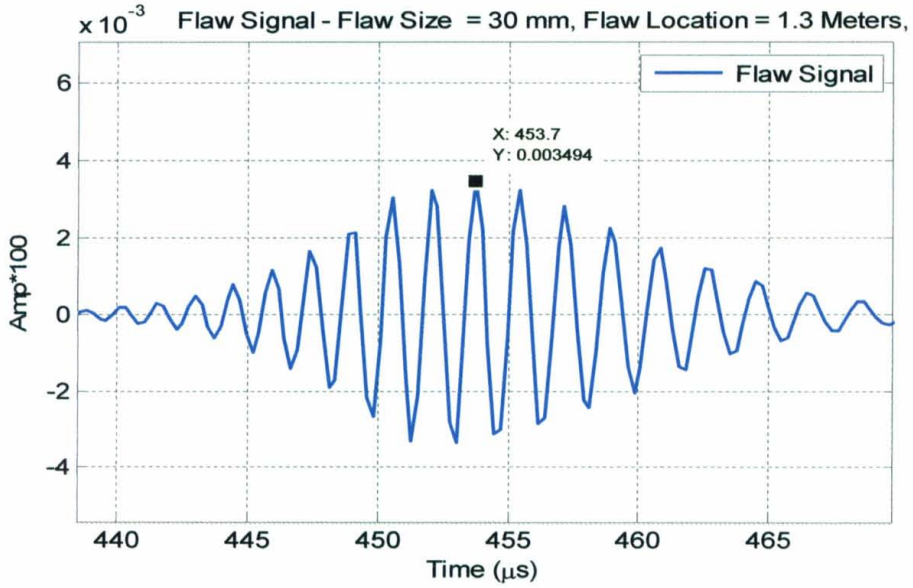

Figure 4.27 – The Flaw Signal.

As indicated in Figure (4.27) that the signal has travelled for 453.7 micro seconds while the reference signal shows the time at the highest amplitude is 434.4 micro seconds; obtaining the speed at the central frequency from Figure (4.25), that the speed is 3032.5 m/s.

The radius of the flaw can be approximated within an accepTable degree of accuracy by:

$$f_e = 1/2(t_{flaw} - t_{ref}) \times S_g$$

Where, f_e : flaw extent, t_{flaw} and t_{ref} are the time at the highest amplitude of the flaw signal and the time at the highest amplitude of reference signal respectively.

$f_e = 1/2 \times (453.7\ \mu s - 434.4\ \mu s) \times 3032.5\ m/s = 29.26\ mm.$

Percentage of Error = -2.45%.

Then the location of the flaw will be:

$f_l = 1/2(t_{flaw} + t_{ref}) \times S_g - f_e$, where f_e is the flaw extent and S_g is the group speed.

$f_l = 1/2 \times (453.7\ \mu s + 434.4\ \mu s) \times 3032.5 m/s - (29.26/1000)\ mm = 1.32$ meters.

To validate and demonstrate the feasibility of the mathematical models presented above, several trials with different propagation distances and flaw sizes are discussed in the next chapter, "Simulation and Results".

CHAPTER 5

SIMULATION AND RESULTS

One of the objectives of this research is to develop a mathematical model that can predict, locate and quantify the extent of spherical flaw. In this chapter several simulation trials for different flaw sizes at different locations on steel pipes will be presented using the mathematical model discussed in chapter 4. Such model can be used as a baseline for operators to know in advance what the output signals look like for defect-free-and defective pipelines. Moreover, such model can serve as a prerequisite for experimental work to provide signal response information before conducting the experiments. It basically enhances our understanding and confidence of such models before performing any real time operation or experimental work.

The main focus then will be exclusively on the developed mathematical model and the associated Equations under this research, Equations (4.11) and (4.19) of the previous chapter as well as Equation (4.17). To validate these models and prove their feasibility in the application area, several trials will be presented and investigated in section 5.1 to conclude their viability. Simulation of different flaw sizes located at fixed distance will be presented in section 5.2 while simulation of different flaw sizes located at various distances will be discussed in section 5.3. The objective of this analysis is to determine the accuracy of estimates obtained using the method suggested in this thesis.

5.1 CASE STUDIES SIMULATION

Steel pipes with the following input parameters having different lengths, different flaw sizes and different flaw locations will be considered in this study. Three different scenarios will be considered in the simulation to demonstrate the validity and applicability of the models.

5.1.1 Input Parameters

Pipe Parameters

Pipe Type:	*Steel Pipe*
Internal Diameter:	*18mm*
External Diameter:	*24mm*
Density:	*7800 kg/m^3*
Poisson's Ratio:	*0.3*
First Pipe	
Length:	*1.2M*
Flaw Location:	*0.3M*
Flaw Radius:	*20mm*
Second Pipe	
Length:	*2.0M*
Flaw Location:	*1.2M*
Flaw Radius:	*30mm*
Third Pipe	
Length:	*2.8M*
First Flaw location:	*0.8M*
First Flaw Radius:	*60mm*
Second Flaw location:	*1.4M*
Second Flaw Radius:	*80mm*

Input Signal Parameters

Test Frequency (Central Frequency - f_c):	*420 KHz*
Number of Samples:	*4096*
Signal Duration:	*2000e-6 Seconds*
Number of signal cycles:	*8 cycles*
Wave Type for the Test:	*Longitudinal Wave mode (0,1)*

The first step in the simulation process is to obtain the dispersion curves for the pipe being tested using Equation (3.20). From the dispersion curves, the phase or group speed can be determined at the specified input frequency used in the simulation. The value of the speed at the central frequency will be used to determine the propagation distance and the flaw size from the time domain response.

Figures (5.1) and (5.2) show the dispersion curves for the specified pipes mentioned above. The plot shows that the group speed at the central frequency (420 KHz) is 3080 m/s.

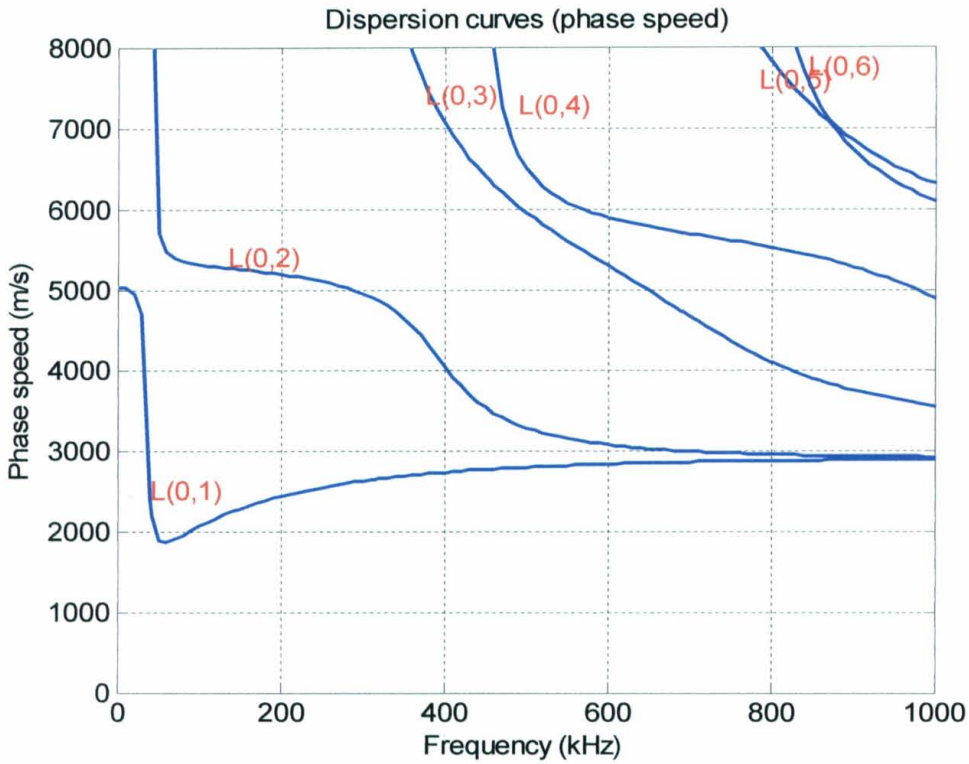

Figure – 5.1 - Dispersion Curves Showing Frequency versus Phase Speed for Longitudinal Mode.

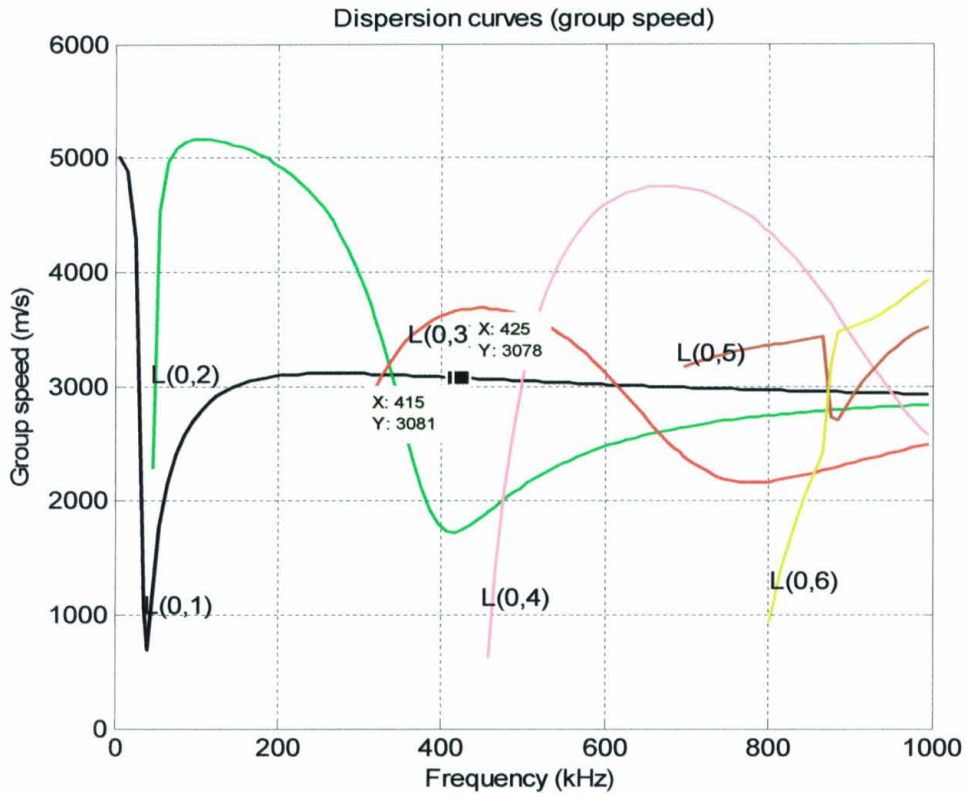

Figure – 5.2 - Dispersion Curves Showing Frequency versus Group Speed for Longitudinal Mode.

5.1.2 Simulation Results and Analysis

5.1.2.1 1.2 Meter Steel Pipe, Flaw Size 20mm Located At 0.9M

Figures (5.4) to (5.9) show the time domain response for 1.2 meter steel pipe with an internal diameter of 18mm and external diameter of 24 mm with a defect having a radius of 20mm located at a distance of 0.3M.

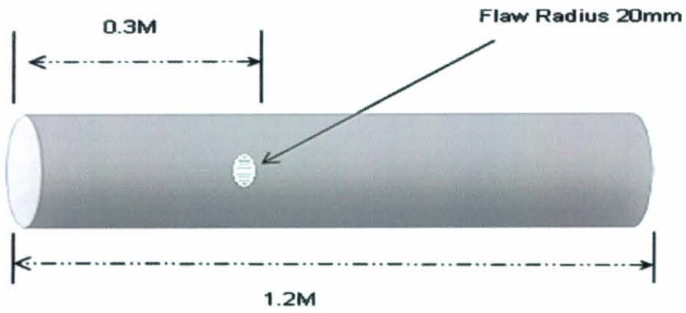

Figure 5.3 – Pipe Details for the First Simulation.

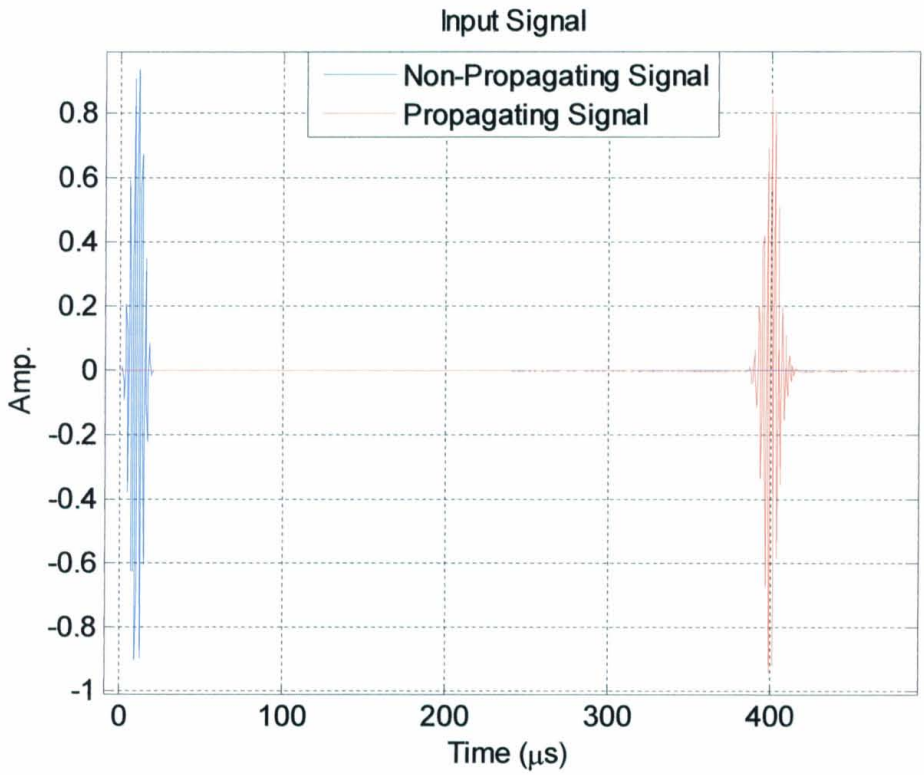

Figure 5.4 – The Original Signal and the Propagating Signal at the End of the Pipe.

Figure (5.4) shows the two signals in the same plot; the input signal and the propagating signal. The second signal travelled up to the end of a defect-free pipe, i.e., representing a pipe without a flaw.

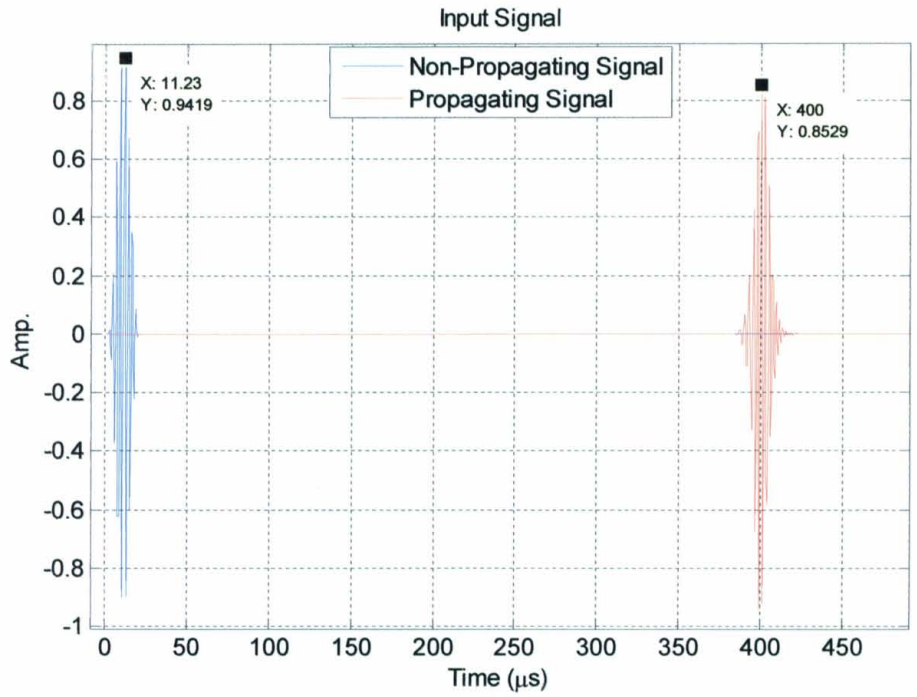

Figure 5.5 – The Original and the Propagating Signals Plot with Data Shown.

Figure (5.5) shows the time at the highest amplitude for both signals shown in the previous Figure, Figure (5.4). Figure (5.6) shows the original signal with a better representation.

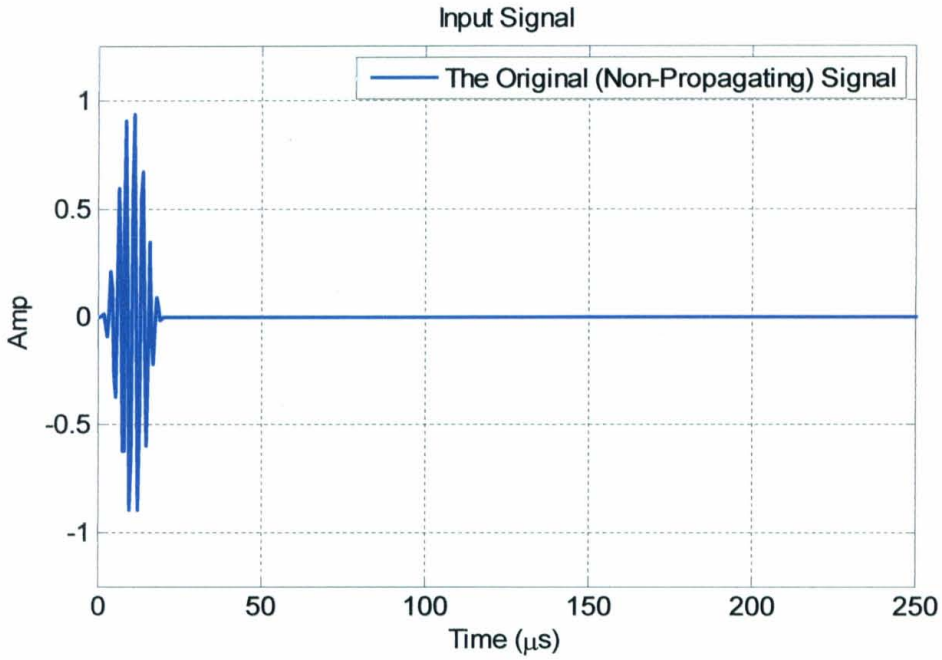

Figure 5.6 – The Original Signal.

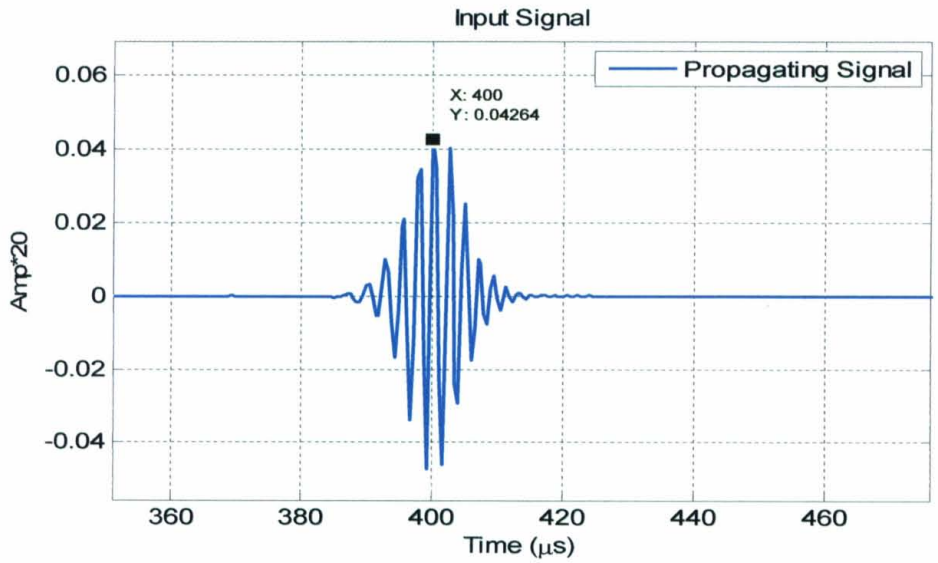

Figure 5.7 – The Propagating Signal up to the End of the Pipe.

Taking the time at the highest amplitude and multiplying it with the group speed at the specified input frequency, the travelled distance by the signal can be obtained. Figure (5.7) depicts the signal travelling in a defect-free pipe and it shows that the signal has travelled for 400 μs x 3080 m/s (group speed) = 1.23 meters; the actual distance is 1.2 meters; a small percentage error about 2.67% .

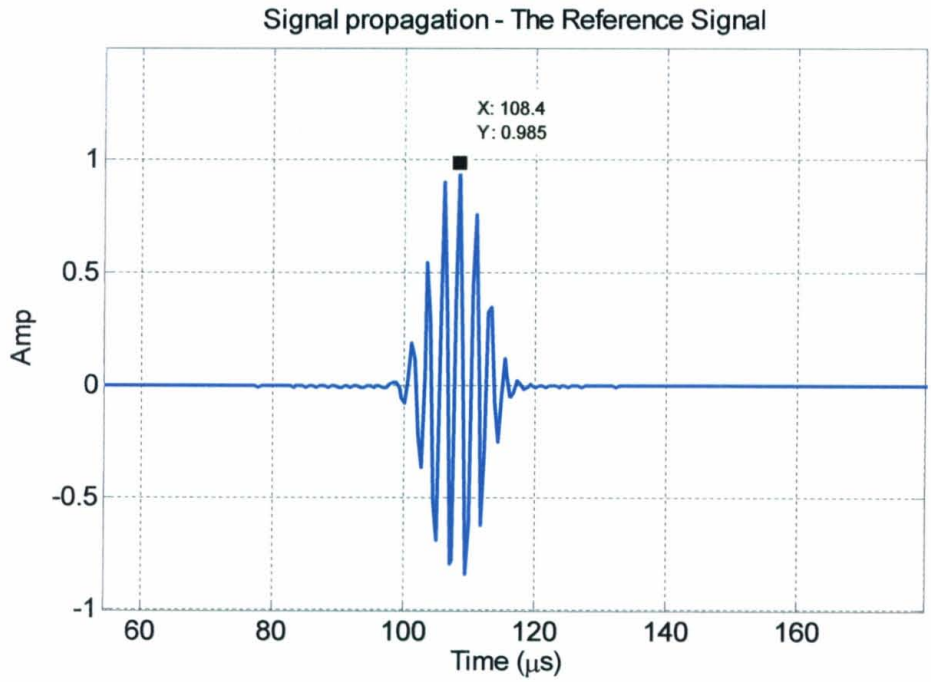

Figure 5.8 – The Flaw-Free Reference Signal.

Figure (5.8) illustrates the reference flaw-free signal that has travelled for 108.40 microseconds. The travelled distance by the propagating signal can be estimated by the following Equation:

$$\text{Travelled Distance} = t_{ha} \times S_g \tag{5.1}$$

Where, t_{ha} is the time at the highest amplitude of the propagating signal and S_g is the group speed.

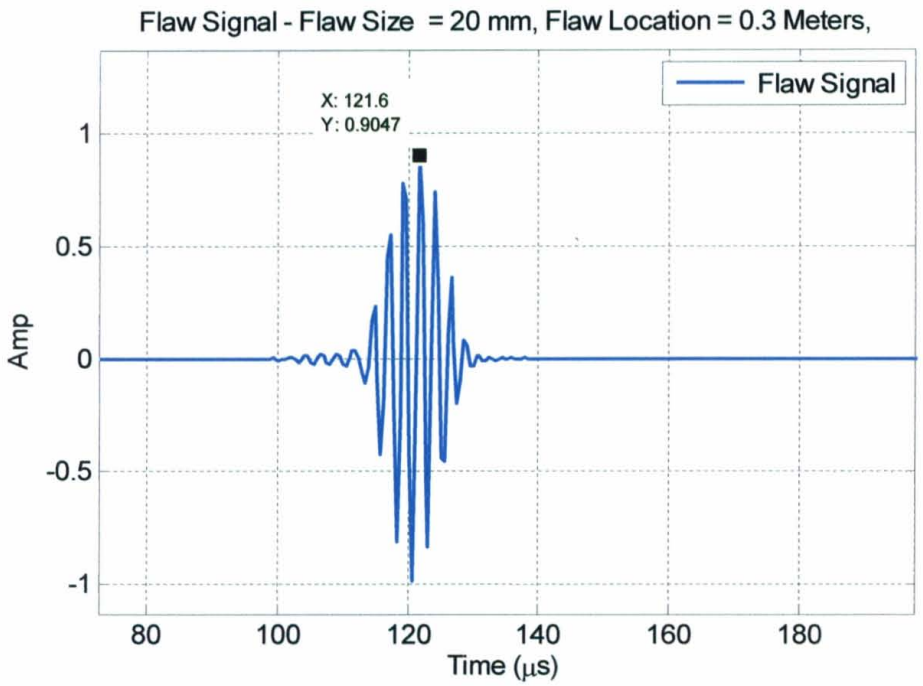

Figure 5.9 – The Flaw Signal.

Figure (5.9) shows the flaw signal has travelled for 121.60 microseconds. The extent of the flaw can be estimated by taking half of the difference of the times at the highest amplitudes of both the reference and the flaw signals and multiplying that by the group speed (Kundu, 2004). Estimated Flaw Extent:

$$f_e = \frac{1}{2}\left(t_{flaw} - t_{ref}\right) \times S_g \qquad (5.2)$$

Where, f_e is the flaw extent, t_{flaw} is the time at the highest amplitude of the flaw signal, t_{ref} is the time at the highest amplitude of the reference signal and S_g is the group speed of the signal.

The difference between the spread of the flaw signal and the reference signal is (121.6-108.4) /2 = 6.6 μs; 6.6 μs x 3080 m/s = 20.33 mm; the actual flaw radius is 20 mm; = 1.64% error.

The location of the flaw can be estimated by the following Equation:

$$\text{Estimated Flaw Location} = f_l = \frac{1}{2}\left(t_{flaw} + t_{ref}\right) \times S_g - f_e \qquad (5.3)$$

The location of the flaw = 0.5 × (121.6 + 108.4) x3080 – 20.33 /1000 = 0.33 meter; percentage of error =10%.

5.1.2.2 2.0 Meter Steel Pipe, Flaw Size 30mm Located at 1.2M

Figures (5.11) to (5.15) show the time domain responses for 2 meter steel pipe with an internal diameter of 18mm and external diameter of 24 mm with a defect having a radius of 30mm located at a distance of 1.2 m.

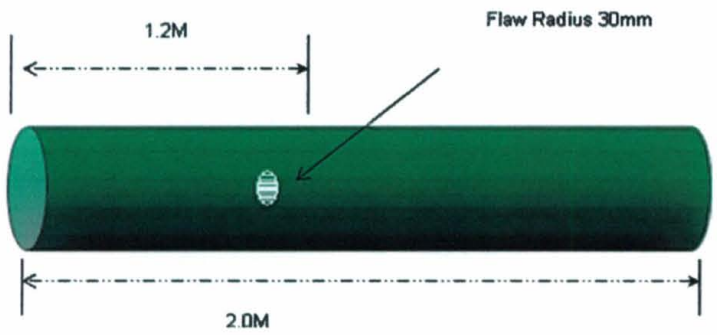

Figure 5.10 – Details of the Pipe – Second Simulation.

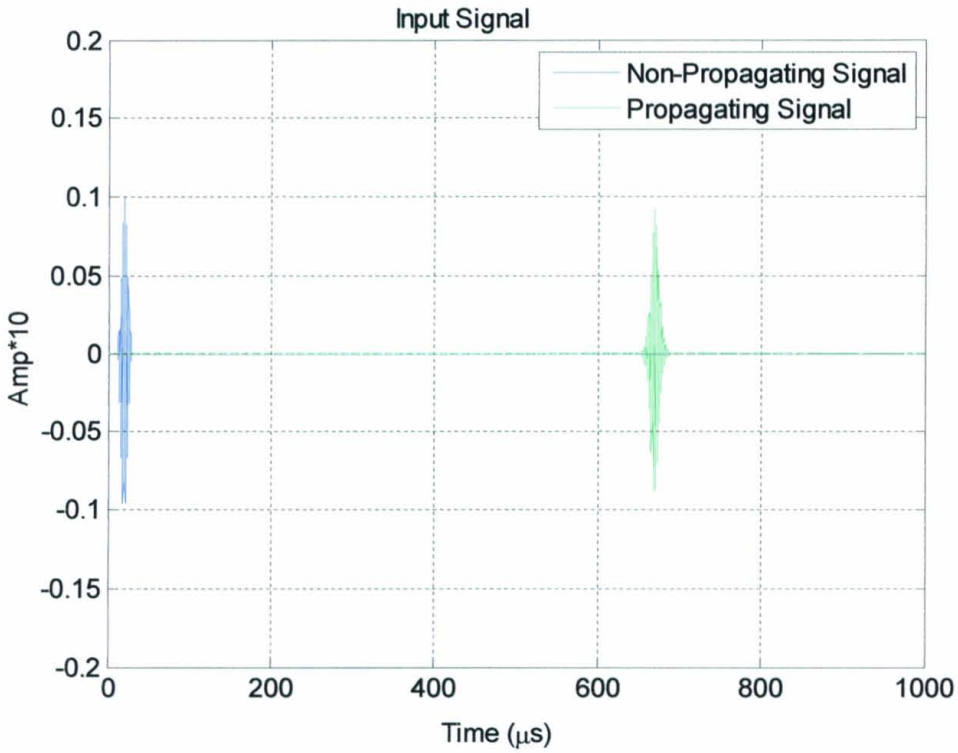

Figure 5.11 – The Original Signal and Propagating Signal.

Figure (5.11) shows two signals in the same plot; the input signal and the signal that has travelled to the end of the pipe. Figure (5.12) shows the input signal in better resolution.

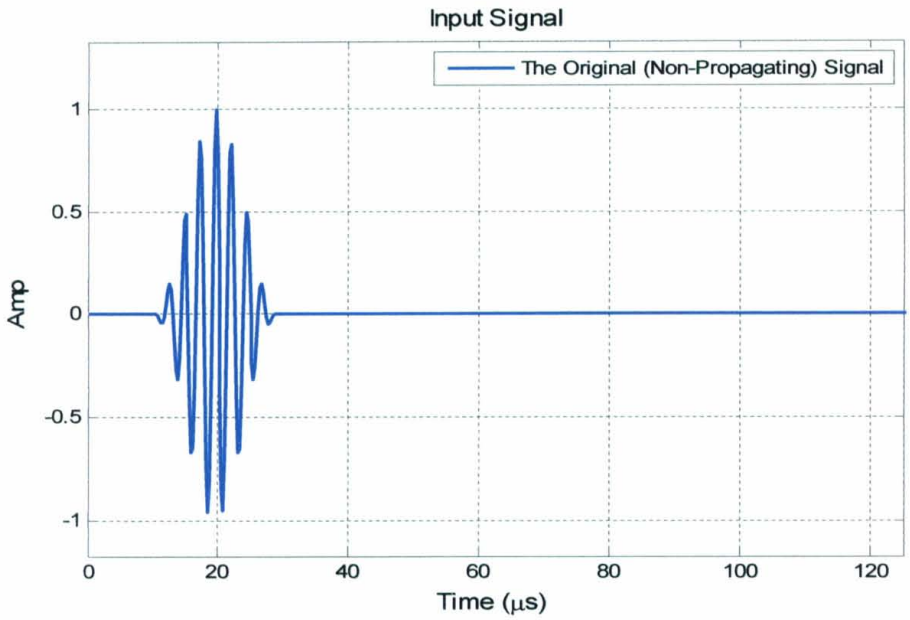

Figure 5.12 – The Original Signal.

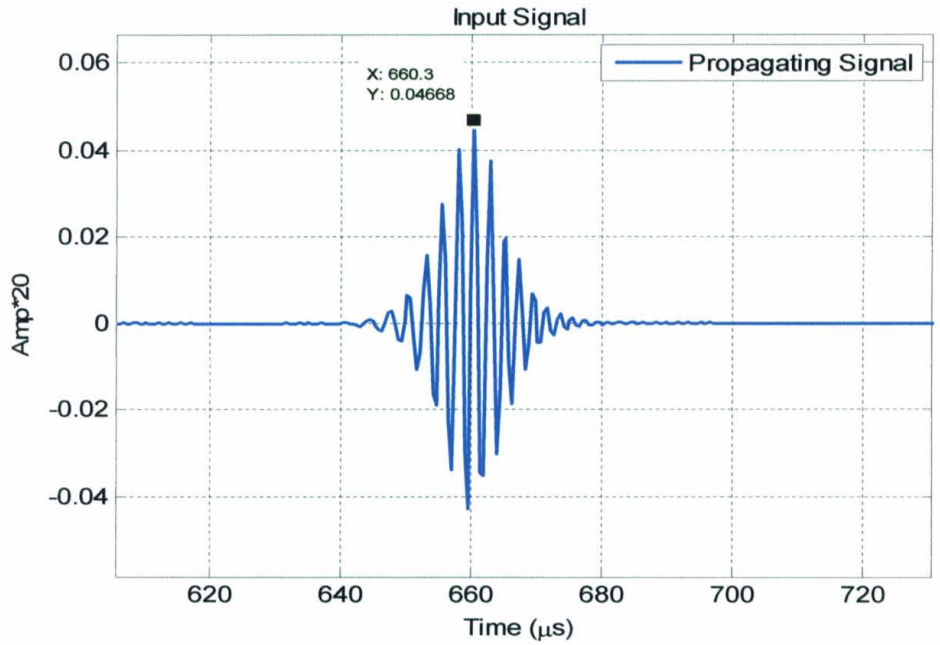

Figure 5.13 – The Propagating Signal.

Figure (5.13) portrays the signal that travelled to the end of the pipe stopping at 660.3 μs, which the time is taken at the highest amplitude. Measuring travelling distance: 660.3 μs × 3080 m/s = 2.03 meters; 98.3% accuracy.

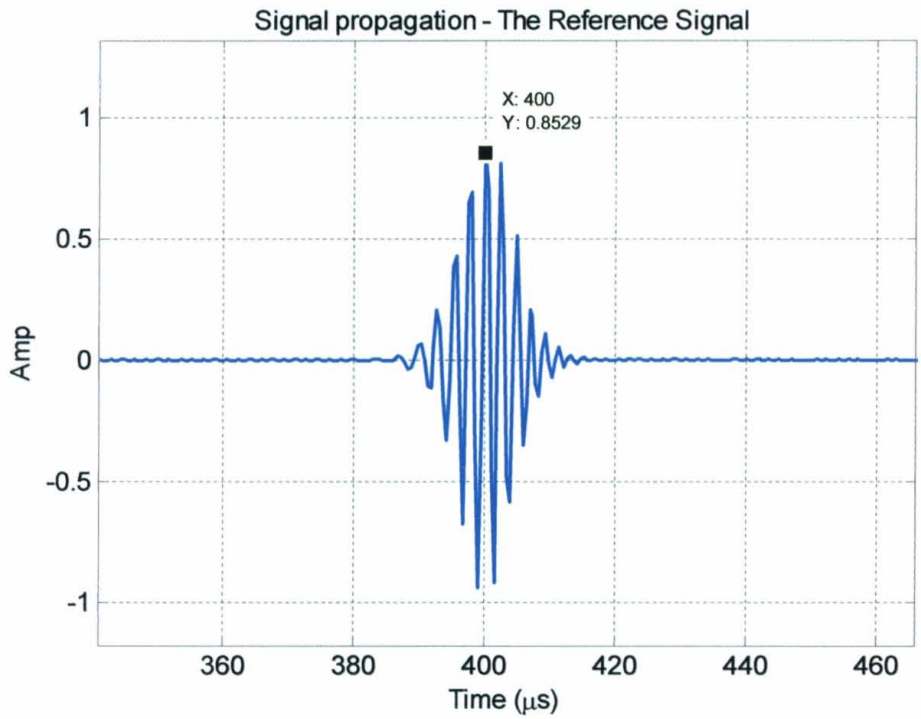

Figure 5.14– The Reference (Free-Defect) Signal

Figure (5.14) shows the reference flaw-free signal; time at the highest amplitude is 400 μs.

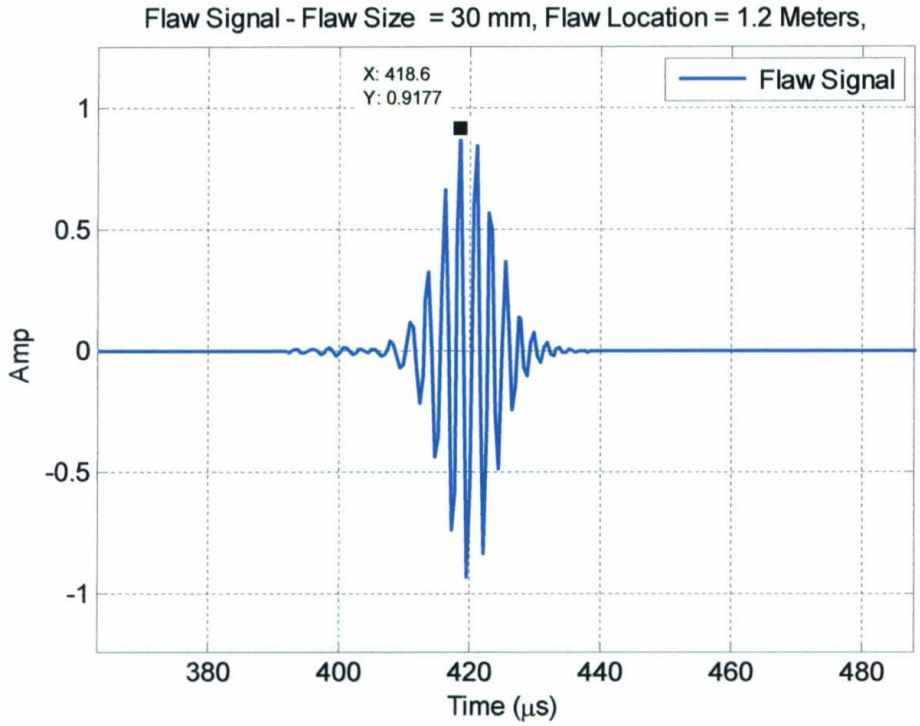

Figure 5.15 – The Flaw Signal.

Figure (5.15) illustrates the flaw signal, travelling for 418.60 μs; using Equation 5.2, to obtain the extent of the flaw = 1/2 x (418.60 – 400) μs × 3080 m/s = 29 mm; 3.33 % error.

Using Equation 5.3 to estimated the location of the flaw :

1/2 × (418.6 + 400) us × 3080 m/s - 29 mm/1000 = 1.23 meters;

2.50% error, accounting for 98% accuracy in the result which is extremely good estimate.

5.1.2.3 2.8 – Meter Steel Pipe, Flaw Sizes 60mm at 0.8M and 80mm at 1.4M

Figures (5.17) to (5.24) show the time domain responses for a 2.8-meter steel pipe with an internal diameter of 18mm and external diameter of 24 mm with two defects, the first one has a radius of 60mm, located at a distance of 0.8M, and the second defect has a radius of 80mm and located at 1.4M.

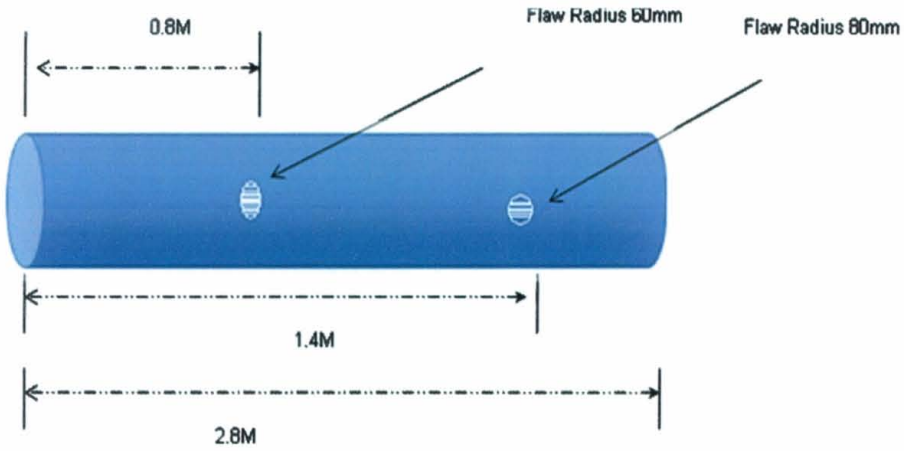

Figure 5.16 – Details of the Pipe – Third Simulation.

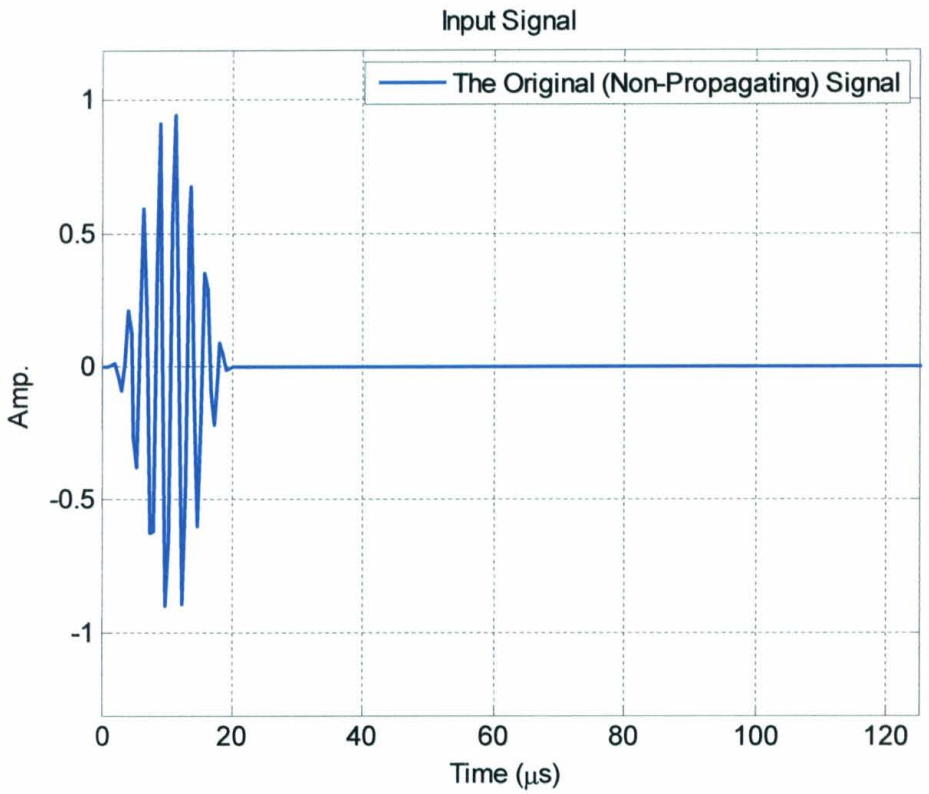

Figure 5.17 – The Input Signal.

Figure (5.17) depicts the input signal as a stationary signal not moving while Figure (5.18) shows the signal after it has travelled to the end of the pipe.

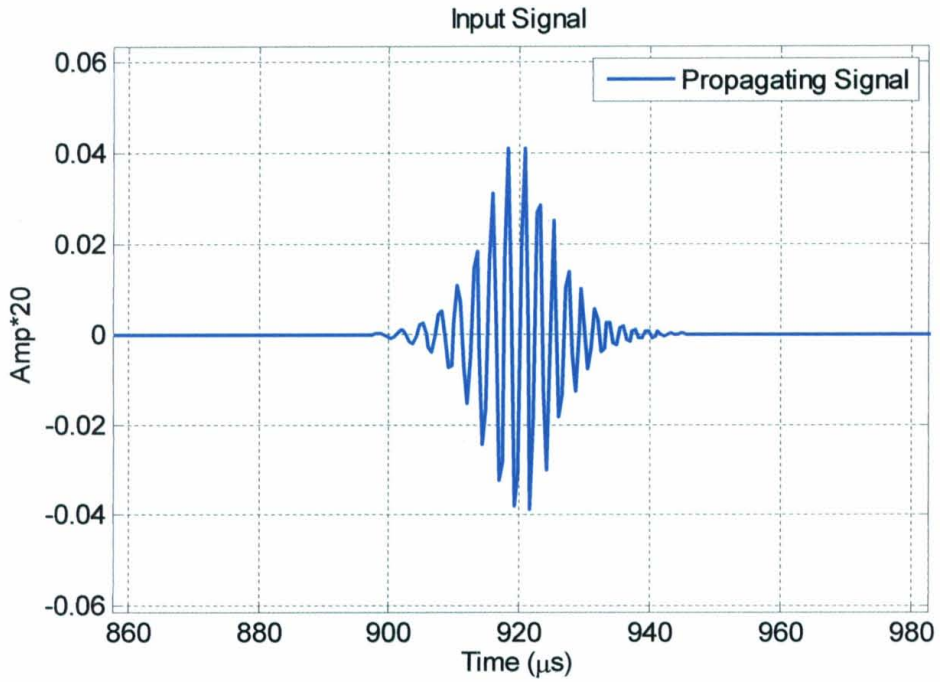

Figure 5.18 – The Response of the Propagating Signal.

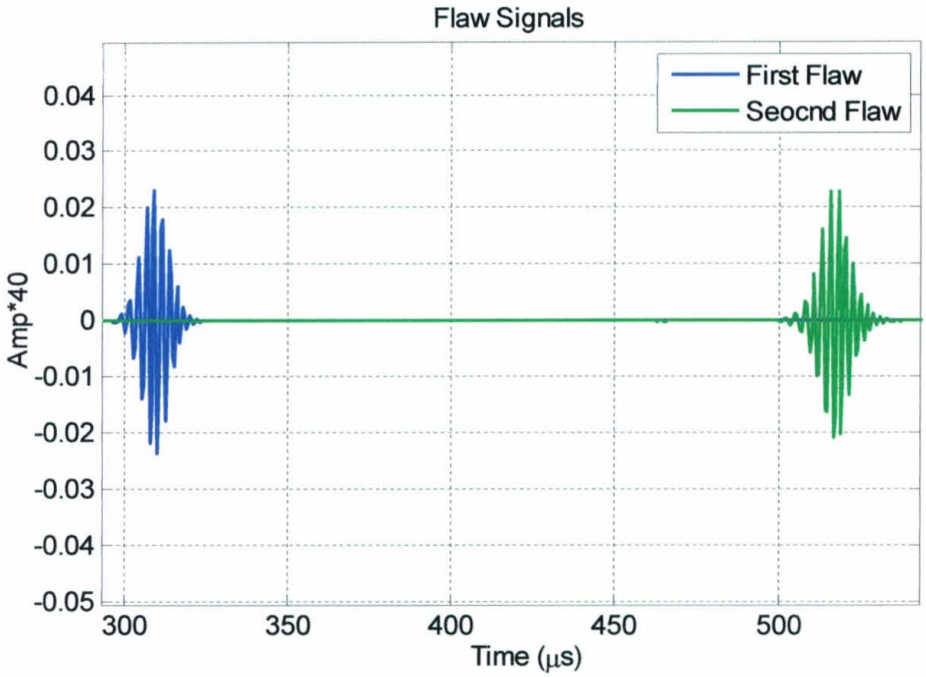

Figure 5.19 – The Response of the 1st and 2nd Flaw Signals.

Figure (5.19) illustrates the signals for the first and second flaws in two different colors. The Figure bleow, Figure (5.20) shows the propagating signal, travelleing for 918.2 μs; using eqaution (5.1) the estimated tarvelled distance becomes 2.828 meters, the actual distance is 2.8 meters, the reuslt has almost 99% accuracy.

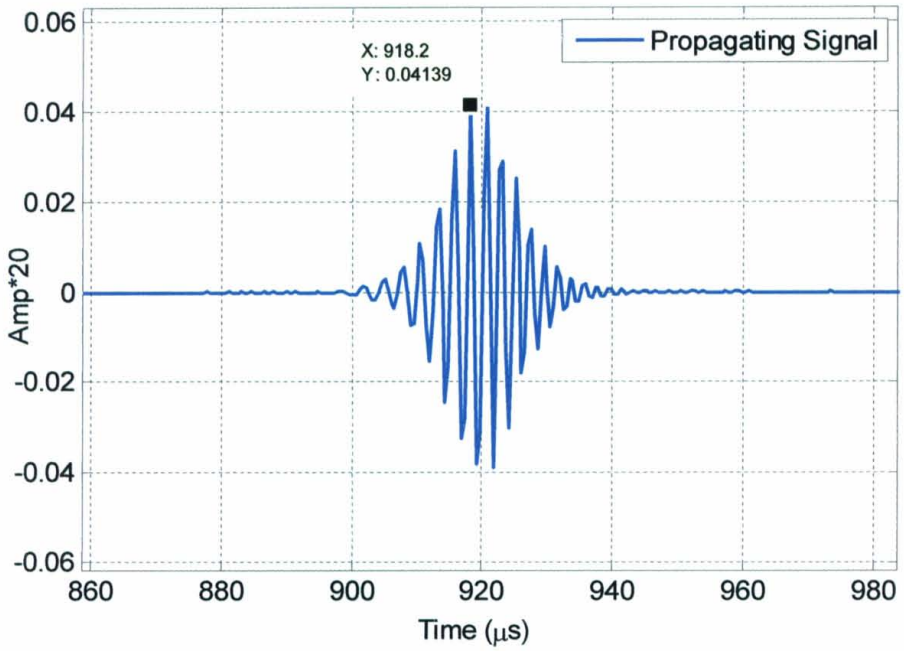

Figure 5.20 – The propagating Signal with Data Shown on the Plot.

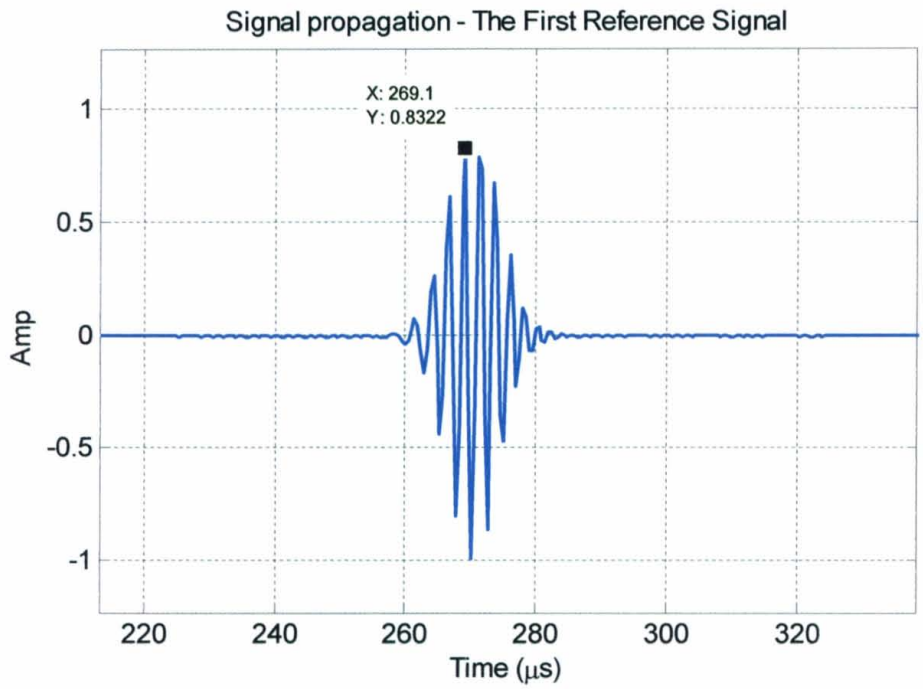

Figure 5.21 – The reference Signal for the 1st Flaw with Data Shown on the Plot.

Figure (5.21) shows the reference signal for the first flaw stopping at 269.1 μs.

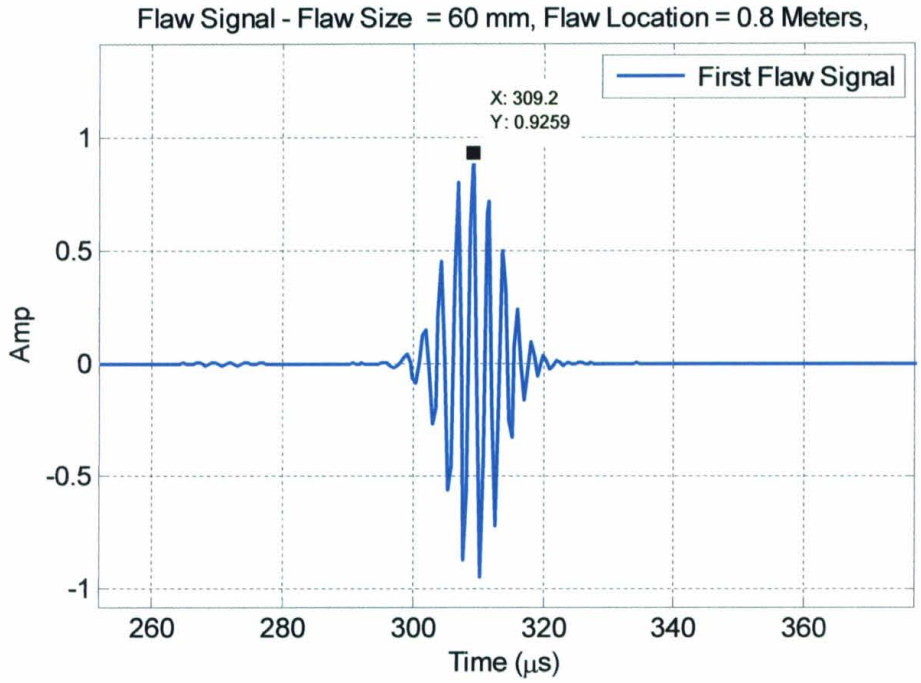

Figure 5.22 – The 1st Flaw Signal with Data Shown on the Plot.

Figure (5.22) shows the time at the highest amplitude for the first flaw signal at 309.2 μs, the estimated flaw size = 61.8 mm; the actual is 60 mm; 2.9% error. Using Equation (5.3) to get the estimated location of the flaw, the estimated location is 0.83 meters. The actual location is 0.8 meter, this difference in result accounts to 3.82% error in the result which is a negligible error.

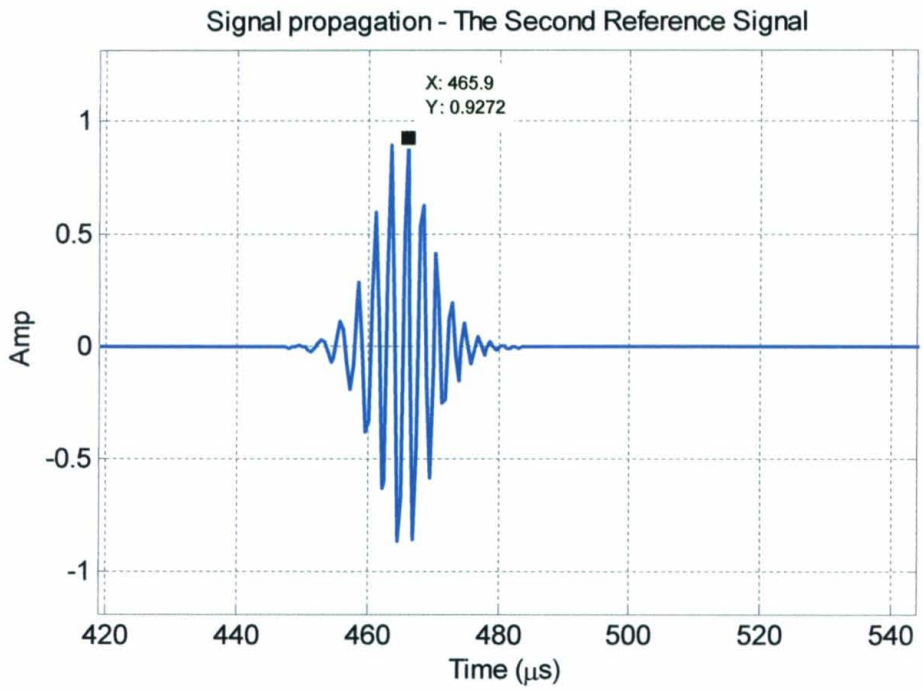

Figure 5.23 – The Reference Signal for the 2nd Flaw with Data Shown on the Plot.

The reference signal for the second flaw is shown in Figure 5.23 where the time at the highest amplitude is 465.9 μs.

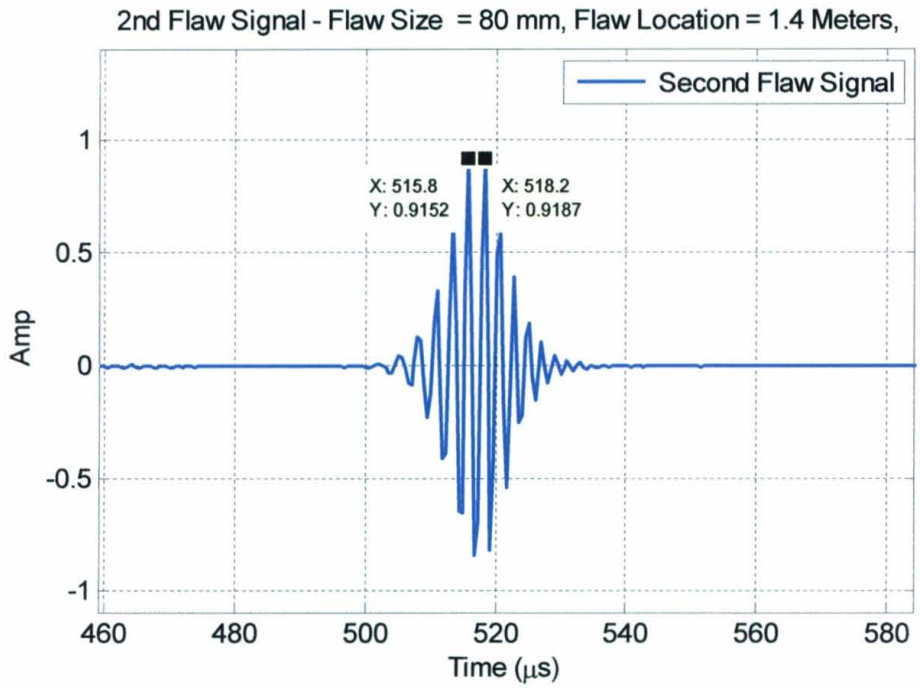

Figure 5.24 – The 2nd Flaw Signal with Data Shown on the Plot.

Figure (5.24) shows the plot for the second flaw; time at the highest amplitude 518.2 μs. The estimated flaw size 80.65 mm. the actual flaw size is 80 mm; the difference between the actual and the estimated accounts for 0.81% error which is extremely good. The estimated flaw location, using Equation (5.3) becomes 1.44 meters; accounting for 2.86 % error.

5.2 SIMULATION OF DIFFERENT FLAW SIZES LOCATED AT FIXED LOCATION

The model was tested for various flaw sizes located at 1.2 meter and 2.0 meter at low frequency, 300 KHz and high frequency 5MHz. The flaw sizes ranging from 10 mm up to 300 mm: 10, 20, 30, 40, 50, 60, 70, 80, 90, 100, 110, 120, 130, 140, 150, 160, 180, 200, 260 and 300 mm.

5.2.1 Simulation of Different Flaw Sizes at Low Frequency

5.2.1.1 Simulation of Different Flaw Sizes at Low Frequency Located at 1.2 m

The specified frequency is 300 KHz and the group speed at this frequency as shown in Figure (5.25) is 3116 m/s; Table (5.1) presents the relevant information for each estimated flaw size and the estimated flaw location followed by a plot portraying the actual versus estimated flaw sizes.

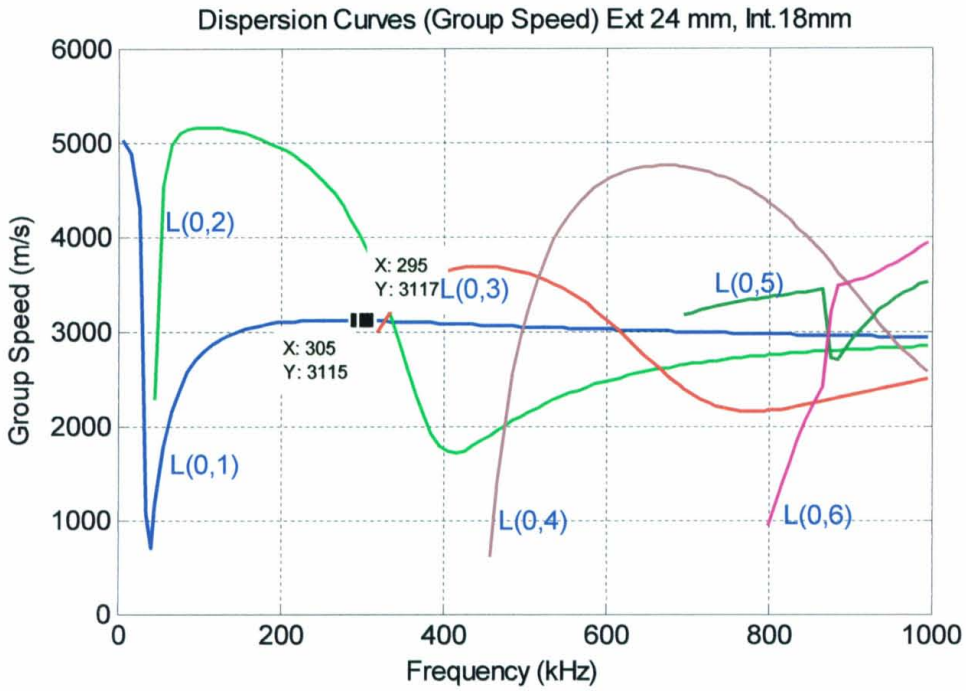

Figure – 5.25 – The Dispersion Curves – Group Speed – for Longitudinal Mode.

Actual Flaw Size (mm)	Actual Time Difference (μs)	Estimated Time Difference (μs)	Estimated Flaw Size (mm)	% of Error	Actual Flaw Location (m)	Estimated Flaw Location (m)	% of Error
10	3.21	3.18	9.89	1.05%	1.20	1.23	2.50%
20	6.42	6.84	21.31	-6.56%	1.20	1.23	2.50%
30	9.63	9.04	28.16	6.13%	1.20	1.23	2.50%
40	12.84	12.95	40.34	-0.85%	1.20	1.23	2.50%
50	16.05	16.61	51.76	-3.51%	1.20	1.23	2.50%
60	19.26	18.81	58.61	2.32%	1.20	1.23	2.50%
70	22.46	22.47	70.02	-0.03%	1.20	1.23	2.50%
80	25.67	26.38	82.20	-2.75%	1.20	1.23	2.50%
90	28.88	28.58	89.05	1.05%	1.20	1.23	2.50%
100	32.09	32.24	100.47	-0.47%	1.20	1.23	2.50%
110	35.30	36.15	112.64	-2.40%	1.20	1.23	2.50%
120	38.51	41.86	130.45	-8.71%	1.20	1.23	2.50%
130	41.72	42.01	130.91	-0.70%	1.20	1.23	2.50%
140	44.93	44.21	137.76	1.60%	1.20	1.23	2.50%
150	48.14	48.12	149.94	0.04%	1.20	1.23	2.50%
160	51.35	51.78	161.36	-0.85%	1.20	1.23	2.50%
180	57.77	57.65	179.62	0.21%	1.20	1.23	2.50%
200	64.18	63.75	198.65	0.67%	1.20	1.23	2.50%
260	83.44	83.29	259.54	0.18%	1.20	1.23	2.50%
300	96.28	96.73	301.40	-0.47%	1.20	1.23	2.50%

Table 5.1 - Output Results for Various Flaw Sizes at Low Frequency Located at 1.20 m.

The actual time difference is calculated by taking the actual flaw size and dividing it by the estimated group speed obtained from the dispersion curves. The estimated time

difference is calculated by subtracting the time at the highest amplitude for the flaw signal from that of the reference signal and dividing the result by 2.

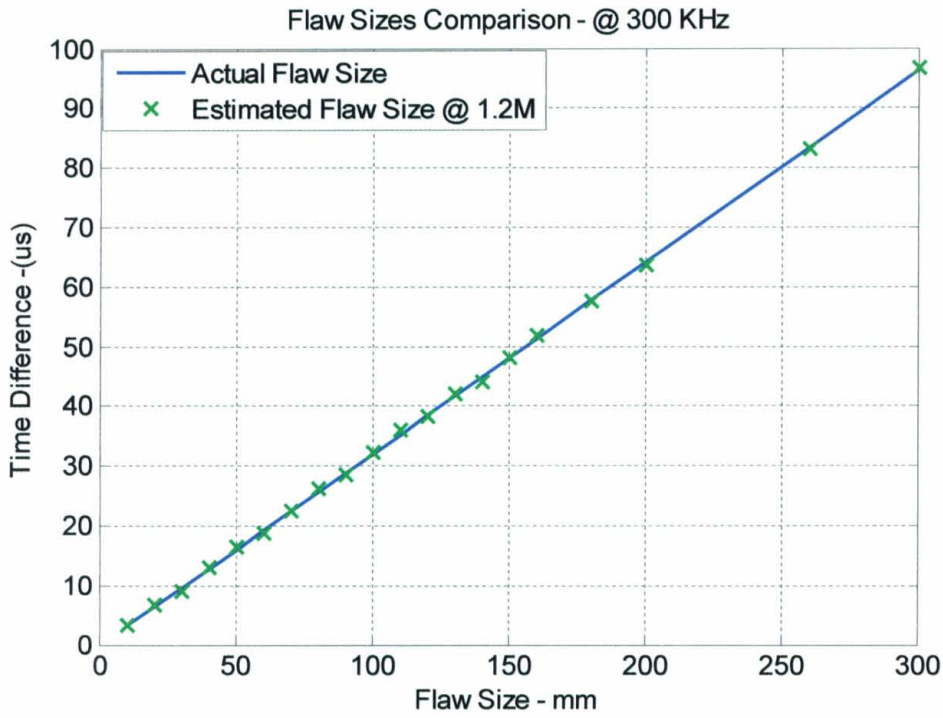

Figure 5.26 – Comparison between Actual and Estimated Flaw Sizes Located at 1.2 Meter - Central Frequency = 300 KHz.

Figure (5.26) compares the estimated flaw sizes versus the actual flaw size; the estimated values almost agree with actual values with a percentage of error ranging from -8.71% to 6.13% providing accuracy ranging from -91.3% to 94%.

5.2.1.2 Simulation of Different Flaw Sizes at Low Frequency Located at 2.0 m

The specified frequency is 300 KHz and the group speed at this frequency as shown in Figure (5.26) is 3116 m/s; Table (5.2) presents the relevant information for each estimated flaw size and the estimated flaw location followed by a plot portraying the actual versus estimated flaw sizes.

Actual Flaw Size (mm)	Actual Time Difference (μs)	Estimated Time Difference (μs)	Estimated Flaw Size (mm)	% of Error (±)	Actual Flaw Location (m)	Estimated Flaw Location (m)	% of Error (±)
10	3.21	3.05	9.51	-4.88%	2.0	2.03	1.66%
20	6.42	6.84	21.31	6.53%	2.0	2.03	1.66%
30	9.63	8.91	27.77	-7.42%	2.0	2.03	1.66%
40	12.84	12.82	39.95	-0.13%	2.0	2.03	1.66%
50	16.05	14.90	46.42	-7.17%	2.0	2.03	1.66%
60	19.26	18.68	58.21	-2.98%	2.0	2.03	1.66%
70	22.46	22.47	70.01	0.01%	2.0	2.03	1.66%
80	25.67	24.66	76.85	-3.93%	2.0	2.03	1.66%
90	28.88	28.45	88.65	-1.50%	2.0	2.03	1.66%
100	32.09	32.23	100.44	0.44%	2.0	2.03	1.66%
110	35.30	34.43	107.29	-2.46%	2.0	2.03	1.66%
120	38.51	38.22	119.09	-0.76%	2.0	2.03	1.66%
130	41.72	42.00	130.88	0.68%	2.0	2.03	1.66%
140	44.93	44.20	137.73	-1.62%	2.0	2.03	1.66%
150	48.14	47.99	149.52	-0.32%	2.0	2.03	1.66%
160	51.35	51.77	161.32	0.82%	2.0	2.03	1.66%
180	57.77	57.63	179.58	-0.23%	2.0	2.03	1.66%
200	64.18	63.61	198.22	-0.89%	2.0	2.03	1.66%
260	83.44	83.15	259.10	-0.35%	2.0	2.03	1.66%
300	96.28	96.70	301.33	0.44%	2.0	2.03	1.66%

Table 5.2 - Output Results for Various Flaw Sizes at Low Frequency Located at 2.0 m.

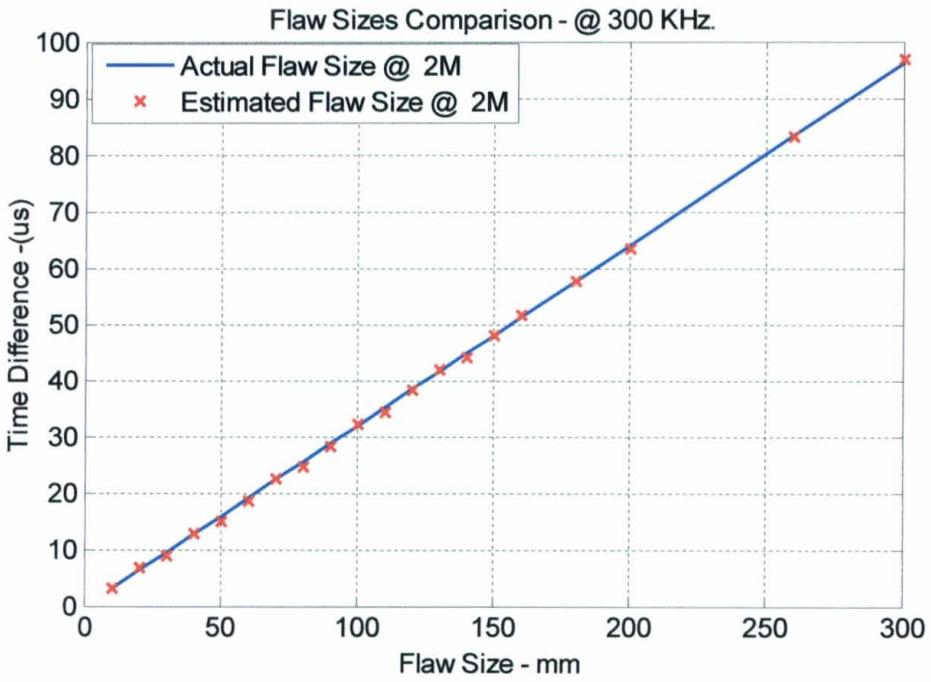

Figure 5.27 – Comparison between Actual and Estimated Flaw Sizes Located at 2.0 Meter - Central Frequency = 300 KHz.

Figure (5.27) compares the estimated flaw sizes versus the actual flaw size; the estimated values almost agree with actual values with a percentage of error ranging from -7.42% to 6.53% providing accuracy ranging from -92.6% to 93.5%.

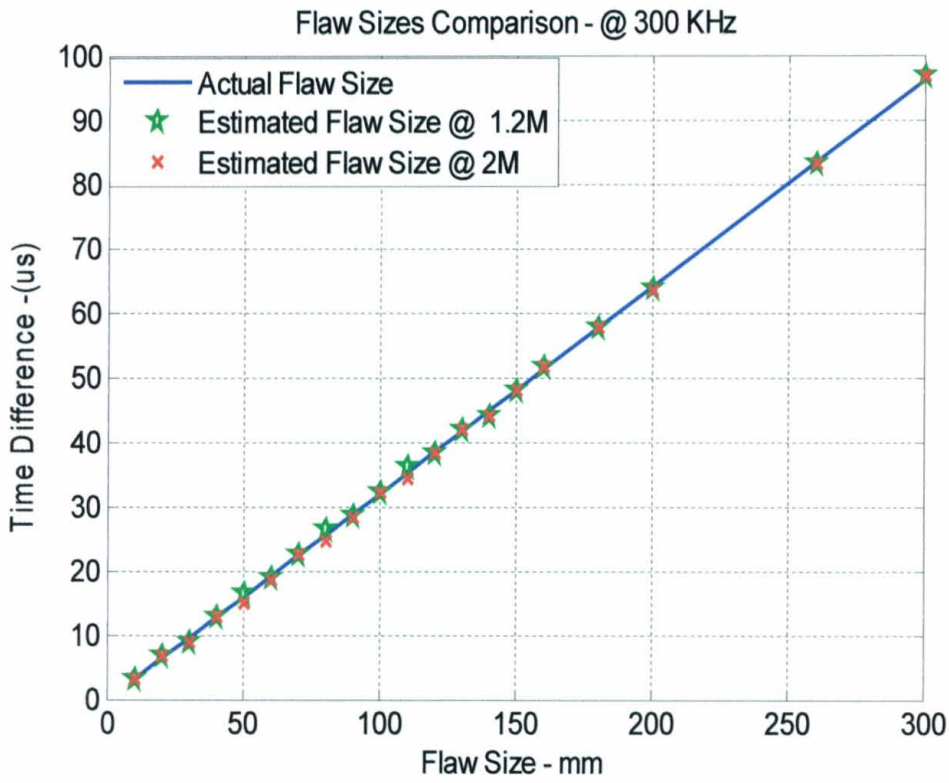

Figure 5.28 – Comparison between Actual and Estimated Flaw Sizes Located at 1.2 Meters and 2.0 Meters - Central Frequency = 300 KHz.

Figure (5.28) illustrates actual flaw sizes versus flaw sizes estimated at the low frequency, 300 KHz located at two different distances 1.2 meters and 2.0 meters. The estimated values fit exactly on the actual values line for both distances.

5.2.2 Simulation of Different Flaw Sizes at High Frequency Located at 1.2m and 2.0m

The model was tested for 30 mm flaw located at 1.2 meter and 2.0 meter at high frequency. The specified frequency was 5MHz. The group speed at 5MHz as shown in Figure (5.29) is 2905 m/s.

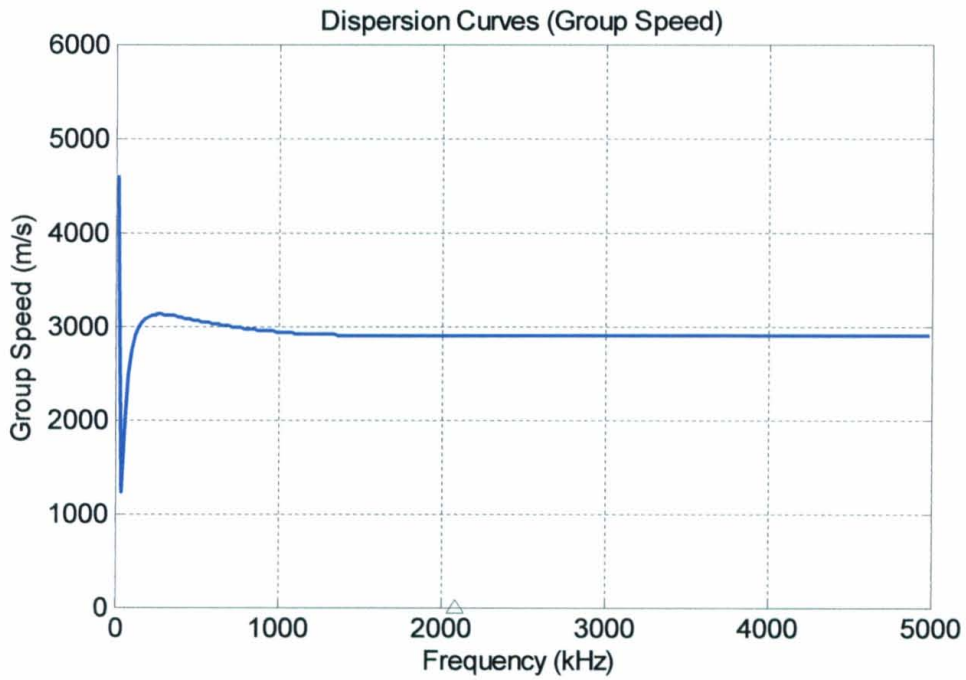

Figure 5.29 – Dispersion Curves – Group Speed – for Longitudinal Mode L(0,1).

5.2.2.1 Simulation of Different Flaw Sizes at High Frequency Located at 1.2M

Figures (5.30) and (5.31) show the plot for the first estimated flaw sizes, 30 mm is shown below. The time shift between both the reference and the flaw signal was calculated to be 9.6 μs, so the estimated flaw size is: 2905ms × 9.6 μs =28 mm, the percentage of error = 6.7%. Table (5.3) presents the relevant information for all the estimated flaw sizes considered and the estimated flaw location followed by a plot portraying the actual versus estimated flaw sizes.

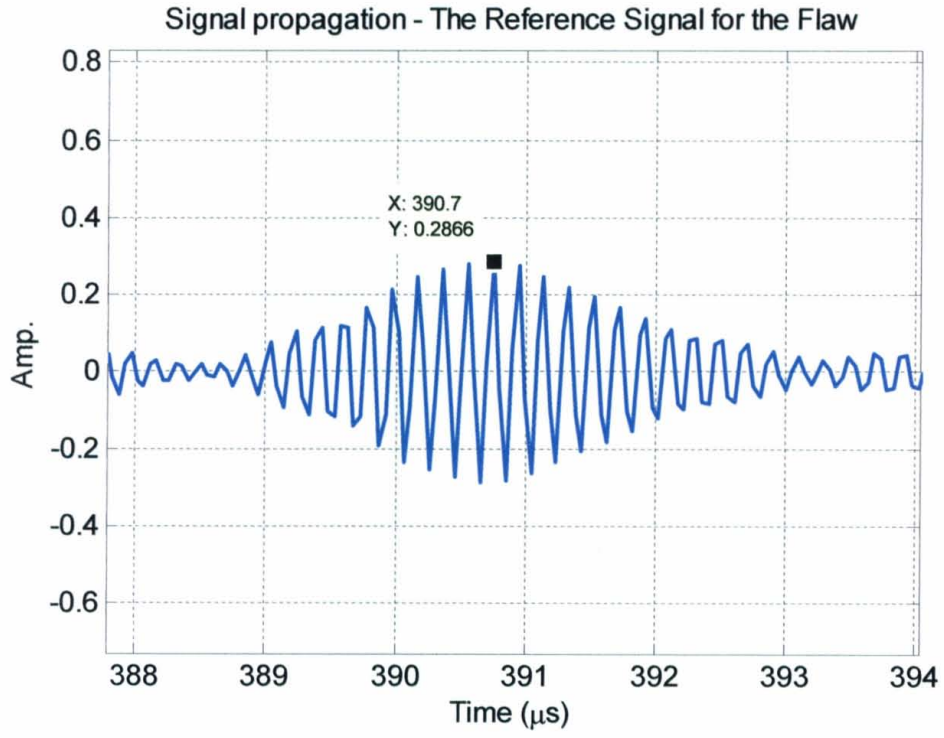

Figure 5.30 – Reference Signal for 30 mm Defect Located at 1.2 m – f_0 (High Frequency -5MHz).

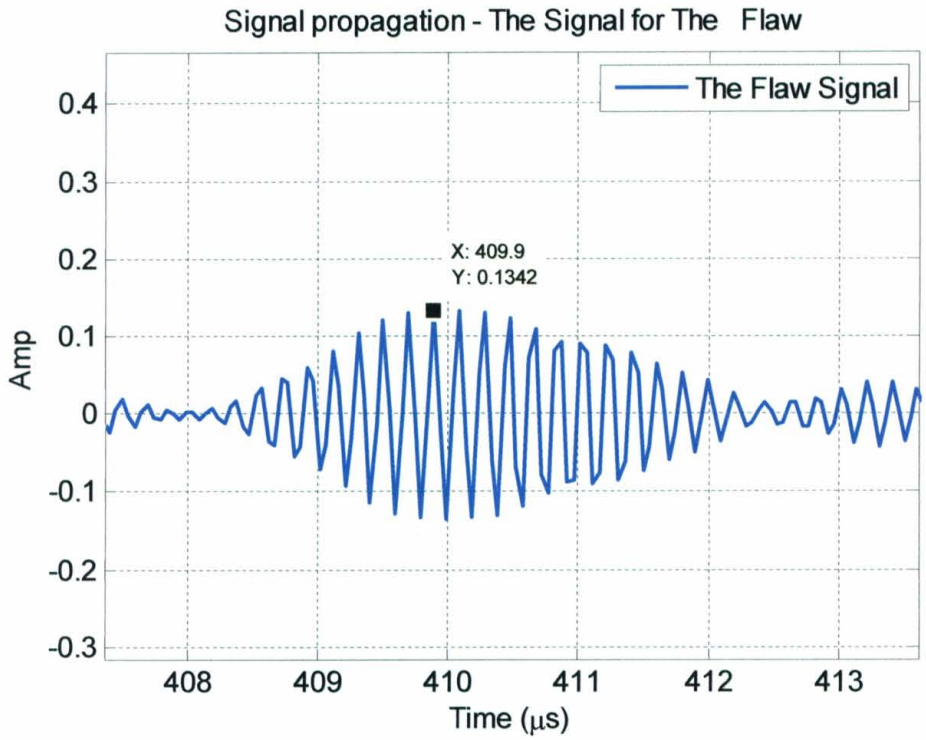

Figure 5.31 – Flaw signal for 30 mm defect located at 1.2 m – f_0 (High Frequency - 5MHz).

Flaw Size (mm)	Actual Time Difference (us)	Estimated Time Difference (us)	Estimated Flaw Size (mm)	% Error (±)	Flaw Location (m)	Estimated Flaw Location (m)	% Error (±)
10	3.44	3.05	8.86	-11.40%	1.20	1.13	-5.42%
20	6.88	6.65	19.32	-3.41%	1.20	1.13	-5.42%
25	8.61	8.30	24.11	-3.55%	1.20	1.13	-5.42%
30	10.33	9.60	27.89	-7.04%	1.20	1.13	-5.42%
40	13.77	13.10	38.06	-4.86%	1.20	1.13	-5.42%
50	17.21	16.15	46.92	-6.17%	1.20	1.13	-5.42%
60	20.65	19.30	56.07	-6.56%	1.20	1.13	-5.42%
70	24.10	22.85	66.38	-5.17%	1.20	1.13	-5.42%
80	27.54	25.80	74.95	-6.31%	1.20	1.13	-5.42%
90	30.98	29.40	85.41	-5.10%	1.20	1.13	-5.42%
100	34.42	32.45	94.27	-5.73%	1.20	1.13	-5.42%
110	37.87	35.50	103.13	-6.25%	1.20	1.13	-5.42%
120	41.31	39.00	113.30	-5.59%	1.20	1.13	-5.42%
130	44.75	42.05	122.16	-6.03%	1.20	1.13	-5.42%
140	48.19	45.70	132.76	-5.17%	1.20	1.13	-5.42%
150	51.64	48.55	141.04	-5.97%	1.20	1.13	-5.42%
160	55.08	51.80	150.48	-5.95%	1.20	1.13	-5.42%
180	61.96	58.35	169.51	-5.83%	1.20	1.13	-5.42%
200	68.85	64.80	188.24	-5.88%	1.20	1.13	-5.42%
260	89.50	84.15	244.46	-5.98%	1.20	1.13	-5.42%
300	103.27	97.30	282.66	-5.78%	1.20	1.13	-104.52%

Table 5.3 - Output Results for Various Flaw Sizes at High Frequency Located at 1.20 m.

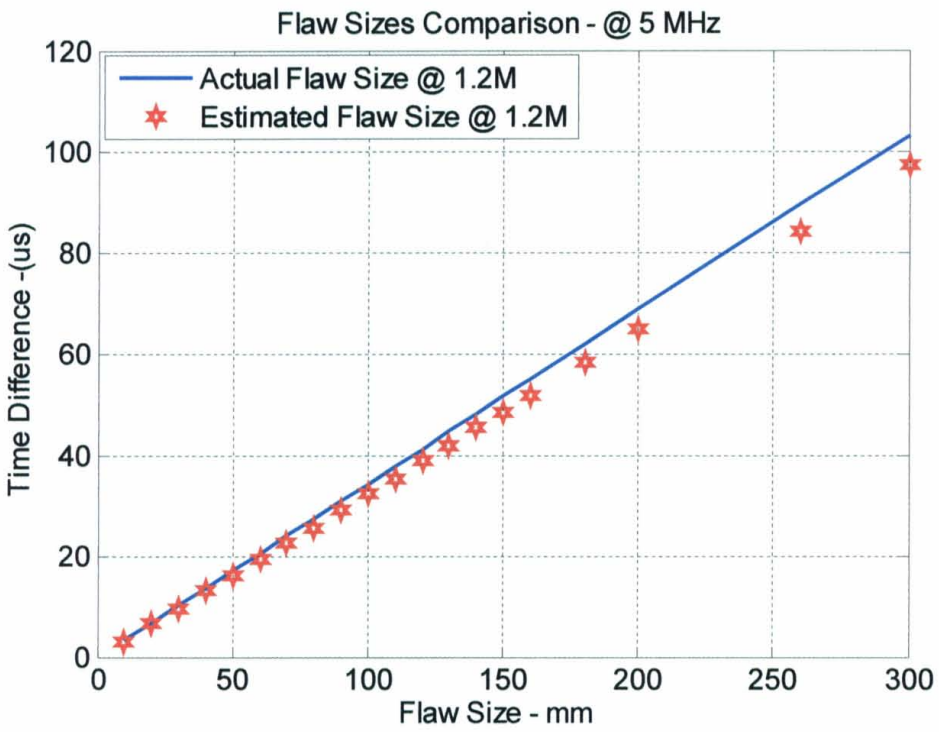

Figure 5.32 – Actual versus Estimated Flaws with Varying Sizes Located at 1.2M $-f_0$ (High Frequency -5MHz).

Figure (5.32) compares the estimated flaw sizes versus the actual flaw size; the estimated values almost agree with actual values with a percentage of error ranging from -7.04 % to -3.41 % providing accuracy ranging from -93% up to -96.6% for all the flaws greater than 10 millimeter, while the 10-millimeter flaw accuracy is -88.6%.

5.2.2.2 Simulation of Different Flaw Sizes at High Frequency Located at 2M

Figure (5.33) compares the estimated flaw sizes versus the actual flaw size; Table (5.4) indicates that the estimated values almost agree with actual values with a percentage of

error ranging from -8.78% to -3.41 % providing accuracy ranging from -91.22% to -96.6% for all the flaws greater than 10mm. While the 10-milimter flaw accuracy is -87.2%.

Actual Flaw Size (mm)	Actual Time Difference (μs)	Estimated Time Difference (μs)	Estimated Flaw Size (mm)	% of Error (±)	Actual Flaw Location (m)	Estimated Flaw Location (m)
10	3.44	3.00	8.72	-12.85%	2.0	1.89
20	6.88	6.65	19.32	-3.41%	2.0	1.89
25	8.61	7.85	22.80	-8.78%	2.0	1.89
30	10.33	9.70	28.18	-6.07%	2.0	1.89
40	13.77	13.30	38.64	-3.41%	2.0	1.89
50	17.21	16.25	47.21	-5.59%	2.0	1.89
60	20.65	19.30	56.07	-6.56%	2.0	1.89
70	24.10	22.80	66.23	-5.38%	2.0	1.89
80	27.54	25.95	75.38	-5.77%	2.0	1.89
90	30.98	29.40	85.41	-5.10%	2.0	1.89
100	34.42	32.45	94.27	-5.73%	2.0	1.89
110	37.87	35.50	103.13	-6.25%	2.0	1.89
120	41.31	39.10	113.59	-5.35%	2.0	1.89
130	44.75	42.05	122.16	-6.03%	2.0	1.89
140	48.19	45.10	131.02	-6.42%	2.0	1.89
150	51.64	48.75	141.62	-5.59%	2.0	1.89
160	55.08	51.80	150.48	-5.95%	2.0	1.89
180	61.96	58.35	169.51	-5.83%	2.0	1.89
200	68.85	64.90	188.53	-5.73%	2.0	1.89
260	89.50	84.13	244.40	-6.00%	2.0	1.89
300	103.27	97.37	282.85	-5.72%	2.0	1.89

Table 5.4 - Output Results for Various Flaw Sizes at High Frequency Located at 2.0 m.

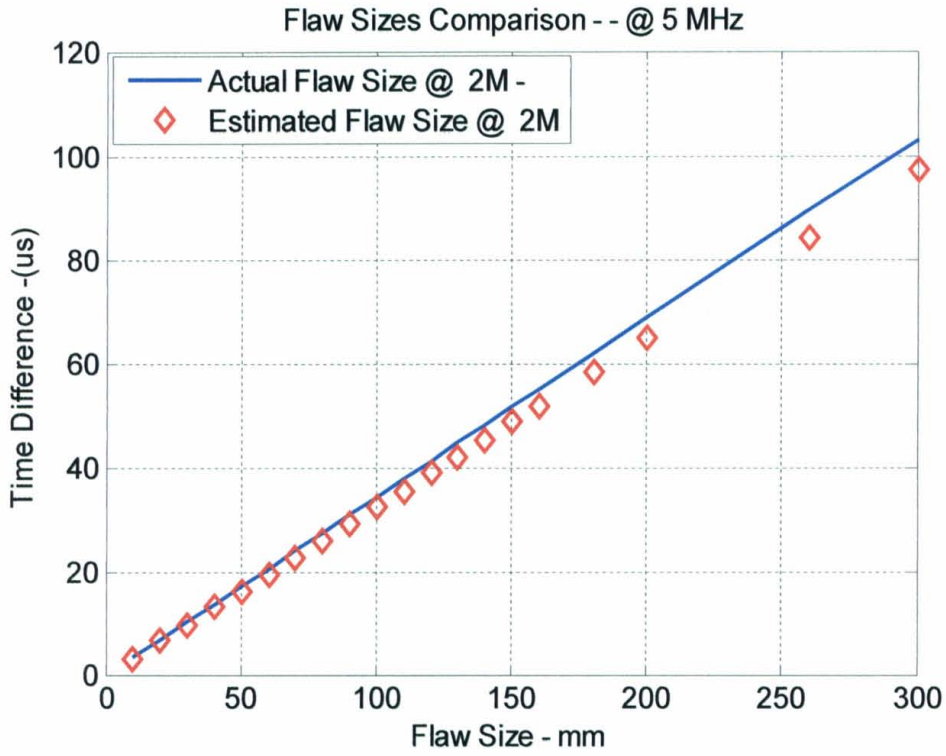

Figure 5.33 – Actual versus Estimated Flaws with Varying Sizes Located at 2.0 M – f_0 (High Frequency -5MHz).

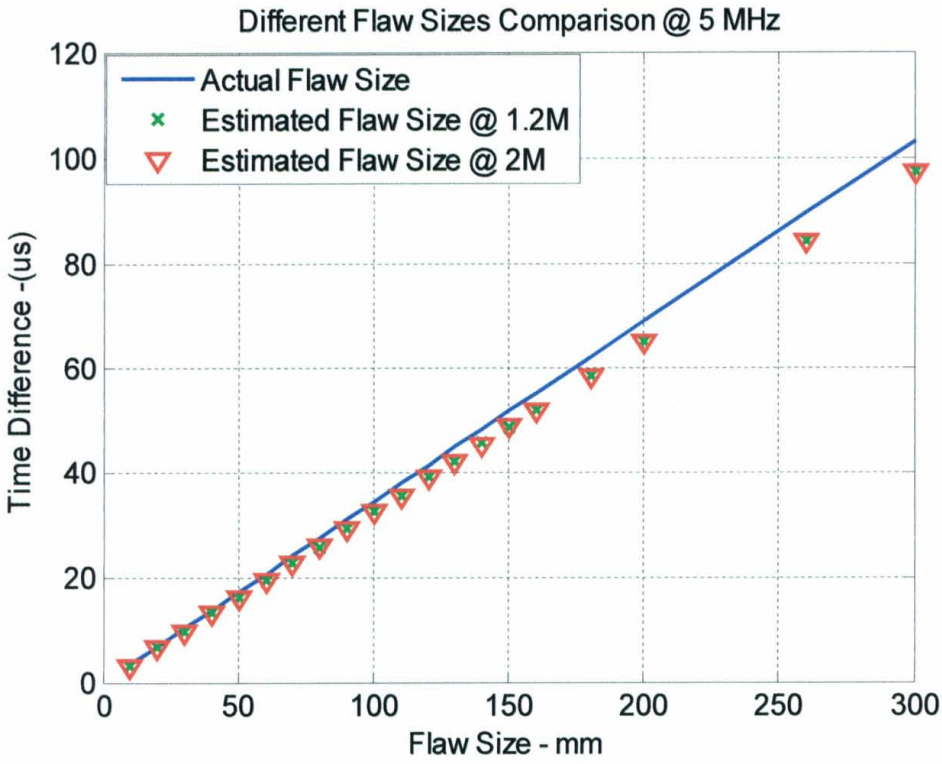

Figure 5.34 – Actual versus Estimated Flaws with Varying Sizes Located at 1.2 M & 2.0 M – f_0 (High Frequency -5MHz).

Figure (5.34) illustrates actual flaw sizes versus flaw sizes estimated at the high frequency, 5MHz KHz located at two different distances 1.20 meters and 2.0 meters. The estimated values almost agree with the actual values line for both distances with slight variation.

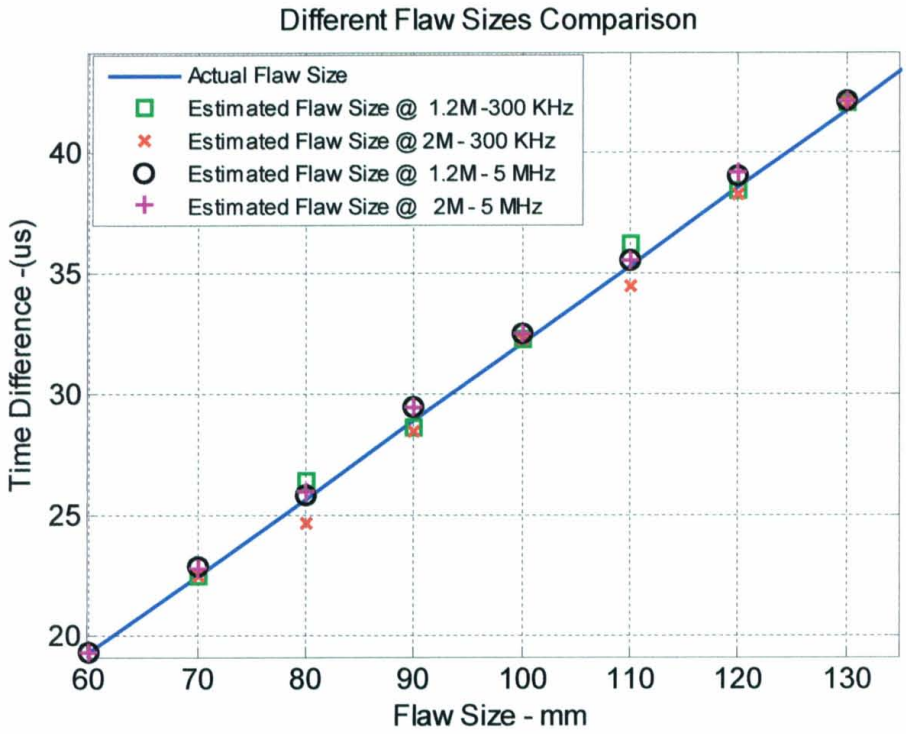

Figure 5.35 - Comparison of Actual and Estimated Flaws with Varying Sizes Located at 1.2 meters and 2.0 meters at Central Frequencies = 300 kHz and 5MHz.

Figure (5.35) illustrates actual flaw sizes versus flaw sizes estimated at the high frequency, 5MHz and low frequency, 300 kHz located at two different distances 1.20 meters and 2.0 meters. The estimated values almost agree with the actual values line for both distances and for both frequencies with slight variation.

5.3 SIMULATION OF DIFFERENT FLAW SIZES LOCATED AT VARIOUS DISTANCES

Another simulation was made using the parameters of the pipe in reference (Wang et al., 2010) and at the same specified frequency of 420 KHz, but the length of pipe is 10 meters. Flaws with different sizes: 16, 20, 24, 30, 44, 66 and 100 mm were introduced on the pipe located at different locations along the 10-meter length. For each flaw size, the flaw is kept constant and its location is varied along the pipe 0.5 – meter interval.

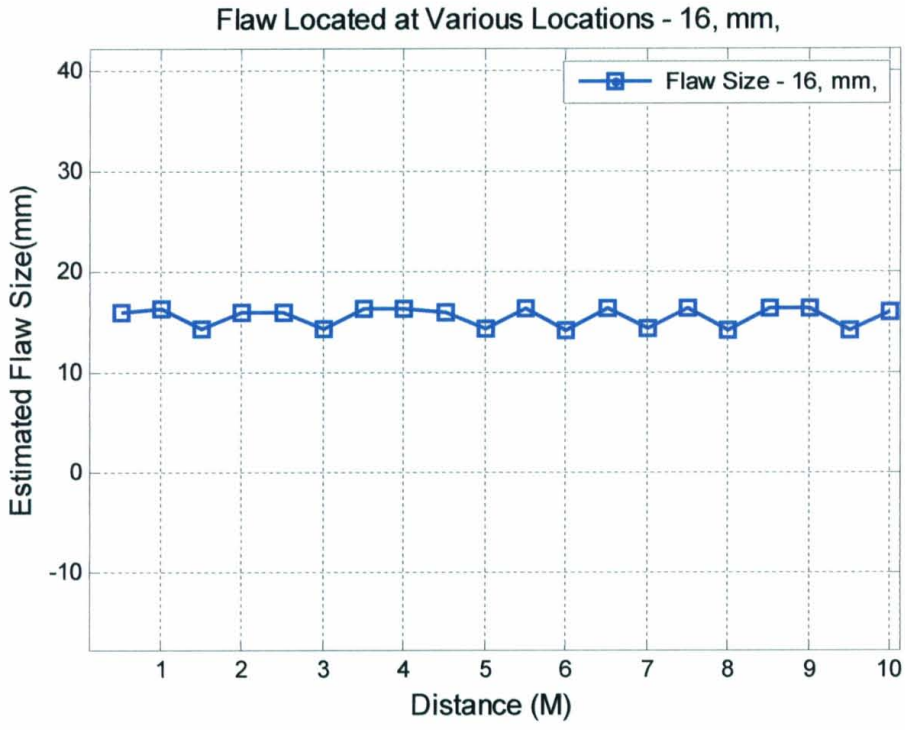

Figure 5.36 – 16 mm Estimated Flaw Size versus Distance Plot.

Figure (5.36) shows the predicted flaw size of 16 mm located at different points along the 10-meter pipe, the flaw size was kept constant and its location was varied in 0.5–meter interval along the 10-meter pipe. The Figure shows that as the location of the flaw changes the estimated flaw size varies insignificantly when compared with the actual flaw size.

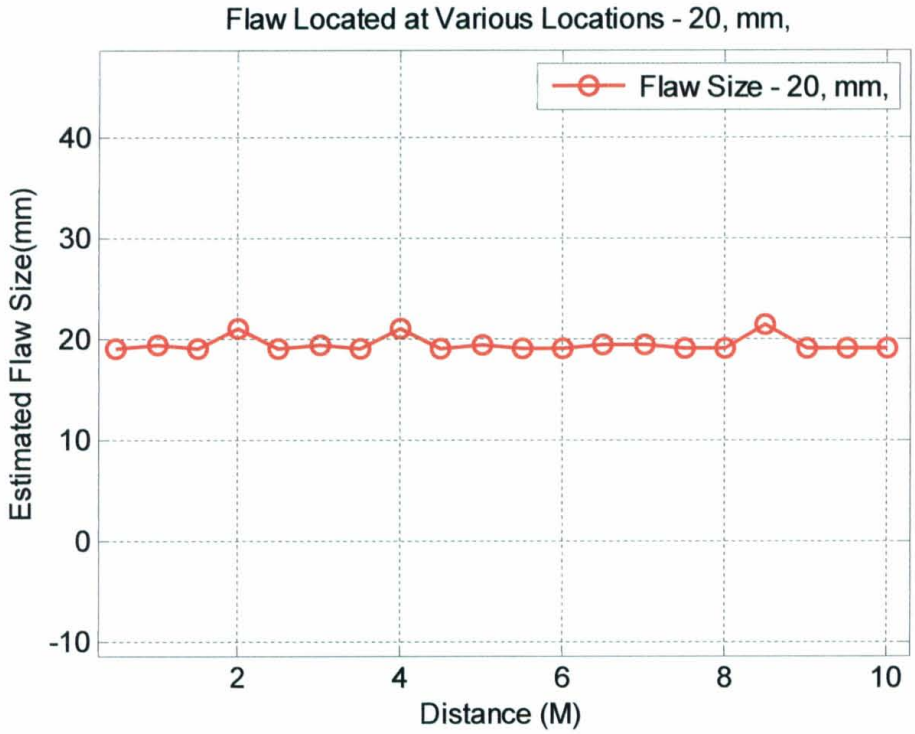

Figure 5.37 – 20 mm Estimated Flaw Size versus Distance Plot.

Figure (5.37) shows the predicted flaw size of 20 mm located at different points along the 10-meter pipe, the flaw size was kept constant as the location was varied along the pipe. The figure portrays that the predicted flaw size almost agrees with the actual flaw size as the location of the flaw changes along the pipe.

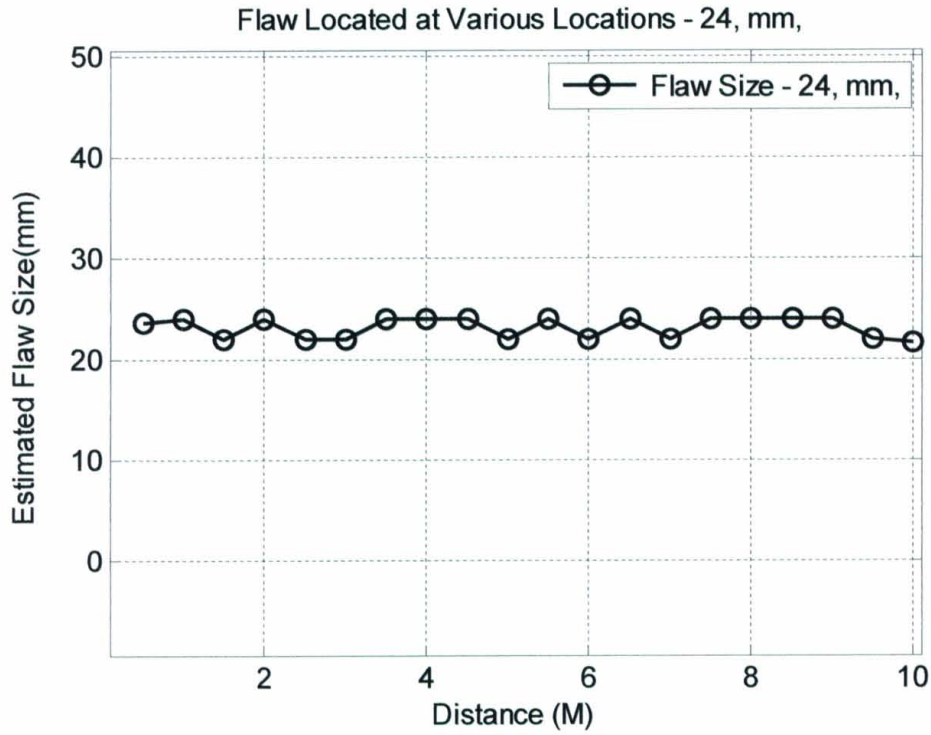

Figure 5.38– 24 mm Estimated Flaw Size versus Distance Plot.

Figure (5.38) shows the predicted flaw size of 24 mm located at different points along the 10-meter pipe, again the flaw size was kept the same at 24 mm radius and its location was varied along the pipe. The estimated flaw size at each location varied insignificantly when compared with actual flaw size as it can be seen from the Figure.

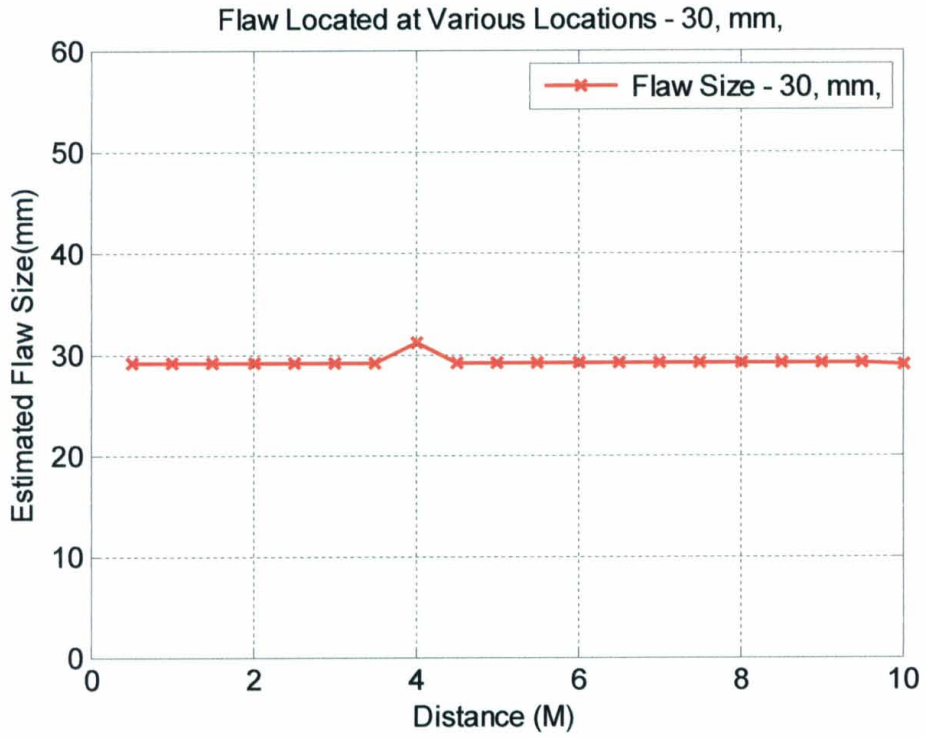

Figure 5.39 – 30 mm Estimated Flaw Size versus Distance Plot.

Figure (5.39) shows that the predicted flaw size of 30 mm located at different points along the 10-meter pipe was steady all over the range of distances, the only noticeable change can be seen at 4 mete which is insignificant.

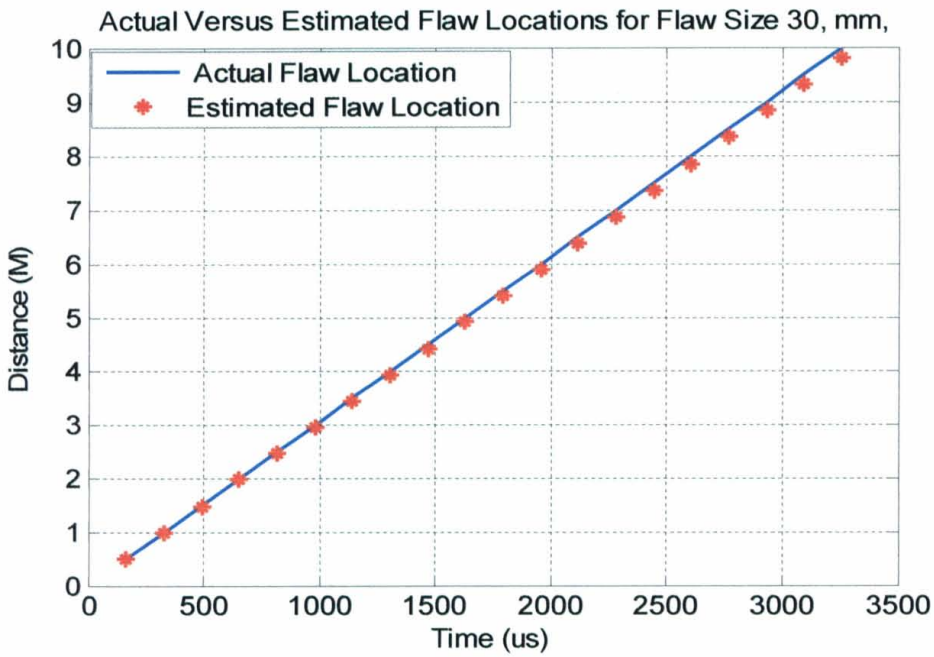

Figure 5.40 – Comparison between the Estimated and Actual Location for 30mm - Flaw.

Figure (5.40) compares the actual flaw location versus the estimated flaw location for a 30 mm flaw located at different distances along the 10-meter pipe. As indicated from the Figure that there is very little variation between the actual and the estimated distance. As the distance or location of the flaw goes beyond 4.8 meter; this variation starts to increase but this increase in variation is insignificant as depicted from the Figure and does not affect the accuracy of the result.

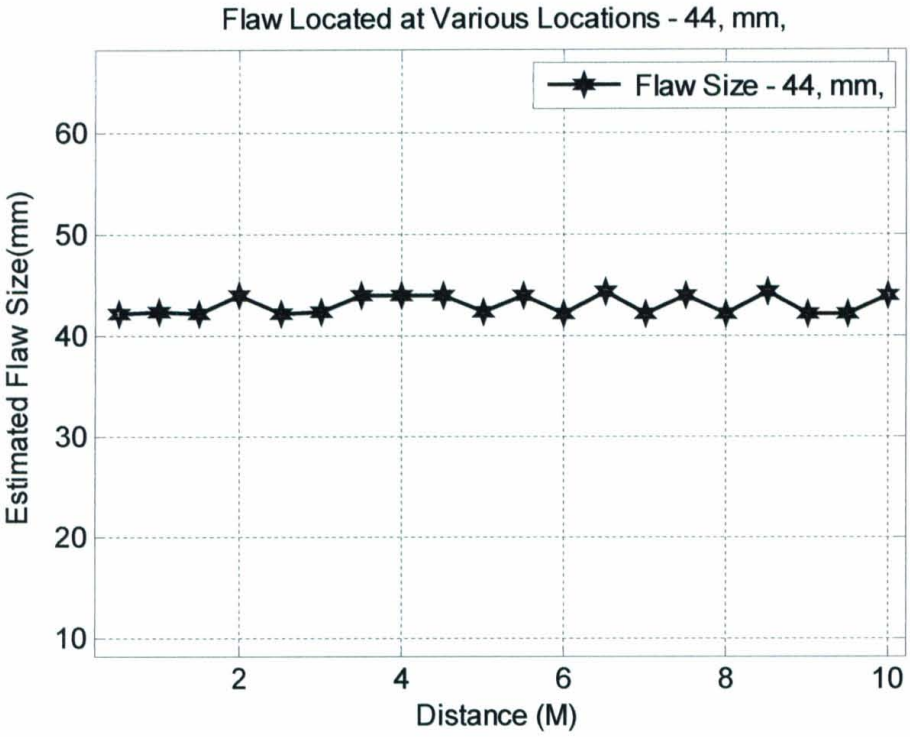

Figure 5.41 – 44 mm Estimated Flaw Size versus Distance Plot.

Figure (5.41) shows the estimated flaw size versus the distance for a 44 mm flaw located at various points along the pipe. The Figure shows that as the flaw location changes along the pipe, the estimated flaw size almost agrees with the actual flaw size.

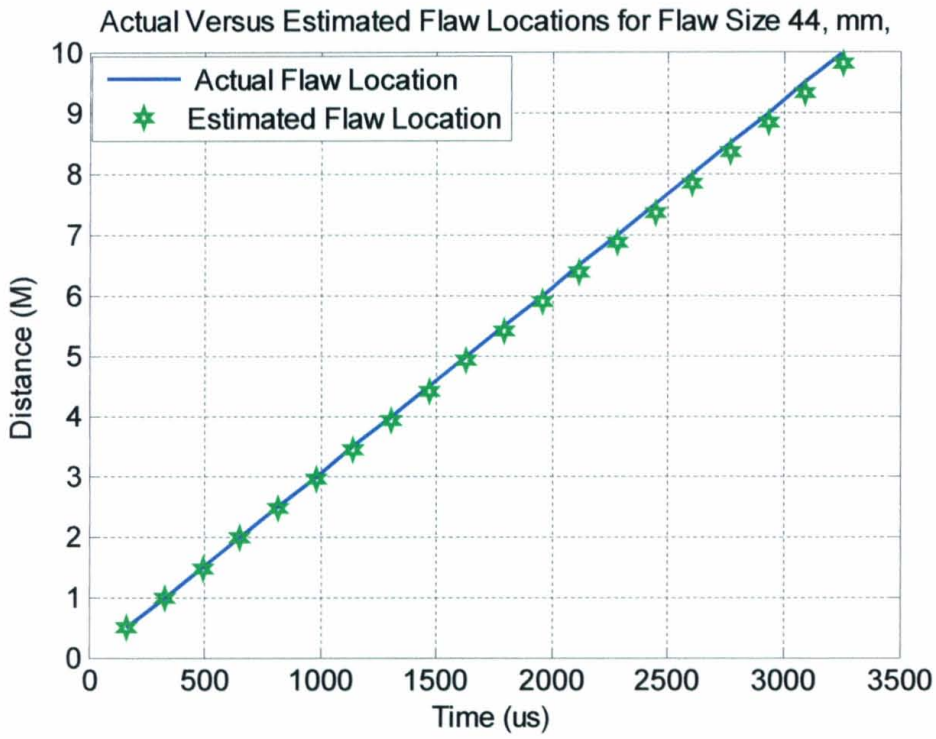

Figure 5.42 – Comparison between the Estimated and Actual Location for 44mm - Flaw.

Figure (5.42) compares the actual flaw location versus the estimated flaw location for the 44-milimter flaw. The Figure shows very little variation between the actual and the estimated distances. As the distance or location of the flaw goes beyond 4.5 meter; this variation starts to increase but this increase in variation is insignificant.

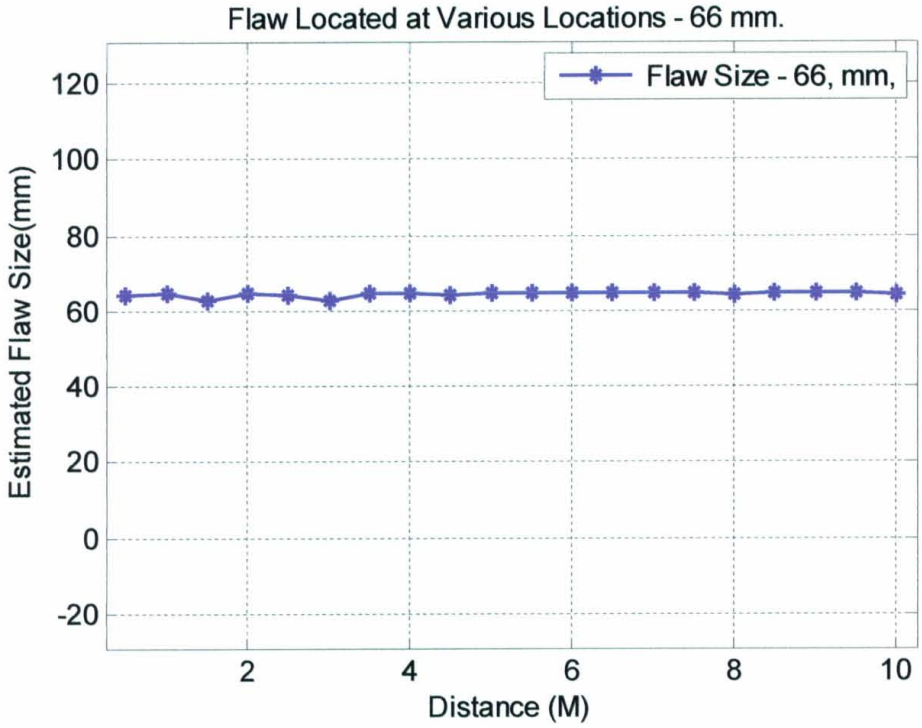

Figure 5.43 – 66 mm Estimated Flaw Size versus Distance Plot.

Figure (5.43) shows the estimated flaw size versus the distance for a 66 mm flaw located at various points along 10-meter pipe. The Figure shows that the estimated size of the flaw is almost the same as the actual size of the flaw along the pipe.

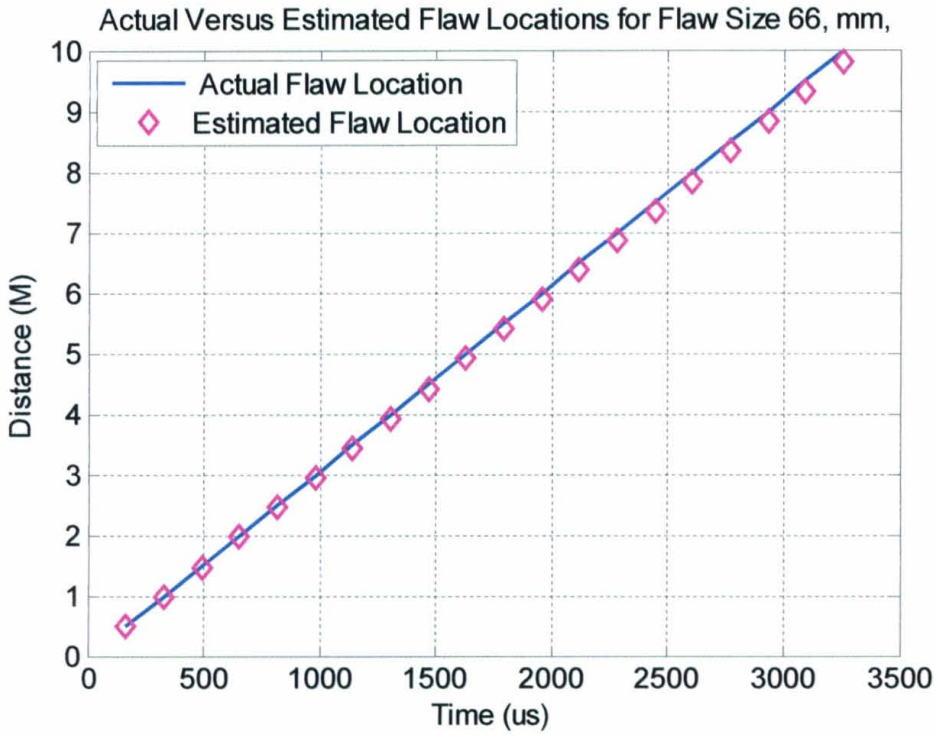

Figure 5.44 – Comparison between the Estimated and Actual Location for 44mm - Flaw.

Figure (5.44) compares the actual flaw location versus the estimated flaw location for 66-milimter flaw. There is very little variation between the actual and the estimated distance. This variation starts to increase beyond the 5-meer region but this increase in variation is insignificant.

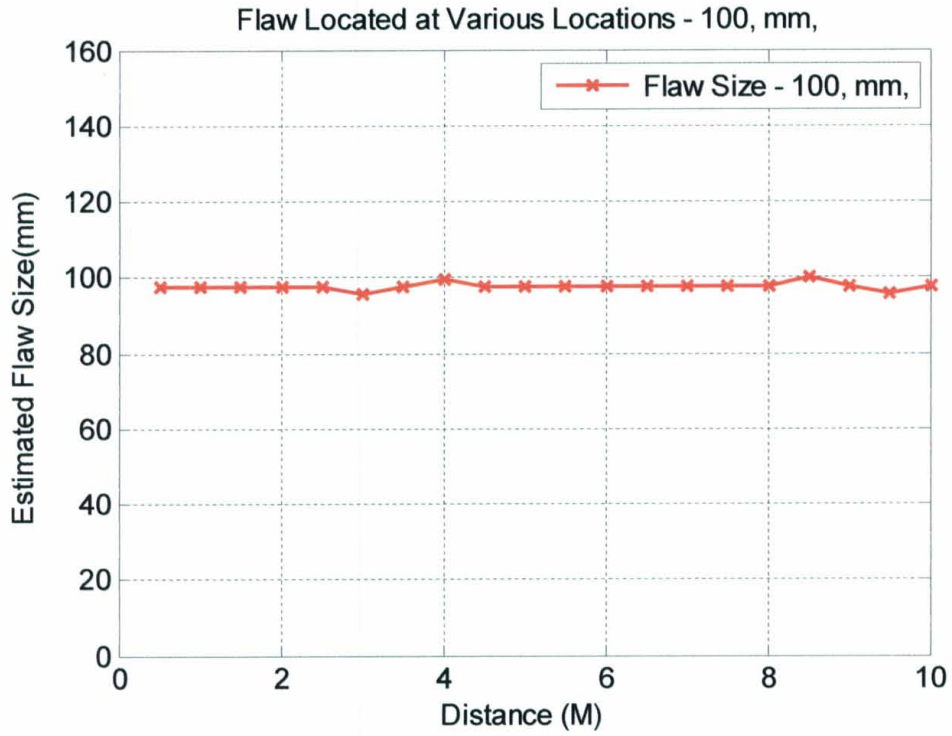

Figure 5.45 – 100 mm Estimated Flaw Size versus Distance Plot.

Figure (5.45) shows the estimated flaw size versus the distance for a 100 mm flaw located at various points along 10-meter pipe. The Figure shows that when changing the flaw location along the pipe the estimated size of the flaw is almost the same as the actual size of the flaw.

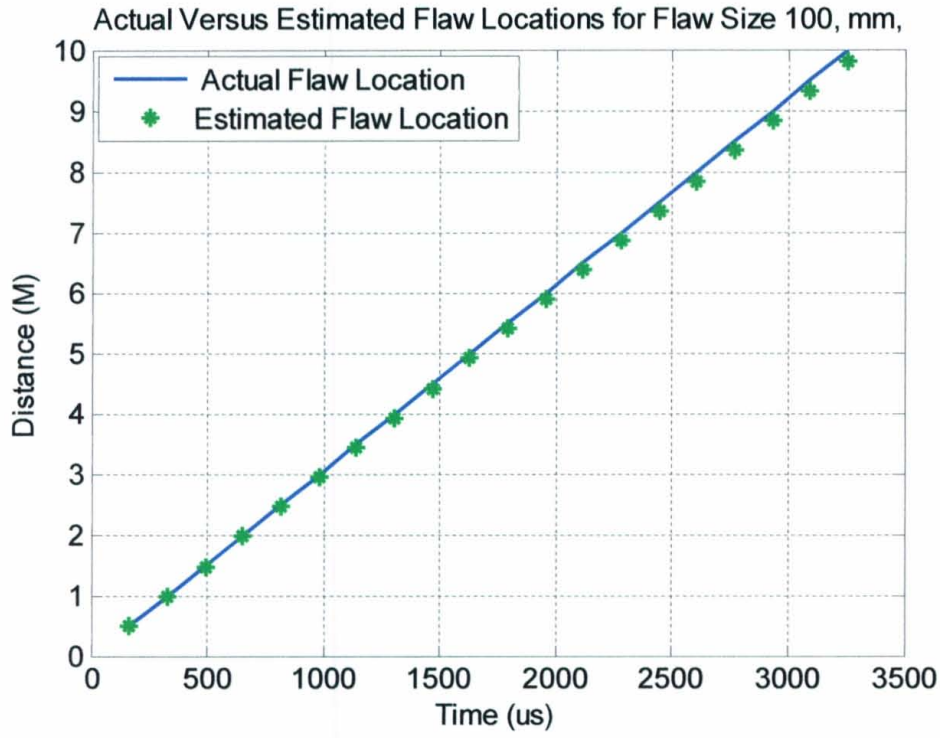

Figure 5.46 – Comparison between the Estimated and Actual Location for 100 mm - Flaw.

Figure (5.46) compares the actual flaw location versus the estimated flaw location. The figure indicates that there is slight variation between the actual and the estimated distances when the flaw is located at 4.8 meter and beyond.

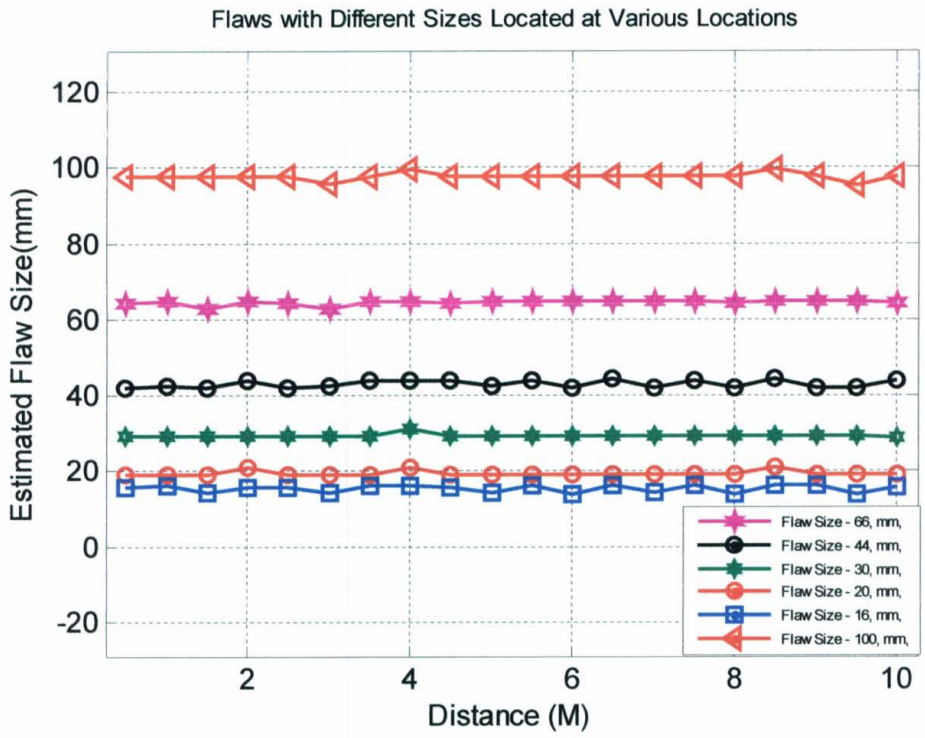

Figure 5.47 – Estimated Flaw Sizes versus Distance – Comparison of All Flaws Located at Different Distances.

Figure (5.47) shows the estimated flaw sizes for all the flaws considered in the analysis with sizes 16, 20, 30, 44, 66 and 100 mm versus the various locations along the 10-meter pipe. As it can be seen from the Figure that as the location of the flaw changes the estimated flaw size varies insignificantly when compared to the actual size of the flaw which does not affect the accuracy of the result.

CHAPTER 6

EXPERIMENTAL ANALYSIS AND RESULTS

In this chapter the results of experiments reported in two research papers (Wang, Tse, Mechefske & Meng, 2010) and (Aiello, Dilettoso & Salerno, 2005) for sizing flaws with varying dimensions will be compared with the simulation results obtained using the method suggested in this thesis. The subsequent sections provide the relevant details and the results pertaining to each experiment.

It should be noted, that one of the underlying assumptions of the modified model suggested in this thesis is that the flaw has an isotropic spherical shape with a given radius. To use this model for the estimation of actual flaws, one can use one of the following two approaches:

The surface of a rectangular shape is obtained by unwrapping the spherical shape as shown in Figure (6.1).

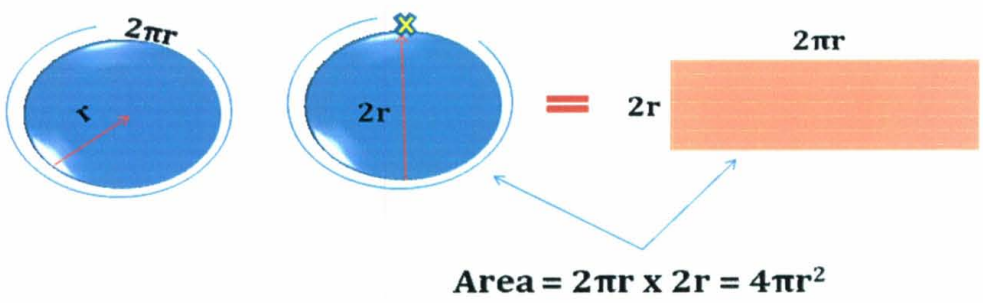

Figure 6.1 – Schematic Showing the Sphere and the Unwrapped Sphere Equivalence.

In this case, the assumed axial extent of the flaw in the experiment is equivalent to $2\pi r$ mm, the radius of the sphere is $r = x / \pi$, where x is the dimension of the flaw and this is the value that will be used in the Equation to calculate the response of the assumed spherical flaw. Then the response of the flaw obtained from simulation will approximate the radius of the flaw (r), which will be substituted back into $2\pi r$ to get the full length.

The second approach is to assume that the dimension of the flaw is equal to 2r as shown in Figure (6.2).

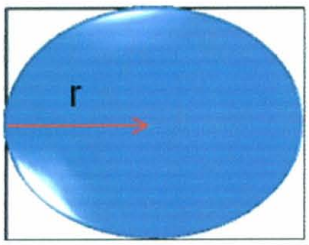

Figure 6.2 – Fitting the External Surface of the Sphere into a Square.

It really, does not matter here as long as we are evaluating the length of the flaw whether in the circumferential or axial direction. The model takes r, the radius of the flaw as the input parameter which is half of the length of the flaw.

It has been found that second approach gives better estimates than the first approach. Therefore, in this work will take the second approach in estimating actual flaws.

Other points to note are that the responses of longitudinal waves can accurately determine the location and the size of the axial extent of the flaw while the responses of torsional waves can provide the information about the circumferential extent of the flaw.

6.1 2.0 – METER STEEL PIPE, FLAW WITH 10 MM AXIAL EXTENT AND 10° IN THE CIRCUMFERENTIAL DIRECTION

Under this section the results of an experiment for sizing the flaw will be compared with simulation results produced by this research. According to (Aiello et al., 2005), a 2-meter steel pipe with 43 mm external radius and 37.5 mm internal radius having flaw with axial extent of 10 mm, and 10° in the circumferential direction was investigated. The flaw is located at a distance of 350 mm. The perimeter of the pipe is equal to $2\pi \times r = 86\pi$ and the circumferential extent at 10^{0} becomes $2.39\ \pi = 7.51$ mm.

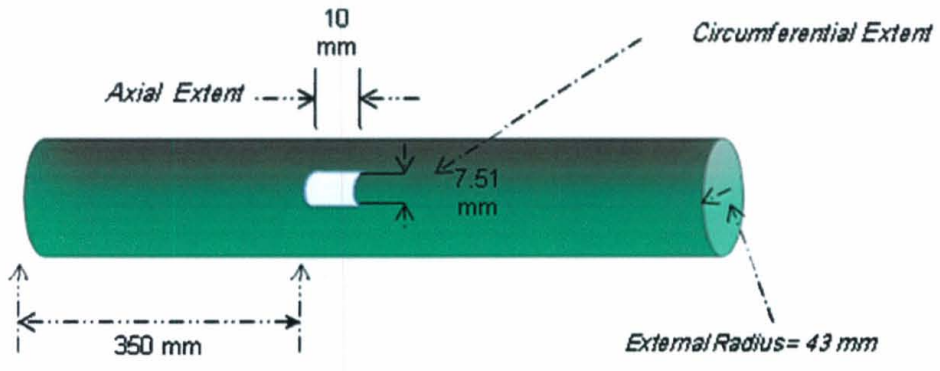

Figure 6.3 – Details of the Pipe in the First Experiment (Aiello et al., 2005).

6.1.1 Results for the Circumferential Flaw

The central frequency was selected to be 420 kHz and from the dispersion curves the group speed at this frequency is 3126 m/s for the torsional wave T(0,1) as shown in Figure (6.4). The output results as given by the program and the flaw-free and flaw signals are shown in Figure (6.5).

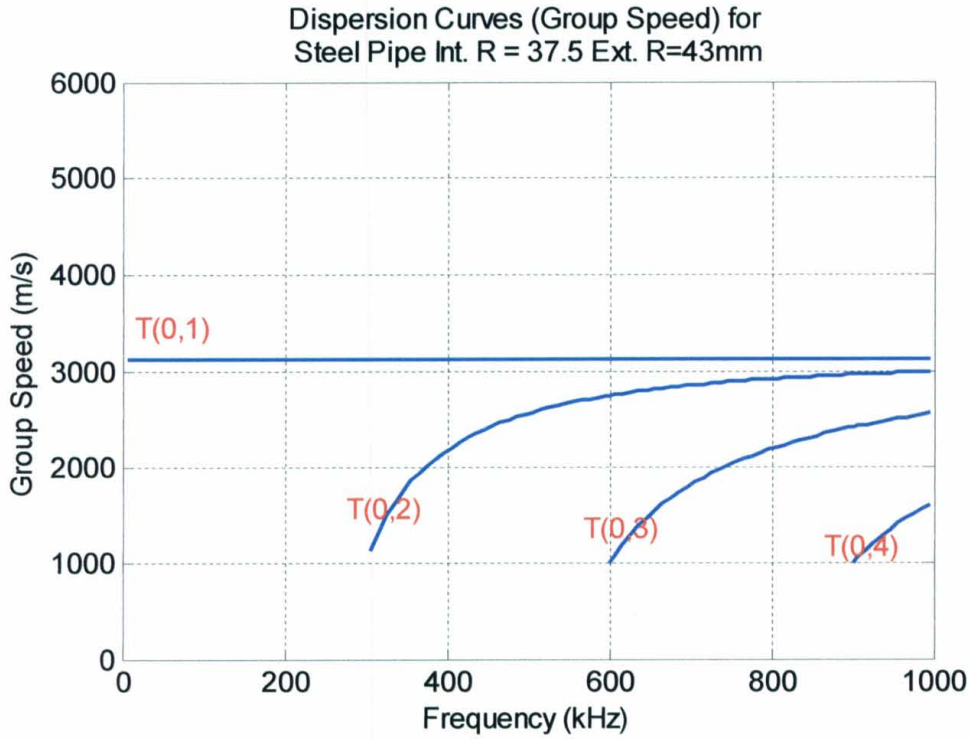

Figure 6.4 – Dispersion Curve for Steel Pipe with Internal and External Radii, 37.5 and 43.0 mm.

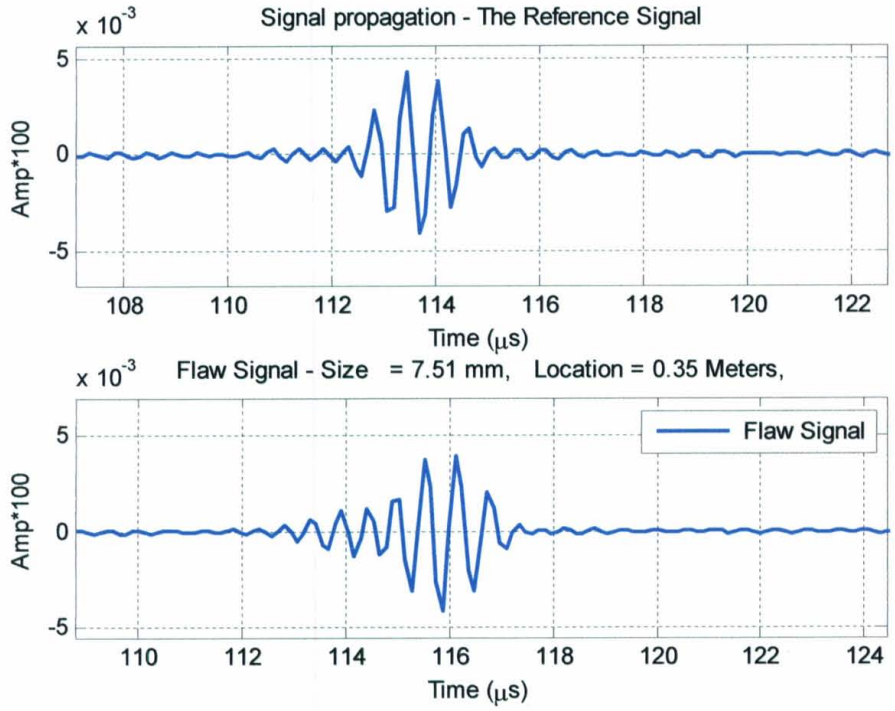

Figure 6.5 – Time Domain Response for the 7.51 mm Circumferential Flaw Located at 0.35 Meter.

Output Data:

Time at the Highest Amplitude - Ref. Signal:	*113.431 μs*
Time at the Highest Amplitude - Flaw Signal:	*116.117 μs*
Time Difference between Ref. and Flaw Signals:	*1.3431 μs*
Actual Flaw Location:	*0.35 meters*
Estimated Flaw Location:	*0.354585 meters*
Percentage of Error:	*1.3101 %*
Actual Flaw Size:	*7.51 mm*
Estimated Flaw Size:	*8.39707 mm*
Percentage of Error:	*11.8118 %*

The actual flaw size was 7.51 mm while the estimated was 8.4 mm resulting in an error of 11.8%. This is a limitation of the model that as the size of the flaw goes below 10 mm the percentage of error start to increase.

6.1.2 Results for the Axial Flaw

The output results and the flaw response Figures are shown below in Figure (6.7). The central frequency was selected to be 420 kHz and from the dispersion curves the group speed at this frequency is 3099.5 m/s for the longitudinal wave L(0,1) as shown in Figure (6.6).

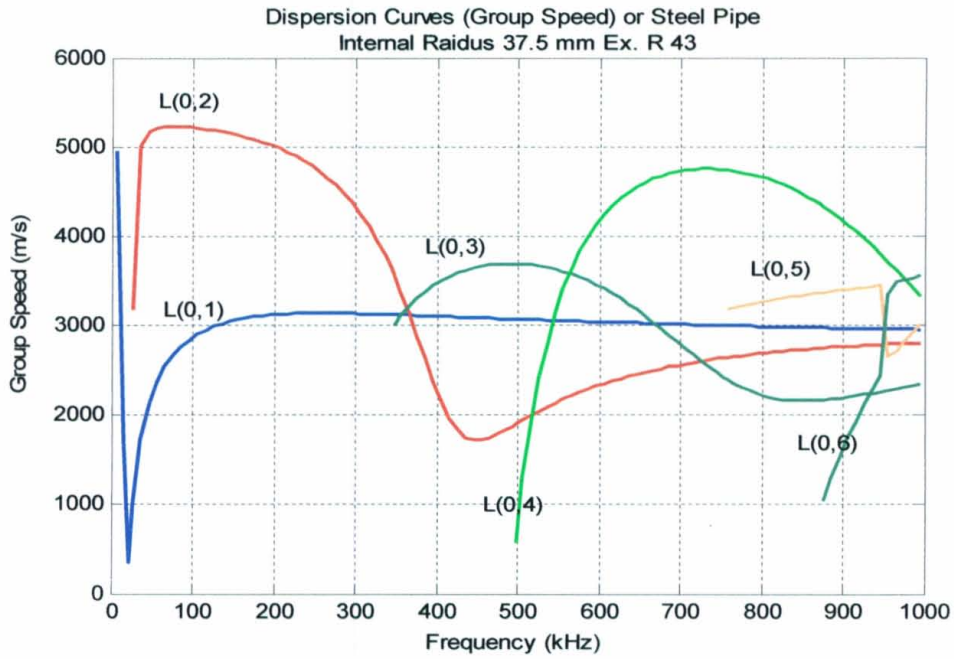

Figure 6.6- Group Speed Dispersion Curves for a Steel Pipe with 37.5 mm Internal Radius and 43 mm External Radius.

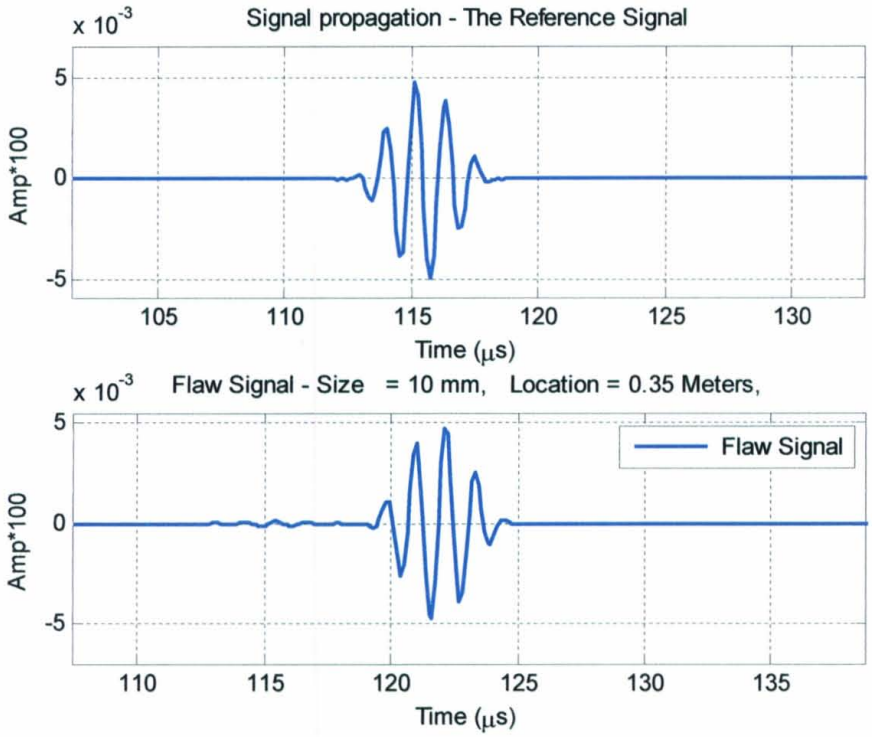

Figure 6.7 – Time Domain Response for the 10.0 mm Axial Flaw Located at 0.35 m.

Output Data:

Time at the Highest Amplitude - Ref. Signal:	*120.521 μs*
Time at the Highest Amplitude - Flaw Signal:	*123.909 μs*
Time Difference between Ref. and Flaw Signals:	*1.69383 μs*
Actual Flaw Location:	*0.35 meters*
Estimated Flaw Location:	*0.373556 meters*
Percentage of Error:	*6.7302 %*
Actual Flaw Size:	*10 mm*
Estimated Flaw Size:	*10.5 mm*
Percentage of Error:	*5.00046 %*

The percentage of error is about 5% for the estimation of the flaw; this is a good approximation with an acceptable percentage of error. The estimated location of the flaw is 0.37 meter resulting in 6.7% of error which is acceptable.

6.2 2.030-METER STEEL PIPE, FLAWS WITH DIFFERENT SIZES

Under this section the results of an experiment for sizing the flaw will be compared with simulation results produced by this research. A steel pipe with flaws having different sizes 3, 6, 14, 16, 21, 24, 27, 29, 37, 42 and 86 mm in the axial direction at a distance of 1.3 meter was tested as per (Wang et al., 2010). The length of the pipe is 2.030 meters with external radius 17 mm and internal radius of 15 mm.

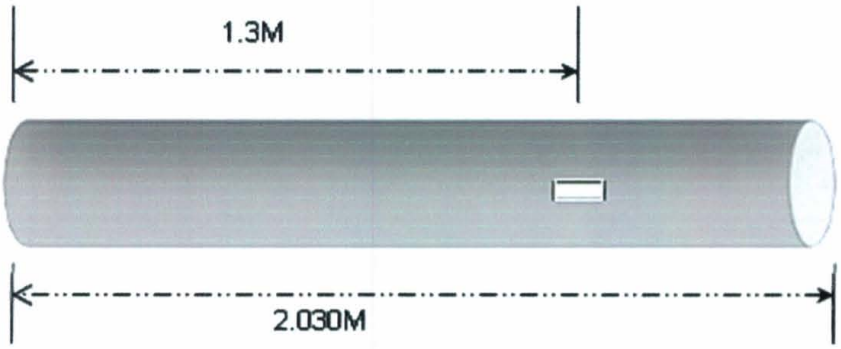

Figure 6.8 –Details of the Pipe in the Second Experiment (Wang et al., 2010).

6.2.1 Input Data:

Central Frequency:	420000 Hz
Group Speed @ the Specified Frequency:	3076 m/s
Time at the Highest Amplitude - Reference Signal:	418.071 μs

Flaw sizes (mm): (3, 6, 14, 16, 21, 24, 27, 29, 37, 42, 86) mm

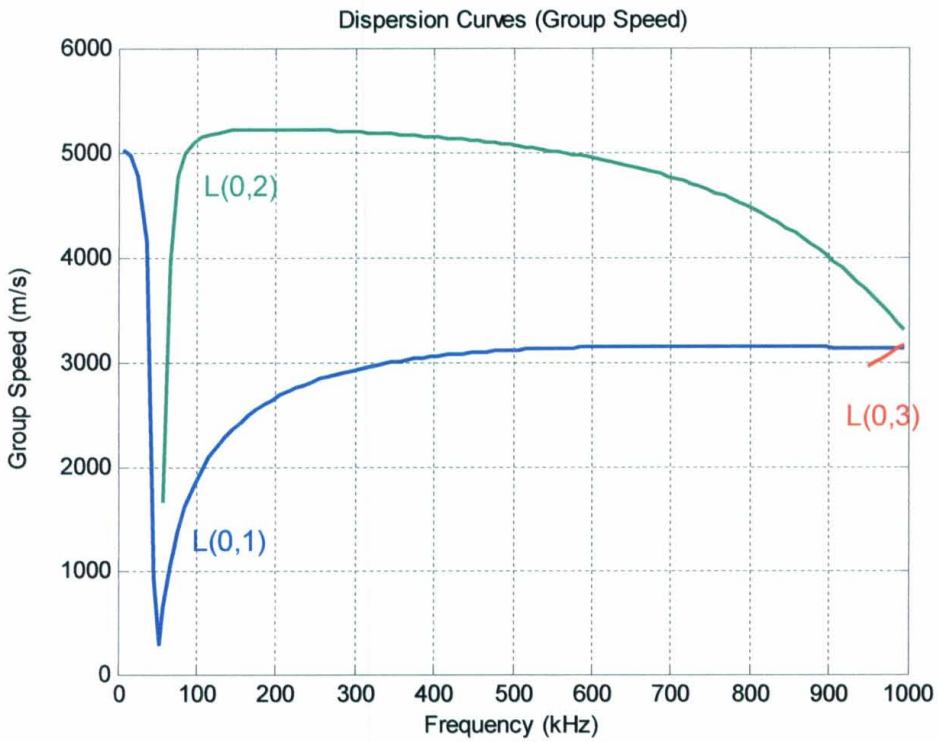

Figure 6.9 – Dispersion Curves Showing Group Speed for a Steel Pipe with Internal Radius 15mm and External Radius 17mm.

6.2.2 Output Data

The output results for some selected flaw sizes are shown below, the output data and the response plots in time domain.

Flaw size, 3mm located at 1.3 meter:

Time at the Highest Amplitude - Ref. Signal:	*418.264 μs*
Time at the Highest Amplitude - Flaw Signal:	*419.973 μs*
Time Difference between Ref. and Flaw Signal:	*0.854597 μs*
Actual Flaw Location:	*1.3 meters*
Estimated Flaw Location:	*1.28658 meters*
Percentage of Error:	*-1.03232 %*
Actual Flaw Size:	*3 mm*
Estimated Flaw Size:	*2.62874 mm*
Percentage of Error:	*-12.3754%*

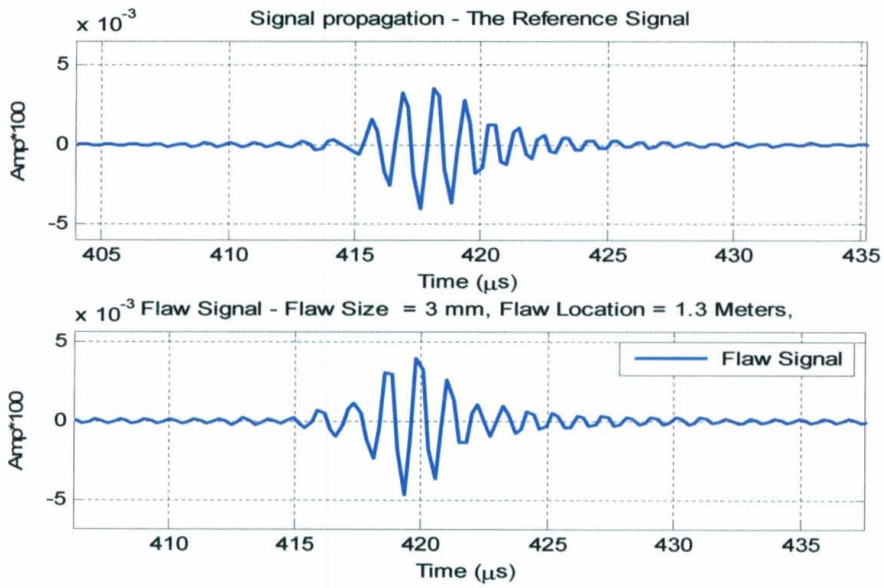

Figure 6.10 - The Time Domain Response for the 3 mm Axial Flaw Located at 1.3 meter

Flaw size, 6mm located at 1.3 meter:

Time at the Highest Amplitude - Ref. Signal:	*418.264 μs*
Maximum Amplitude - Ref. Signal:	*0.431125*
Time at the Highest Amplitude - Flaw Signal:	*422.293 μs*
Maximum Amplitude - Flaw Signal:	*0.424454*
Amplitude Difference between Ref. and Flaw Signals:	*-0.00667107*
Time Difference between Ref. and Flaw Signals:	*2.01441 μs*
Actual Flaw Location:	*1.3 meters*
Estimated Flaw Location:	*1.28658 m*
Percentage of Error:	*-1.03%*
Actual Flaw Size:	*6 mm*
Estimated Flaw Size:	*6.19631 mm*
Percentage of Error:	*3.27188 %*

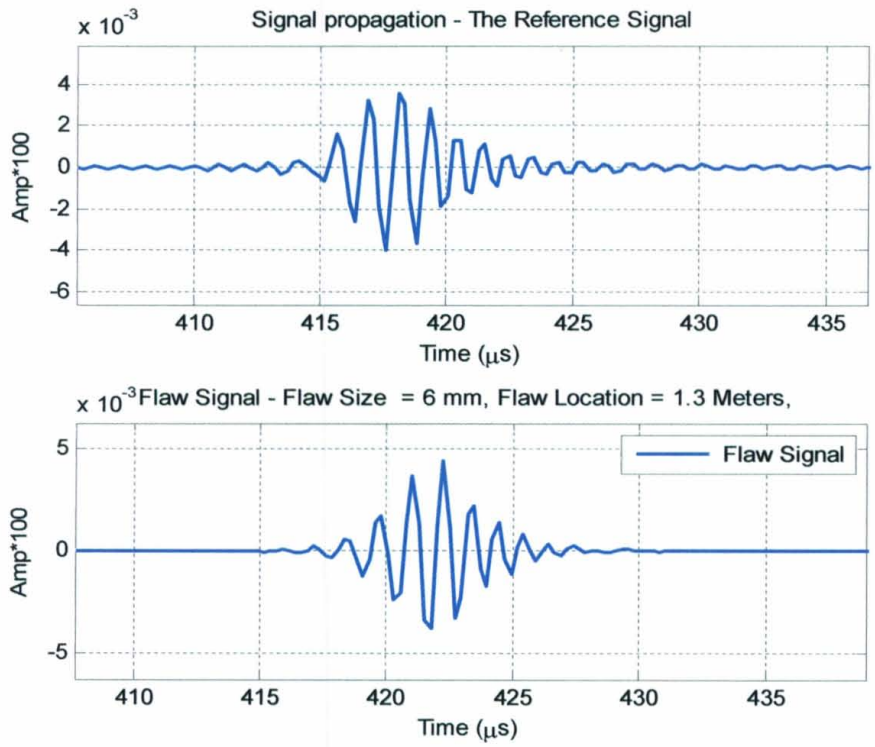

Figure 6.11 – The Time Domain Response for the 6.0 mm Flaw Located at 1.3 meter.

Flaw size, 14mm located at 1.3 meter:

Time at the Highest Amplitude - Ref. Signal:	*418.264 μs*
Maximum Amplitude - Ref. Signal:	*0.431125*
Time at the Highest Amplitude - Flaw Signal:	*427.298 μs*
Maximum Amplitude - Flaw Signal:	*0.422625*
Time Difference Between Ref. and Flaw Signals(us):	*4.51715 μs*
Actual Flaw Location:	*1.3 meters*
Estimated Flaw Location:	*1.28658 m*
Percentage of Error:	*-1.03232%*
Actual Flaw Size:	*14 mm*
Estimated Flaw Size:	*13.8948 mm*
Percentage of Error:	*-0.751696%*

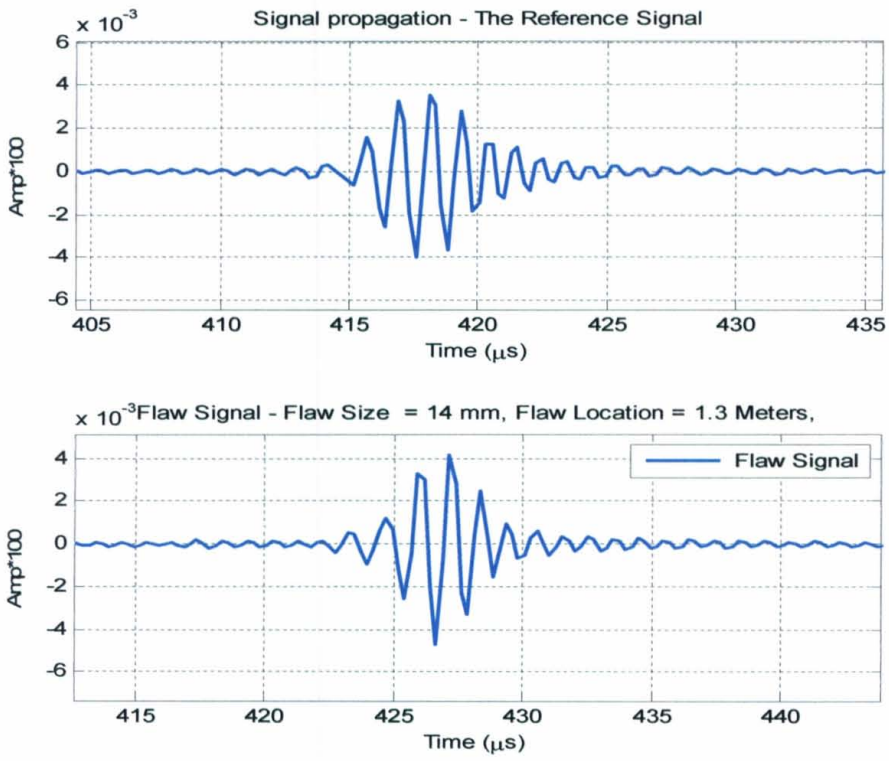

Figure 6.12 – The Time Domain Response for the 14.0 mm Flaw Located at 1.3 meter.

Flaw size, 16mm located at 1.3 meter:

Time at the Highest Amplitude - Ref. Signal:	*418.264 μs*
Maximum Amplitude - Ref. Signal:	*0.431125*
Time at the Highest Amplitude - Flaw Signal:	*428.763 μs*
Time Difference between Ref. and Flaw Signals:	*5.24966 μs*
Actual Flaw Location:	*1.3 meters*
Estimated Flaw Location:	*1.28658 meters*
Percentage of Error:	*-1.03232 %*
Actual Flaw Size:	*16 mm*
Estimated Flaw Size:	*16.148 mm*
Percentage of Error:	*0.924796 %*

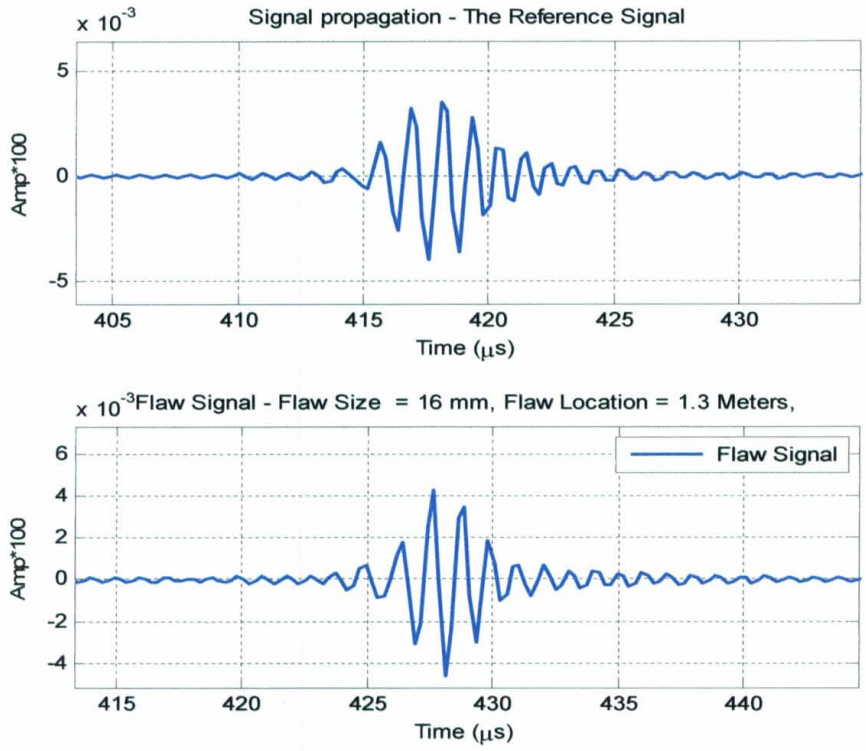

Figure 6.13 – The Time Domain Response for the 16.0 mm Flaw Located at 1.3 meter.

Flaw size, 37mm located at 1.3 meter:

Time at the Highest Amplitude - Ref. Signal:	*418.264 μs*
Maximum Amplitude - Ref. Signal:	*0.431125*
Time at the Highest Amplitude - Flaw Signal:	*441.46 μs*
Maximum Amplitude - Flaw Signal:	*0.425802*
Amplitude Difference between Ref. and Flaw Signals:	*-0.00532331*
Time Difference between Ref. and Flaw Signals:	*11.5981 μs*
Actual Flaw Location:	*1.3 meters*
Estimated Flaw Location:	*1.28658 meters*
Percentage of Error:	*-1.03232 %*
Actual Flaw Size:	*37 mm*
Estimated Flaw Size:	*35.6757 mm*
Percentage of Error:	*-3.57908%*

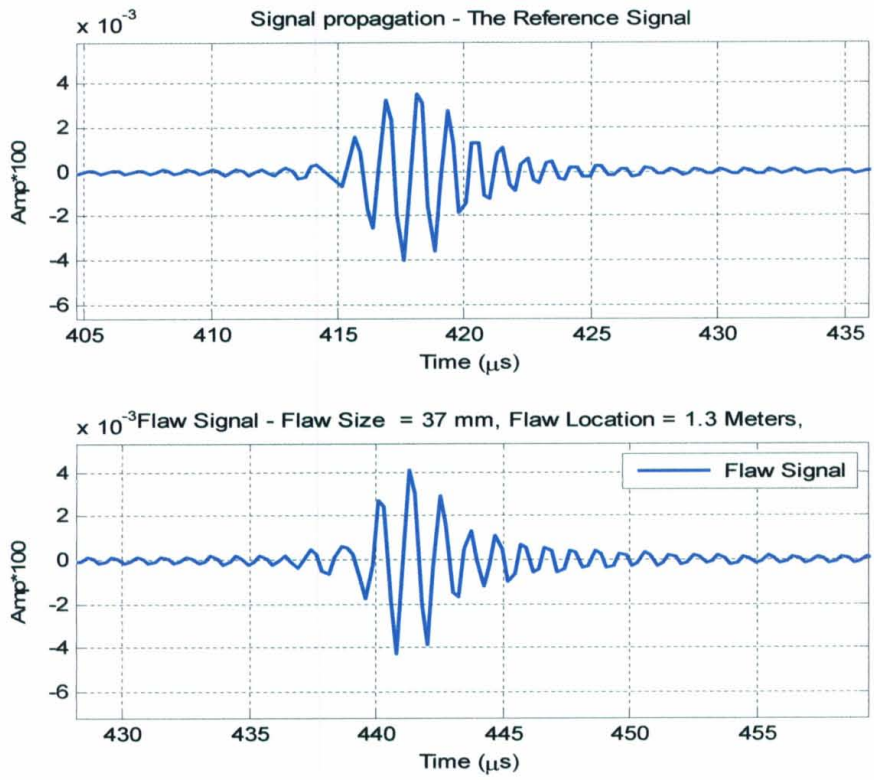

Figure 6.14 – The Time Domain Response for the 37.0 mm Flaw Located at 1.3 meter.

Flaw size, 42mm located at 1.3 meter:

Time at the Highest Amplitude - Ref. Signal:	*418.264 μs*
Maximum Amplitude - Ref. Signal:	*0.431125*
Time at the Highest Amplitude - Flaw Signal:	*445.245 μs*
Maximum Amplitude - Flaw Signal:	*0.39708*
Time Difference between Ref. and Flaw Signals:	*13.4904 μs*
Actual Flaw Location:	*1.3 meters*
Estimated Flaw Location:	*1.28658 meters*
Percentage of Error:	*-1.03232%*
Actual Flaw Size:	*42 mm*
Estimated Flaw Size:	*41.4965 mm*
Percentage of Error:	*-1.19876%*

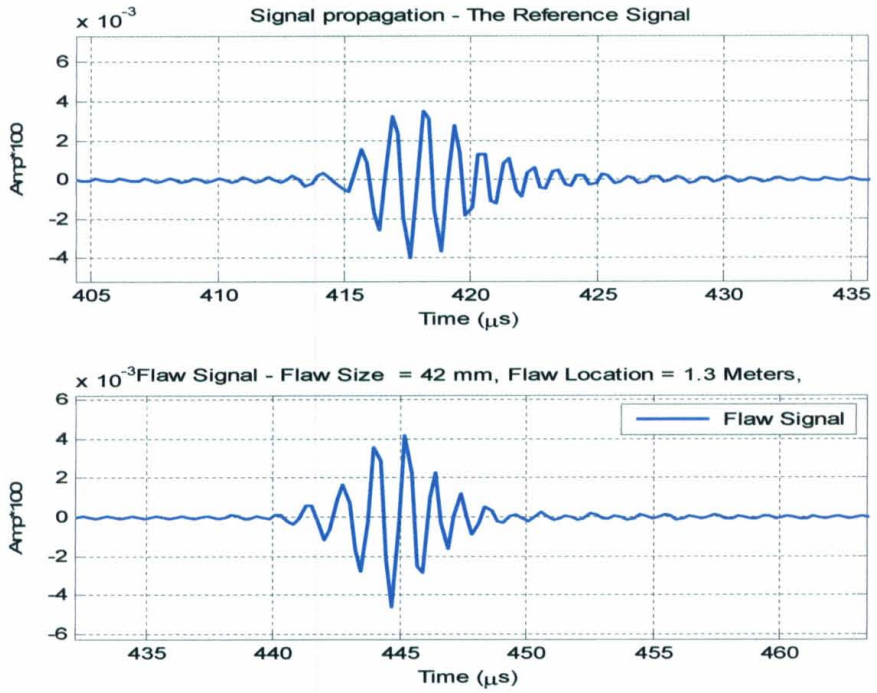

Figure 6.15 – The Time Domain Response for the 42.0 mm Flaw Located at 1.3 meter.

Flaw size, 86mm located at 1.3 meter:

Time at the Highest Amplitude - Ref. Signal:	*418.264 μs*
Maximum Amplitude - Ref. Signal:	*0.431125*
Time at the Highest Amplitude - Flaw Signal:	*473.324 μs*
Maximum Amplitude - Flaw Signal:	*0.412935*
Time Difference between Ref. and Flaw Signals:	*27.5302 μs*
Actual Flaw Location:	*1.3 meters*
Estimated Flaw Location:	*1.28658 meters*
Percentage of Error:	*-1.03232%*
Actual Flaw Size:	*86 mm*
Estimated Flaw Size:	*84.6829 mm*
Percentage of Error:	*-1.53146%*

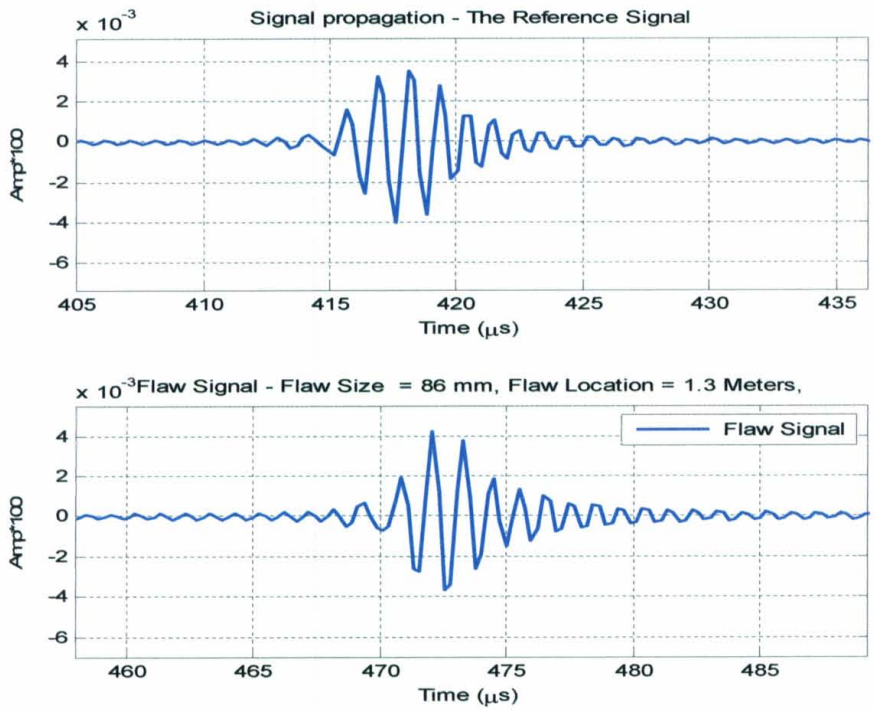

Figure 6.16 – The Time Domain Response for the 86.0 mm Flaw Located at 1.3 meter.

Actual Flaw Size (mm)	Ref. Signal - Time at Highest Amplitude (μs)	Flaw Signal - Time at Highest Amplitude (μs)	Time Difference (μs)	Group Speed (m/s)	Estimated Flaw Size (mm)	% of Error between Actual and Simulation Results (±)
3.00	418.264	419.973	0.85	3076.00	2.63	-12.39%
6.00	418.264	422.293	2.01	3076.00	6.20	3.28%
14.00	418.264	427.298	4.52	3076.00	13.89	-0.76%
16.00	418.264	428.763	5.25	3076.00	16.15	0.92%
21.00	418.264	431.449	6.59	3076.00	20.28	-3.44%
24.00	418.264	433.769	7.75	3076.00	23.85	-0.64%
27.00	418.264	434.868	8.30	3076.00	25.54	-5.42%
29.00	418.264	436.455	9.10	3076.00	27.98	-3.52%
37.00	418.264	441.46	11.60	3076.00	35.68	-3.58%
42.00	418.264	445.245	13.49	3076.00	41.50	-1.20%
86.00	418.264	473.324	27.53	3076.00	84.68	-1.53%

Table 6.1 – Estimated Flaw Sizes by the Simulation and % of Error.

As shown in Table (6.1) that the percentage of error varies from -5.42% up to 3.28% for flaws greater than 3mm. The percentage of error for the 3mm flaw is about 12.4%; it is higher than 10%. This is one of the limitations of the model that when the size of the flaw falls to smaller sizes the accuracy of the estimation starts to decrease significantly. Figure (6.17) illustrates the estimated flaw sizes by the simulation almost agree with the actual values. Table (6.2) shows the estimated flaw location and the percentage of error at 1.03%.

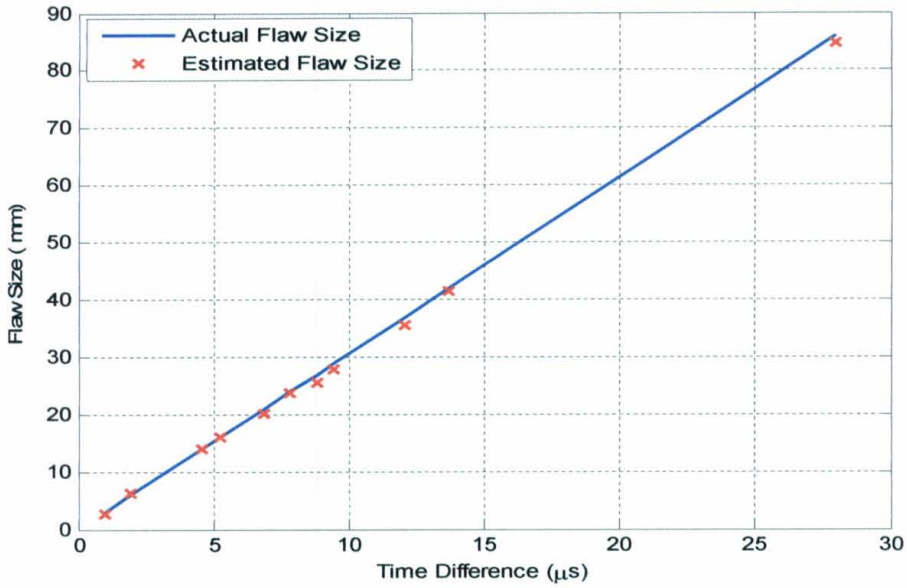

Figure 6.17 – Comparison of the Actual and Simulation Results.

Actual Flaw Size (mm)	Actual Flaw Location (m)	Estimated Flaw Location (m)	% of Error (Actual vs. Simulation) (± %)
3.00	1.30	1.29	-1.03%
6.00	1.30	1.29	-1.03%
14.00	1.30	1.29	-1.03%
16.00	1.30	1.29	-1.03%
21.00	1.30	1.29	-1.03%
24.00	1.30	1.29	-1.03%
27.00	1.30	1.29	-1.03%
29.00	1.30	1.29	-1.03%
37.00	1.30	1.29	-1.03%
42.00	1.30	1.29	-1.03%
86.00	1.30	1.29	-1.03%

Table 6.2 - The Actual Versus the Estimated Flaw Location and % of Error.

Actual Flaw Size (mm)	Estimated Flaw Size (mm)	Experimental Flaw Size - Ref. [20] (mm)	% of Error (Actual vs. Experimental) (±)
3.00	2.62874	2.94	-2.00%
6.00	6.19631	6.39	6.50%
14.00	13.8948	14.79	5.64%
16.00	16.148	17.33	8.31%
21.00	20.2788	22.76	8.38%
24.00	23.8464	24.34	1.42%
27.00	25.5363	27.10	0.37%
29.00	27.9773	29.82	2.83%
37.00	35.6757	37.42	1.14%
42.00	41.4965	42.13	0.31%
86.00	84.6829	84.24	-2.05%

Table 6.3 – The % of Errors for the Difference between Experimental and Actual Flaw Sizes

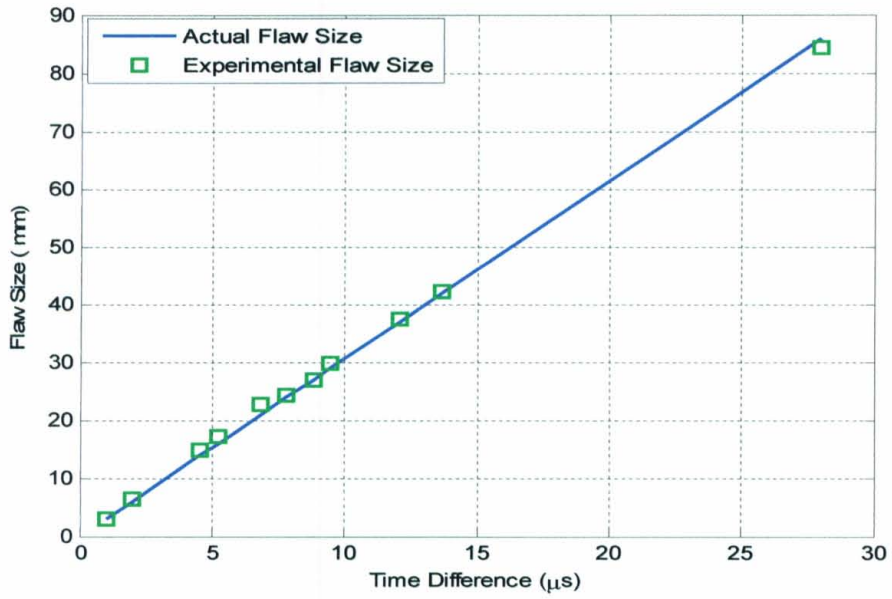

Figure 6.18 – Comparison of the Actual and Experimental Results.

Actual Flaw Size (mm)	Estimated Flaw Size (mm)	Experimental Flaw Size - Ref. [20] (mm)	% of Error (Simulation vs. Experimental) (±)
3.00	2.62874	2.94	10.59%
6.00	6.19631	6.39	3.03%
14.00	13.8948	14.79	6.05%
16.00	16.148	17.33	6.82%
21.00	20.2788	22.76	10.90%
24.00	23.8464	24.34	2.03%
27.00	25.5363	27.10	5.77%
29.00	27.9773	29.82	6.18%
37.00	35.6757	37.42	4.66%
42.00	41.4965	42.13	1.50%
86.00	84.6829	84.24	-0.53%

Table 6.4 – The % of errors for the Difference between Estimated Flaw Sizes by the Simulation and Experiments (Wang et al., 2010).

The percentage of error for the difference between estimated flaws by the simulation and the measured flaw sizes by the experiment in reference (Wang et al., 2010), varies from -0.53% and 10.90% as indicated in Tables (6.4). These variations indicate that there is negligible difference between the values obtained from the simulation and the experiment. This discrepancy is attributed to the impact of the lab environment, test equipment calibration, test setup, temperature of the tested object and noise from the surrounding environment. Figure (6.18) shows the actual flaw sizes (real flaw sizes) versus the measured flaw sizes by the experiments (experimental results) reported in reference (Wang et al., 2010), both the actual and experimental values almost agree with each other.

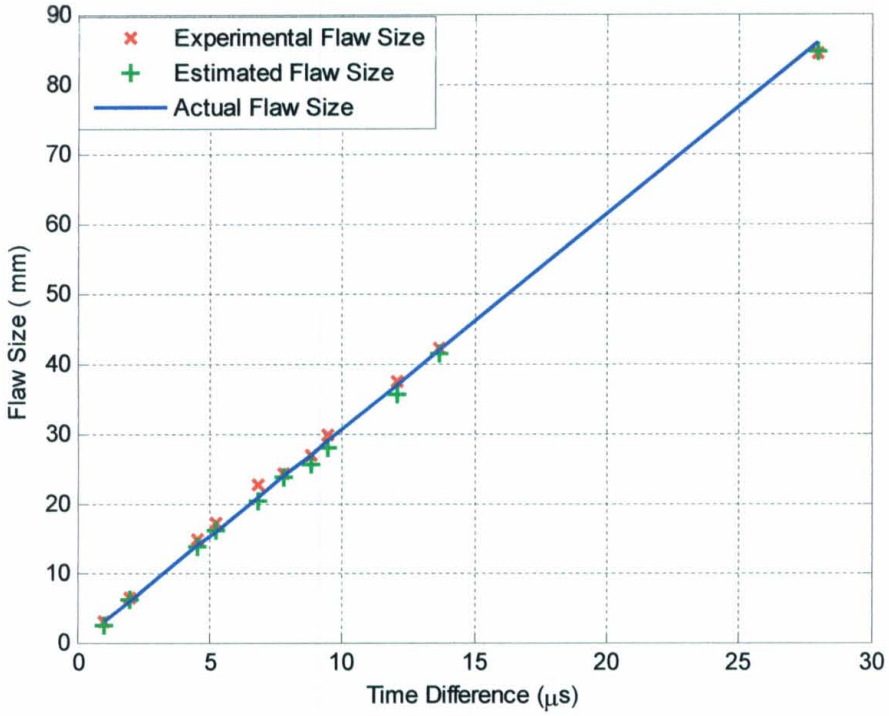

Figure 6.19 – Comparison of the Actual, Simulated and Experimental Results.

Figures (6.19) illustrates the results for the estimated flaw sizes by the simulation and experimental results in (Wang et al., 2010) almost agree with actual results with slight variations.

CHAPTER 7

SUMMARY, CONCLUSIONS AND RECOMMENDATIONS FOR FUTURE WORK

7.1 SUMMARY AND CONCLUSIONS

On-line Structural Health Monitoring (SHM) of industrial structures in particular the oil and gas transporting system such as pipelines are of great importance to the reliability and survivability of oil and gas plants. Due to this importance, an effort has been taken to investigate this subject in more details. The first step in the research was the investigation of the propagation of ultrasonic guided waves into pipes and their interaction with defects. In the subsequent steps, the Kirchhoff flaw approximation model was modified to provide an estimation of the size and location of spherical flaws that may exist along the pipe.

Several simulation trials were performed using Matlab Environment to validate the feasibility and applicability of the modified model. Under the simulation effort, various defects with different sizes located at fixed location along a pipe were analyzed. It was found out that the model can accurately estimate the extent and location of the flaw as the flaw size changes.

Proceeding further with this effort, a comparative analysis was performed for various flaw sizes located at different distances along a 10-meter pipe using pipe parameters

reported in (Wang, Tse, Mechefske & Meng, 2010). The resulted plots from the analysis indicated that the estimated values obtained using the method suggested in this research were very close to the actual values. These findings indicate that the model can accurately estimate the location and the size of the flaw as the location of the flaw changes.

At the end, the results of experiments reported in two research papers (Wang, Tse, Mechefske & Meng, 2010) and (Aiello, Dilettoso & Salerno, 2005) for sizing flaws with varying dimensions have been compared with the simulation results obtained using the method suggested in this thesis. The simulation results produced by this thesis and experimental results reported in the reference articles agreed with each other with little variation. The plots showed that the results for both the simulation and experimental work in the reference article fall reasonably close to each other indicating that the differences between the two are not significant. From the findings stated above, it can be concluded that the modified model can accurately assess the extent and estimate the location of flaws along the pipe.

Hence such a model can serve as an instrumental part in the Structural Health Monitoring (SHM) system of industrial structure such as pipelines. Moreover, this model can assist researchers, to investigate the interaction of ultrasonic waves with different flaw sizes located at different positions along pipes before carrying out any experimental work.

7.2 RECOMMENDATIONS FOR FUTURE WORK

- Perform experimental work to validate this model using different pipes made of different metals other than steel.
- Extend this model to approximate other types of flaws like cracks and cylindrical flaws.
- Expand the work achieved under this research to include an integrated wireless monitoring system using the suggested model under this research and determine how the signal will behave as it travels from solid media to free space and then from free space to solid media. Likewise investigate how the signal will behave as it travels form solid media to water media and then to free space.
- Investigate the use of other Digital Signal Processing (DSP) techniques other than Fourier transforms, such as Wavelet or Haung-Hilbert transforms.

REFERENCES

Achenbach, J.D. (1973). *Wave Propagation in Elastic Solids*. Amsterdam: North Holland.

Ahmad, R. (2005). Guided Wave Technique To Detect Defects In Pipes Using Wavelet Analysis. PhD Thesis, Department of Civil Engineering and Engineering Mechanics, The University Of Arizona, Tucson, AZ, USA.

Ahmad, R,, Banerjee, S. and Kundu, T. (2009). Pipe Wall Damage Detection in Buried Pipes Using Guided Waves. *Journal of Pressure Vessel Technology*, 131 131 / 011501- pp(1-9).

Aiello, G., Dilettoso, E. and Salerno, N. (2005). Finite Element Analysis of Elastic Transient Ultrasonic Wave Propagation for NDT Applications. *Proceedings of the 5th WSEAS/IASME International Conference on Systems Theory and Scientific Computation, Malta*, pp114-119.

Aprameya, k., Anand, R., Mishra, B. & Ahmed, S. (2009). Prediction Of Flaw Response In Polycrystalline Metals For An Ultrasonic Pulse Echo Simulation Using Born Approximation. *Nondestructive Testing and Evaluation Journal*, Vol. 24(3), 289–300.

Auld, B.A. (1973). *Acoustic Fields and Waves in Solids*. (V. I). N.Y: John Wiley & Sons.

Barshinger, J., Lewistown, K. and Rose, J. (2002). Guided Wave Resonance Tuning for Pipe Inspection. *Journal of Pressure Vessel Technology*, 124, 303-310.

Barshinger. N. (2004). Guided Wave Propagation in an Elastic Hollow Cylinder Coated with a Viscoelastic Material. (2004). *IEEE Transactions on Ultrasonic, Ferroelectrics, and Frequency Control,* 51(11),1547-1555.

Bertoncini, F., Musolino, A., Raugi, M. And Turcu, F. (2005). Numerical Simulations for long range guided waves Nondestructive Testing by a wavelet based two port equivalents. *Proceedings of the 5th WSEAS/IASME International Conference on Systems Theory and Scientific Computation*, Malta, pp103-107.

Bertoncini, F. and Raugi, M., (2005). Numerical and Experimental Analysis of Long Range Guided Waves for Non Destructive Testing of Pipes. *Proceedings of the 5th WSEAS/IASME International Conference on Systems Theory and Scientific Computation*, Malta, (pp108-113).

Blitz, J. & Simpson, G. (1991). *Ultrasonic Methods of Non-Destructive Testing*. New York, LLC: Springer-Verlag.

Chen, T., Que, P., Zhang, O. and Liu, Q. (2005). Ultrasonic Nondestructive Testing Accurate Sizing and Locating Technique Based on Time-of-Flight-Diffraction Method. *Russian Journal of Nondestructive Testing*, 41(9), 594–601.

Davies, J and Cawley, P. (2009). The Application of Synthetic Focusing for Imaging Crack-Like Defects in Pipelines Using Guided Waves. *IEEE Transactions on Ultrasonic, Ferroelectrics, and Frequency Control,* 56(4), 759-771.

Demmaa, A., Cawleya, P., Lowea, M., Roosenbr, A. andb, Pavlakovic, B. (2004). The Reflection Of Guided Waves From Notches In Pipes A Guide For Interpreting Corrosion Measurements. *NDT&E International*, 37, 167–180.

Ditri, J.J. (1994). Utilization of Guided Elastic Waves for the Characterization of Circumferential Cracks in Hollow Cylinders. *Journal of the Acoustic Society of America*, Vol. 96, No. 6, pp. 3769-3775.

Doyle, J. (1997). *Wave Propagation in Structures*. (2nd edition).:Springer.

Gazis, D. C. (1958). Exact Analysis of the Plane-Strain Vibrations of Thick-Walled Hollow Cylinders. *The Journal of the Acoustical Society of America,* vol. 30, issue 8, p. 786.

Gazis D. Z. (1959a). Three Dimensional Investigation of Propagation of Waves in Hollow Circular Cylinders. Part I. Analytical Foundation. *The Journal of Acoustical Society of America, 31* (5), 568-573.

Gazis D.Z. (1959b). Three Dimensional Investigation of Propagation of Waves in Hollow Circular Cylinders. Part II. Numerical Results. *The Journal of Acoustical Society of America, 31* (5), 573-578.

Guo, D. (2001). Pipe Inspection by Cylindrical Guided Waves. PhD Thesis, Department of Civil Engineering and Engineering Mechanics, The University of Arizona, Tucson, AZ, USA.

Hay. R. (2004). (2004). The Aspects of Guided Waves in Structural Health Monitoring. PhD, Thesis, The Pennsylvania State University, University Park, PA, USA.

Hideo Nishino, H., Yokoyama, R. Ogura, K., Kondo, H., and Yoshida, K. (2008). Tone-Burst Generation of Circumferential Guided Waves by a Bulk Shear Wave Sensor and Their Wide-Range Time–Frequency Analyses. *Japanese Journal of Applied Physics*, 47(5), 3885–3893.

Hwang, K. (2002). 3-D Defect profile reconstruction form Magnetic Flux Leakage Signature Using Wavelet Basis Function Neural Network. PhD Thesis, Ames, Iowa State University, Iowa, USA.

Ingle, K. and Proakis, G. (2007). *Digital Signal Processing using MATLAB.* (2nd Edition). Stamford, CT, USA: CENGAGE Learning.

Jin, Y. and Eydgahi, A. (2008). Monitoring of Distributed Pipeline Systems by Wireless Sensor Networks. *Proceedings of The 2008 IAJC-IJME Intentional Conference*, Paper 213, IT 304.

Kokossalakis, G. (2006). Acoustic Data Communications System for In Pipe Wireless Sensors Network. PhD Thesis, Dept. of Civil and Environmental Engineering, Massachusetts Institute of Technology. Cambridge, MA, USA.

Kundu, T. (2004). *Ultrasonic Nondestructive Evaluation, Engineering and Biological Material Characterization.* Boca Raton, FL, USA: CRC Press.

Kundu, T. (2007). *Advanced Ultrasonic Methods for Materials and Structure Inspection.* Hoboken, NJ, USA: Wiley-ISTE.

Kwun, H., Kim, S., Matsumoto, H., and Vinogradov, S. (2008). Detection of Axial Cracks in Tube and Pipe Using Torsion Guided Waves. *Review of Quntative Nondestructive Evaluation, American Institute of Physics*, 27, 193-199.

Lathi, B. (2005). *Linear Systems and Signals.* (2nd Edition). New York, NY, USA: Oxford University Press, Inc.

Li, J. and Rose, J. (2001). Implementing Guided Wave Mode Control by Use of a Phased Transducer Array. *IEEE Transactions on Ultrasonics, Ferroelectrics, and Frequency Control,* 48(3), 4-22.

Liu, G. and Qu, J. (1998). Guided Circumferential Waves in a Circular Annulus. *Journal of Applied Mechanics*, 65, 424-430.

Long, R., Lowe, M. and Cawley, P. (2003). Attenuation Characteristics of the Fundamental Modes that Propagate in Buried Iron Water Pipes. *Ultrasonics*, 41(7), 509–19.

Lowe, M., Alleyne, D. and Cawley, P. (1998). Defect Detection In Pipes Using Guided Waves. *Ultrasonics,* 36,147-154.

Lu, B. (2005). On-line Structural Integrity Monitoring and Defect Diagnosis of Steam Generators Using Analysis of Guided Acoustic Waves. PhD Thesis, Nuclear Engineering, The University of Tennessee, Knoxville, Tennessee, USA.

Montesinos, M.E., Munoz-Cobo, J.L. and Perez, C. (2003). Hilbert-Huang Analysis of BWR Neutron Detector Signals: Application to DR Calculation and to Corrupted Signal Analysis. *Annals of Nuclear Energy* 30, pp.715-727.

Mudge, P. and Catton, P. (2008). Quantification of Defect Size from Long Range Guided Wave Ultrasonic Tests on Pipes. *Review of Quantitative NDE, American Institute of Physics*, 27, 147- 154.

Na, W. and Kundu, T. (2002). Underwater Pipeline Inspection Using Guided Waves. *ASME Transactions of the ASME*, 124, 196-200.

Oppenheim, A and Schafer, R. (2010). *Discrete–Time Signal Processing.* (3rd Edition). Upper Saddle River, NJ, USA: Prentice Hall.

Pavlakovic, B. and Lowe, M. (2000). Disperse: *A System for Generating Dispersion Curves User's Manual*. Retrieved August, 2010, from Imperial College, London, UK: http://www.me.ic.ac.uk/dynamics/ndt.

Qing, X. Beard, S., Shen, S., Banerjee, S., Brdley, I., Salama, M., et al. (2009). Development of a Real-Time Active Pipeline Integrity Detection System. *Smart Materials and Structures*, 18-115010.

Rose, J.L. (1999). *Ultrasonic Waves in Solid Media.* Cambridge, UK: Cambridge University Press.

Rose, J. (2000). Guided Wave Nuances for Ultrasonic Nondestructive Evaluation. IEEE *Transactionson On Ultrasonics, Ferroelectrics and Frequency Control*, 47(3), 575-583.

Rose, J. (2004). Ultrasonic Guided Waves in Structural Health Monitoring. *Key Engineering Materials*, 270-273, 14-21.

Schmerr, L. and Song, S. (2007). *Ultrasonic Nondestructive, Evaluation Systems Models and Measurements.*: Springer.

Seco, F., Martín, J., Jiménez, A., Pons, J., Calderón, L., Ceres, R. (2002). *PCDISP: A Tool for the Simulation of Wave Propagation in Cylindrical Waveguides.* Retrieved March, 2011, form Institute of Industrial Automation, (CSIC) web site: http://www.iai.csic.es.

Stoianov, I., Nachman, L. and Madden, S. (2007). PIPENET: A Wireless Sensor Network for Pipeline Monitoring. *Proceedings Of The 6th International Conference On Information Processing in Sensor Networks (IPSN'07),* Cambridge (MIT Campus), Massachusetts, USA.

Sun, Z., Zhang and L. Rose, J. (2005). Flexural Torsional Guided Wave Mechanics and Focusing in Pipe. *Journal of Pressure Vessel Technology*, 127(4), 471- 479.

Takashi K., Nobuhiko, N., Fumitoshi S., and Kiyotaka A. (2006). Guided Wave Pipe Inspection and Monitoring System. *Thermal and Nuclear Power Journal,* 57(9), 660-664.

Wang, X., Tse, P., Mechefske, C. and Meng, H. (2010). Experimental investigation of reflection in guided wave-based inspection for the characterization of pipeline defects. *NDT&E International*, 43 (4) - 365–374.

Wei, L., Pei-Wen, Q. and Guang,Y. (2006). Ultrasonic Flaw Detection During NDE of Oil Pipelines via a Resonance Filter. *Russian Journal of Nondestructive Testing*, 42(6), 398–403.

Yang, Y. (2009). Non-Destructive Evaluation of the Depth of Cracks in Concrete Plates Using Surface Waves. PhD Thesis, University of Waterloo, Canada.

Yen, N. (1994). Wave Packet Decomposition. *Journal of the Acoustic Society of America*, Vol. 95, No. 2, pp. 889-896.

Zemanek, J. Jr. (1998). An Experimental and Theoretical Investigation of Elastic Wave Propagation in a Cylinder. *Journal of Acoustical Society of America*, 10(4), 205-225.

Zhao, X. (2003). Quntative Defects Characterizations via Guided Waves. PhD Thesis, Graduate School, College of Engineering, The Pennsylvania State University, University Park, PA, USA.

Zhao, B. Basir, O. and Mittal, G. (2005). Estimation of Ultrasound Attenuation and Dispersion Using Short Time Fourier Transform. *Ultrasonics*, 43, 375–381.

Zheng, G., Wu, B. and HE, C. (2009). Shape Reconstruction of Flaws In Inhomogeneous Cylinders. *IEEE*, 978-1-4244-4950-7.

Zhuang, W., Shah, A.H. and Datta, S.K. (1997). Axisymmetric Guided Wave Scattering by Cracks in Welded pipes. *Journal of Pressure Vessel Technology*, 119 (4), 401-406.